

# A Model for Heavy Ion Collisions with Quark and Hadronic degrees of freedom

Dissertation  
zur Erlangung des Doktorgrades  
der Naturwissenschaften

vorgelegt beim Fachbereich Physik  
der Johann Wolfgang Goethe-Universität  
in Frankfurt am Main

von

Jan Steinheimer-Froschauer  
aus Frankfurt am Main

Frankfurt am Main, 2010  
(D30)

vom Fachbereich Physik der  
Johann Wolfgang Goethe - Universität als Dissertation angenommen.

Dekan: Prof. Dr. M. Huth

Gutachter: Prof. Dr. Dr. h.c. H. Stöcker, Prof. Dr. S. Schramm

Datum der Disputation: 06.06.2011

Diese Arbeit basiert auf folgenden Publikationen:

- (3+1)-dimensional hydrodynamic expansion with a critical point from realistic initial conditions [67]
- A Fully Integrated Transport Approach to Heavy Ion Reactions with an Intermediate Hydrodynamic Stage [264]
- Strangeness fluctuations and MEMO production at FAIR [180]
- Effects of a phase transition on HBT correlations in an integrated Boltzmann+Hydrodynamics approach [225]
- $\langle m(T) \rangle$  excitation function: Freeze-out and equation of state dependence [216]
- Hydrodynamics with a chiral hadronic equation of state including quark degrees of freedom [7]
- Elliptic flow in an integrated (3+1)d microscopic + macroscopic approach with fluctuating initial conditions [8]
- Strangeness at the international Facility for Antiproton and Ion Research [9]
- A Transport calculation with an embedded (3+1)d hydrodynamic evolution: Elliptic flow as a function of transverse momentum at SPS energies [10]
- Strangeness production and local thermalization in an integrated Boltzmann + hydrodynamics approach [11]
- An effective chiral Hadron-Quark Equation of State [12]
- The problem of repulsive quark interactions - Lattice versus mean field models [13]



# Chapter 1

## Zusammenfassung

### 1.1 Der Aufbau der Materie

Die fundamentalen Bestandteile von Materie sind die Bausteine die die Welt des Mikrokosmos und des Makrokosmos zusammenbringen. Wir denken, dass die kleinsten Bausteine aus denen alle Materie die wir kennen zusammengebaut ist aus Quarks besteht. Auf unglaublich kleinen Längenskalen (weniger als  $10^{-15}$  m) wechselwirken diese durch den Austausch so genannter Gluonen.

In den größten uns bekannten Skalen, den kosmischen, gehen Astrophysiker davon aus, dass das Universum in einem "Big Bang" entstanden ist. In einer sehr kurzen Periode danach war die Temperatur des Universums unvergleichlich hoch. Zu diesem Zeitpunkt könnte die gesamte existierende Materie des Kosmos in einem Zustand freier Quarks und Gluonen, dem sogenannten Quark Gluonen Plasma, vorgelegen haben. Zudem zeigen Astrophysikalische Beobachtungen die Existenz von sehr kompakten Objekten deren Dichten vergleichbar, oder größer, sind als sie in Atomkernen vorliegen.

Um also die fundamentalen Bausteine unserer Welt, die Entstehung des Universums sowie den Aufbau dichter astrophysikalischer Objekte zu beschreiben, müssen wir die Theorie der starken Wechselwirkung verstehen. Das Ziel ist es letztendlich alle Naturphänomene durch fundamentale Kräfte der Natur zu beschreiben. Ein solcher Ansatz ist der im letzten Jahrhundert entwickelte "Standardmodel der Teilchenphysik". Dieses kennt drei fundamental verschieden Teilchentypen: die Quarks, die Leptonen und die Eichbosonen. Man kennt heute 6 verschiedene Quark Sorten die, genau wie die Leptonen, in 3 Familien eingeteilt werden. Die Quarks wechselwirken durch den Austausch von Farbladungen und tragen selber auch eine von 3 dieser Farben. Alle im Labor direkt nachweisbaren Teilchen wie z.B. das Nukleon sind allerdings farbneutrale Kombinationen von Quarks. Die Eichbosonen sind für den Austausch von Wechselwirkungen verantwortlich. Das Austauscheteilchen der starken Wechselwirkung ist das Gluon.

## 1.2 Das effektive Modell für die Zustandsgleichung der QCD

Als fundamentale Theorie der starken Wechselwirkung hat sich die Quantenchromodynamik (QCD) herausgestellt. Es ist eine nicht-abelsche Theorie der Farbladungen. Diese Theorie hat allerdings ein Problem. Da die Kopplungsstärke der QCD abhängig von der Impulsskala ist kann sie in vielen Gebieten nicht analytisch gelöst werden. Sogar im Vakuum sind die Gleichungen der QCD sehr kompliziert, da Gluonen ohne Masse sind und ihre Selbstwechselwirkung daher nicht unterdrückt wird. Nur in Regionen in denen die QCD Kopplung klein ist können analytische Methoden der Störungstheorie angewendet werden.

Alternativ hat sich ein Ansatz etabliert der auf der Lösung von QCD ähnlicher Gleichungen auf einem Raum-Zeit Gitter beruht. Dieser Ansatz, wenn auch vielversprechend, erfordert sehr aufwendige Computer Ressourcen und die systematischen Fehler sind bis heute nicht vollständig kontrollierbar. Desweiteren hat die Gittereichtheorie ein fundamentales Problem bei Berechnungen mit endlicher Baryonendichte. Hier ist die Entwicklung effektiver Modelle der QCD eine notwendige Alternative.

Für besonders heiße oder dichte Systeme sind die Brechung der chiralen Symmetrie sowie ein Aufbrechen des Quarkeinschlusses in Hadronen die interessantesten theoretischen Konzepte. Da die Niederenergie QCD noch nicht analytisch gelöst werden kann fokussieren effektive Modelle meist auf diese beiden Aspekte der QCD. Besonders die Thermodynamik und das Phasendiagramm der QCD sind im momentanen Fokus der Forschung.

Das Hauptziel dieser Arbeit ist es eine effektive Zustandsgleichung für die Quanten Chromo Dynamik zu entwickeln, welche die korrekten asymptotischen Eigenschaften dieser Theorie hat. Diese soll dann als Input für dynamische Modellstudien von Schwerionenkollisionen dienen. Zuerst widmen wir uns daher dem hadronischen Sektor der QCD. Hier sind eine Vielzahl von Zuständen und deren Resonanzen bekannt. Das Hadron-Resonanz-Gas stellt daher eine effektive niedrig Energie Lösung der QCD dar. Da aber bekannt ist das Quarks sich ab einer bestimmten Dichte quasi frei verhalten müssen diese ab einem bestimmten Punkt in das Modell eingebaut werden. In einem HRG kann dies nur über eine Maxwell-Konstruktion geschehen. Dies führt zu einem starken Phasenübergang erster Ordnung was im Widerspruch zu aktuellen Gitterdaten ist. Hier ist dieser Übergang ein stetiger 'Crossover'. Daher muss ein Modell entwickelt werden in dem alle Freiheitsgrade in einer einzigen Zustandssumme eingeführt sind und die daher einen glatten Übergang erlaubt. In dieser Arbeit präsentieren wir ein solches Modell welches die fundamentalen Symmetrien der QCD respektiert sowie die korrekten asymptotischen Freiheitsgrade (Quarks und Hadronen) beinhaltet. Das Modell erlaubt eine gleichzeitige Beschreibung der spontanen Brechung der chiralen Symmetrie sowie einen Übergang von hadronischer zu quark-Materie. Dies wird erreicht indem wir Quarks sowie den thermischen Beitrag des Polyakov Loop in eine hadronisches chirales Modell einführen.

Der hadronische Teil unseres Modells ist eine nichtlineare Realisierung eines sigma-omega Modells. Da die fundamentalen Symmetrien der QCD auch in den hadronischen Zuständen sichtbar sein sollten ist ein solcher Ansatz weit verbreitet um das Verhalten von Hadronen bei hohen Dichten zu simulieren. Mit unserem Modell erreichen wir eine gute Beschreibung des nuklearen Grundzustandes sowie der Vakuumeigenschaften der Hadronen. Die Quarks in diesem Model werden dann als quasi-Teilchen eingeführt welche an den Polyakov Loop koppeln, während die Dynamik des Polyakov Loop durch ein effektives Potential bestimmt wird. In diesem Model dient das sigma-Feld als Ordnungsparameter für die chirale Restauration und der Polyakov Loop für die Befreiung der Quarks. Bei hohen Dichten werden die Hadron durch die Einführung von Volumenkorrekturtermen unterdrückt. Dennoch enthält diese Modell einen nicht vernachlässigbaren Beitrag von Hadronen bis zu einer Temperatur die 2 mal der kritischen Temperatur entspricht.

Wir können zeigen das die Eigenschaften dieser Zustandsgleichung qualitativ mit denen von Gitterdaten übereinstimmen. Besonders die thermodynamischen Größen stimmen sehr gut mit den Gitterdaten überein. Abweichungen sind sehr gut mit hadronischen Beiträgen und Volumenkorrekturen zu erklären. Bei endlicher Baryonenendichte beschreibt das Modell den Phasenübergang von hadronischer zu Quark Materie immer als sehr kontinuierlicher 'Crossover' (Ausgenommen des Flüssig-Gas Phasenübergangs welcher erster Ordnung ist). Bei hohen chemischen Potentialen und mittleren Temperaturen finden wir eine sehr interessante Phase in der die chirale Symmetrie fast restauriert ist aber die dominanten Freiheitsgrade noch die Hadronen sind.

Im Weiteren vergleichen wir Rechnungen zu den Quark-Zahl Suszeptibilität von dem von uns entwickelten Modell mit Ergebnissen der Gitter-Eichrechnung. Unsere Resultate legen nahe, dass die Suszeptibilität schon bei Temperaturen leicht über der kritischen nur mit einem nicht wechselwirkenden Gas von Quarks beschrieben werden kann. Auf der anderen Seite deuten thermodynamische Größen wie die 'Interaction Measure' oder der Wert des normalisierten Polyakov Loops darauf hin, dass starke Wechselwirkungen noch weit oberhalb von  $T_c$  vorliegen.

### 1.3 Das Hybridmodell

Der nächste Schritt dieser Arbeit ist die Einarbeitung der neuen effektiven Zustandsgleichung in ein Modell zu Beschreibung von relativistischen Schwerionenstößen. Ein Ziel der Durchführung dieser Art von Experimenten ist die Suche nach Observablen die sensitiv auf einen Phasenübergang der QCD oder gar auf die Existenz eines kritischen Endpunktes sind. Um die experimentellen Daten interpretieren zu können sind daher Modellstudien unabdingbar. In den vergangenen Jahren waren in diesem Bereich die Verwendung von Fluid dynamischen oder sog. Hybridmodellen favorisiert, denn die Fluid Dynamik erlaubt

die Einbeziehung der Zustandsgleichung auf eine sehr einfache Art und Weise. Um das System der fluiddynamischen Gleichungen zu schließen wird der Druck als Funktion der Energiedichte und Baryondichte benötigt. Dieser funktionale Zusammenhang wird im Allgemeinen als die 'Zustandsgleichung' der Fluiddynamik bezeichnet.

Das von uns verwendete Hybridmodell basiert auf dem Ultra-relativistischen Quantum Molekular Dynamik (UrQMD) Transport Modell und beinhaltet eine hydrodynamische Evolution für die heiße und dichte Phase der Schwerionenkollision. Dabei wird UrQMD verwendet um einen Anfangszustand für die hydrodynamische Phase zu erzeugen. Dazu beschreiben wir jedes Hadron als eine Gaußförmige Verteilung von Energiedichte, Impulsdichten und Baryonenzahl. Summiert man nun über alle Hadronen kann damit eine kontinuierliche Verteilung der Dichten auf einem 3 dimensionalen Raumgitter erzeugt werden. Die Energie- Impuls- und Baryonenzahlverteilungen entwickeln sich als Funktion der Zeit nach den Gleichungen der Fluiddynamik.

Wenn die Dichte im System dann nach einiger Zeit unter einen gewissen Schwellenwert sinkt endet diese Phase und die mit der Cooper-Frye Methode erzeugten Teilchen entkoppeln wieder dynamisch im UrQMD Modell. Eine Voraussetzung zur Verwendung von Fluid dynamischen Modellen ist die Annahme eines lokalen thermodynamischen Gleichgewichtes. In unserem Modell folgt hieraus eine verstärkte Produktion von seltsamen Hadronen. Dies führt zu einer verbesserten Beschreibung von seltsamen Teilchenzahlverhältnissen, insbesondere dem Verhältnis von positiv geladenen Kaonen und Pionen.

Nach einer Studie über die Auswirkungen der Parameter für den Anfangszustand und den Übergang von der Hydrodynamik zurück zum Transportmodell wenden wir uns dem Hauptanliegen dieser Arbeit zu. Wir untersuchen die Abhängigkeit verschiedener Observablen von der verwendeten Zustandsgleichung. Hier können wir zeigen das die kollektiven Eigenschaften des Feuerballs, wie der Teilchenfluß, scheinbar unabhängig von der verwendeten Zustandsgleichung sind. Insbesondere untersuchen wir Observablen wie den gemittelten transversalen Fluß, und die ersten zwei Momente der Multipolentwicklung des Teilchenflusses. Unabhängig von der verwendeten Zustandsgleichung weichen die Modellrechnungen qualitativ von gemessenen Daten ab. Dies bedeutet das andere physikalische Effekte, wie z.B. eine endliche Viskosität oder nicht-Gleichgewichtseffekte eine scheinbar größere Rolle spielen als die Zustandsgleichung.

Obwohl diese Ergebnisse eher enttäuschend erscheinen so gibt es auch neue Resultate zur Berechnung der Emission von Photonen und Di-Leptonen aus der heißen und dichten Phase einer Schwerionenkollision [277, 278, 279, 280]. Diese Rechnungen zeigen, dass die Existenz einer Phase von freien Quarks wichtig für die korrekte Beschreibung von Photonen und Leptonenraten ist. Dies ist dadurch zu erklären, dass die in der Quarkphase erzeugten Leptonen und Photonen nur elektromagnetisch oder schwach wechselwirken und den Feuerball daher fast ungestört verlassen.



## 1.4 Hyperkerne und MEMOs

Im letzten Kapitel dieser Arbeit werden thermische Produktionsraten für Hyperkerne und MEMO's (Metastable Exotic Multihypernuclear Objects) präsentiert. Hyperkerne sind Atomkerne bei denen einzelne Nukleonen durch Hyperonen, also Teilchen mit Seltsamkeit, ausgetauscht werden. Im Vergleich mit der herkömmlichen Nuklidkarte eröffnet sich hierdurch eine dritte Dimension in der Einteilung der Kerne. So sind Hyperkerne mit einer aber auch mehrerer Einheiten von Seltsamkeit möglich. Besonders interessant sind hier die MEMO's. Diese zeichnen sich dadurch aus, dass sie auch vollständig aus Hyperonen aufgebaut sein können. Herkömmliche Hyperkerne sind schon lange bekannt. Auch gibt es seltene Ereignisse von Hyperkernen mit doppelter Seltsamkeit. Die vorhergesagten Di-Baryonen (z.B. Zustände aus 2  $\Lambda$ 's oder  $\Xi$ 's) konnten noch nicht nachgewiesen werden.

Die möglichen Produktionsraten, von Hyperkernen und MEMO's, in Schwerionenexperimenten werden mit dem vorher beschriebenen Hybridmodell berechnet. Des Weiteren können Rapiditäts- und Impulsspektren für Kollisionen von Bleikernen bei Energien von  $E_{lab} = 5$  und  $30A$  GeV vorhergesagt werden. Die Anregungsfunktionen verschiedener Hyperkerne und MEMO's zeigt ein klares Maximum im Energiebereich des geplanten FAIR Beschleunigers. Dieser ist daher der ideale Platz um nach neuen exotischen Zuständen seltsamer Materie zu suchen.

Für den hochinteressanten Bereich der Anti-Hyperkerne sind die Schwerionenexperimente am LHC sehr aussichtsreich. Durch diese beiden Experimente wird es möglich sein noch weiter die unentdeckten Bereiche der (anti-)seltsamen Nuklidkarte zu erforschen.

Im Vergleich zu älteren Studien zur Produktion von MEMO's und Hyperkernen, basierend meist auf statistische Modelle mit globaler Erhaltung der Seltsamkeit, zeigt unser Modell, dass die Seltsamkeit lokal nicht erhalten ist. Dies konnte im Impuls wie auch im Ortsraum gezeigt werden. Um diese Trennung von Seltsamkeit und Anti-Seltsamkeit zu erreichen bedarf es hier nicht eines Phasenüberganges zum Quark Gluon Plasma. Diese Fluktuationen im Phasenraum könnten zu einer erhöhten Produktion von seltsamen Clustern wie MEMO's und Hyperkernen führen. Eine Verstärkung solcher Fluktuationen und Clusterbildung kann durch eine vorhergesagte Destillation noch verstärkt werden. Desweiteren können wir zeigen wie die Emission von Kaonen eine Anreicherung der Quarkphase mit seltsamem Quarks noch verstärkt. Dies hätte eine erhöhte Produktionsrate von Clustern mit Seltsamkeit zur Folge.

Ein weiterer Mechanismus zur Produktion von Hyperkernen in Schwerionenkollisionen ist die Absorption von Hyperonen in den Spektatorfragmenten. Diese hoch angeregten Kernfragmente können im Feuerball erzeugte  $\Lambda$  oder  $\Xi$  Teilchen absorbieren und dann zu kleineren Hyperkernen zerfallen. Von besonderem Interesse ist hier das was wir zeigen konnten, dass  $\Lambda$ 's sowie  $\Xi$ 's absorbiert werden können. Dies wäre besonders für die Untersuchung von doppelt seltsamen  $\Xi$ -Hyperkernen interessant. In dieser Arbeit verwenden wir das

UrQMD Modell in seiner Cascade-Version um die Absorptionsraten für diese Teilchen bei einer Laborenergie von  $E_{lab} = 20A$  Gev abzuschätzen. Zusätzlich können wir auch die Raum-Zeit und Impulsinformationen für solche absorbierten Teilchen angeben und untersuchen.

# Contents

<b>1</b>	<b>Zusammenfassung</b>	<b>5</b>
1.1	Der Aufbau der Materie . . . . .	5
1.2	Das effektive Modell für die Zustandsgleichung der QCD . . . . .	6
1.3	Das Hybridmodell . . . . .	7
1.4	Hyperkerne und MEMOs . . . . .	9
<b>2</b>	<b>Introduction</b>	<b>17</b>
2.1	Fundamental degrees of freedom . . . . .	17
2.2	QCD . . . . .	18
2.2.1	Symmetries . . . . .	20
2.2.2	Deconfinement . . . . .	22
2.3	Heavy ion collisions . . . . .	24
<b>3</b>	<b>A model for HIC</b>	<b>27</b>
3.1	The UrQMD model . . . . .	29
3.2	The initial state . . . . .	30
3.3	The fluid-dynamic phase . . . . .	32
3.4	The freezeout and final state . . . . .	33
<b>4</b>	<b>The EoS</b>	<b>39</b>
4.1	The Hadron Resonance Gas (HRG) . . . . .	40
4.1.1	Including quarks . . . . .	41
4.1.2	Excluded volume corrections . . . . .	43
4.2	The Chiral hadronic model . . . . .	44
4.3	The PNJL model . . . . .	45
4.4	Including quarks in the chiral model . . . . .	46
4.4.1	Results at zero baryochemical potential . . . . .	52
4.4.2	Results at nonzero baryochemical potential . . . . .	59
4.4.3	Susceptibilities . . . . .	63
4.4.4	Distillation . . . . .	66

<b>5</b>	<b>Results</b>	<b>71</b>
5.1	Investigating bulk matter properties . . . . .	71
5.1.1	Strangeness ratios with the HRG . . . . .	72
5.1.2	Freezeout dependence . . . . .	73
5.1.3	The speed of sound . . . . .	78
5.1.4	Comparisons of different EoS . . . . .	80
5.2	Production of hypernuclei in HIC . . . . .	94
5.2.1	From the fireball . . . . .	95
5.2.2	From the spectator region . . . . .	109
<b>6</b>	<b>Summary</b>	<b>115</b>
6.1	Outlook . . . . .	118
<b>A</b>	<b>Effective chiral models</b>	<b>121</b>
A.1	The linear sigma model . . . . .	121
A.2	The nonlinear sigma model . . . . .	123
<b>B</b>	<b>Trace anomaly and scale invariance</b>	<b>125</b>
<b>C</b>	<b>Viscous fluid dynamics</b>	<b>127</b>
	<b>Literaturverzeichnis</b>	<b>127</b>
C.1	Danksagung . . . . .	146
C.2	Lebenslauf . . . . .	147
C.3	Akademische Lehrer . . . . .	148

# List of Figures

2.1	Heavy quark free energy . . . . .	23
2.2	Conjectures phase diagram of QCD . . . . .	25
3.1	Initial state net baryon distribution . . . . .	31
4.1	Bag model phase construction . . . . .	41
4.2	Phase diagram for a HRG + QGP construction . . . . .	42
4.3	Phase diagram with a critical endpoint . . . . .	51
4.4	Order parameters at $\mu_B = 0$ . . . . .	53
4.5	Particle densities at $\mu_B = 0$ . . . . .	54
4.6	Quark fraction at $\mu_B = 0$ . . . . .	55
4.7	Pressure and energy density at $\mu_B = 0$ . . . . .	56
4.8	Interaction measure at $\mu_B = 0$ . . . . .	57
4.9	The speed of sound at $\mu_B = 0$ . . . . .	58
4.10	Particle densities and binding energy per nucleon at $T = 0$ . . . . .	60
4.11	The chiral order parameter as a function of $T$ and $\mu_B$ . . . . .	61
4.12	The polyakov loop, order parameter of the deconfinement phase transition, as a function of $T$ and $\mu_B$ . . . . .	62
4.13	The fraction of the quark and gluonic portion of the energy density as a function of $T$ and $\mu_B$ . . . . .	63
4.14	Second and fourth order quark number susceptibility from the PNJL model . . . . .	64
4.15	Second and fourth order quark number susceptibility from the QH model . . . . .	65
4.16	Binding energy per particle as a function of strangeness per baryon for different values of the hyperon interaction . . . . .	67
4.17	Time evolution of the strangeness per baryon fraction for 2 coexisting phases . . . . .	69
5.1	Excitation functions for kaon to pion ratios and strange baryon to pion ratios . . . . .	73
5.2	Freeze-out dependence of the $\langle m_T \rangle$ excitation function of $\pi$ 's and protons . . . . .	76
5.3	Freeze-out dependence of the $\langle m_T \rangle$ excitation function of kaons . . . . .	77
5.4	Isentropic expansion paths and contours of the speed of sound in the $\epsilon$ - $n$ phase diagram . . . . .	78
5.5	Excitation function of the averaged speed of sound in most central A+A collisions . . . . .	79

5.6	EoS dependence of the $\langle m_T \rangle$ excitation function of pions and protons . . .	82
5.7	EoS dependence of the $\langle m_T \rangle$ excitation function of kaons . . . . .	83
5.8	Total $4\pi$ multiplicities of pions, $\Xi$ 's and kaons . . . . .	85
5.9	Rapidity distributions for different particle species at three different beam energies . . . . .	86
5.10	Mean transverse mass spectra of different particle species . . . . .	87
5.11	Excitation functions of the mean transverse mass of pions, protons and kaons	88
5.12	The directed flow $v_1$ for pions and protons at $E_{\text{lab}} = 40A$ GeV . . . . .	92
5.13	Elliptic flow of pions in mid-central (b=5-9 fm) Pb+Pb collisions . . . . .	93
5.14	Multiplicities of various types of MEMOs and strangelets in central Pb+Pb reactions . . . . .	97
5.15	Excitation functions of the multiplicities of various MEMOs in central Pb+Pb reactions . . . . .	98
5.16	Normalized rapidity density of various MEMOs in central Pb+Pb reactions	98
5.17	Transverse momentum spectra at midrapidity of various MEMOs in central Pb+Pb reactions . . . . .	99
5.18	Excitation function of the multiplicity of several hypernuclei and di-baryons	101
5.19	Excitation function of the multiplicity of several anti-hypernuclei and anti-di-baryons . . . . .	102
5.20	Excitation function of the ratio $R_H$ for different model calculations compared to data . . . . .	103
5.21	Energy dependence of the strange quark over anti-strange quark ( $s/\bar{s}$ ) ratio	104
5.22	Rapidity dependence of the strange quark over anti-strange quark ( $s/\bar{s}$ ) ratio	106
5.23	Transverse momentum dependence of the strange quark over anti-strange quark ( $s/\bar{s}$ ) ratio . . . . .	107
5.24	Fluctuations of the strangeness fraction $f_s = \rho_s/\rho_B$ in the central plane for a single central Pb+Pb reaction . . . . .	108
5.25	Distribution of the absorbed $\Lambda$ 's in the X-Z-plane . . . . .	111
5.26	Distribution of the absorbed $\Lambda$ 's in the transverse-plane . . . . .	112
5.27	Momentum distribution of the absorbed $\Lambda$ 's . . . . .	113
A.1	Mexican-Hat potential . . . . .	122

# List of Tables

2.1	Properties of the quarks . . . . .	18
2.2	Properties of the leptons . . . . .	18
2.3	Particles of the spin 1/2-baryon octet . . . . .	21
2.4	Particles of the pseudoscalar octet . . . . .	22
4.1	Coupling parameters for the hadronic chiral model . . . . .	49
4.2	Parameters for the hadronic chiral model . . . . .	50
4.3	Parameters for the Polyakov potential . . . . .	50
5.1	Properties of all considered multibaryonic states . . . . .	95
5.2	Rate of absorbed strange baryons . . . . .	110





# Chapter 2

## Introduction

The fundamental constituents of matter are the building blocks which bring together the world of the very small and the world of the very large. For the very small part we think that the elementary building blocks, which all matter we know is made off, consist of quarks. On very small sub nuclear length scales ( $< 10^{-15}\text{m}$ ) they interact via the strong interaction and the exchange of so called gluons.

On the very large side, cosmologists think that the universe was created in a very big bang. In the short period after it, the temperature of the universe was incredibly large. At this point all the matter of the universe may have existed in a state of matter called the quark gluon plasma, which is a gas of free quarks and gluons (which are the particles that transmit the strong force). Furthermore astrophysical observations show objects (compact stars) that are as dense as normal nuclear matter. Even denser astrophysical objects are possible in which the strong interaction becomes the dominant force that is keeping those objects from collapsing to a black hole.

This means in order to understand the basic building blocks we are made of as well as the very early evolution of the universe and the nature of compact stars we have to understand the theory of the strong interaction. The final aim is to explain all observed phenomena in nature by the fundamental interactions of elementary particles. Experimental and theoretical efforts in the last century have lead to the formulation of a physical theory: the standard model of particle physics.

### 2.1 Fundamental degrees of freedom

The *Standard model of particle physics* knows three fundamentally different types of particles: the quarks, the leptons and the gauge bosons.

By today we know 6 different quark flavors and their anti-particles: up-, down-, strange-, charmed-, bottom- (or beauty-), and top-quarks. Furthermore one can distinguish three generations of quarks, each with 2 flavors where always one flavor has an electric charge of  $+2/3$  and  $-1/3$ .

The quarks interact through the exchange of colored charges. Interestingly all known

Name	Short	Mass [MeV]	electric charge [e]
down	d	4...8	$-\frac{1}{3}$
up	u	1.5...4	$+\frac{2}{3}$
strange	s	80...130	$-\frac{1}{3}$
charm	c	1300...1700	$+\frac{2}{3}$
bottom	b	4700...5300	$-\frac{1}{3}$
top	t	> 9100	$+\frac{2}{3}$

Table 2.1: Properties of the quarks (from [14])

existing stable particles, consisting of combinations of quarks, are color neutral. The fundamental theory of color charge, quantum chromo dynamics (QCD) knows three colors, green, red and blue. Only combinations of all of the three colors or color-anti-color combinations are neutral.

This means that we can classify the existing composite objects, hadrons, into simply being a meson (quark- antiquark state) or a baryon (e.g. a proton or neutron). Theoretically there are also other combinations allowed, e.g 3 quark + 1 quark antiquark pair (the Pentaquark), but their existence has not been established.

From the leptons we also know 6 distinct particles. The electron, the muon and the tau, each forming a generation with its neutrino. The electric charge of the leptons is either 1 or 0.

Name	Short	Mass [MeV]	Electric charge [e]
Electron	e	0.512	-1
Electron-Neutrino	$\nu_e$	$< 7.3 \cdot 10^{-6}$	0
Muon	$\mu$	105.66	-1
Muon-Neutrino	$\nu_\mu$	< 0.27	0
Tau-Lepton	$\tau$	1776	-1
Tau-Neutrino	$\nu_\tau$	< 31	0

Table 2.2: Properties of the leptons (from [14])

The gauge bosons are accountable for the transmission of the different forces. The electromagnetic force for example is transmitted by the photon. Furthermore we know the  $W^{+-}$  and  $Z^0$  (weak interaction) and the Gluon (strong interaction).

## 2.2 QCD

Quantum chromodynamics is the fundamental theory of the strong interaction and therefore should enable us to describe how the fundamental blocks of matter are formed. It as

a nonabelian gauge theory of color charge [15, 16, 17]. The QCD Lagrangian is:

$$L_{QCD} = -\frac{1}{4}G^{\mu\nu}G_{\mu\nu} + \sum_k \bar{\Psi}_k(i\gamma^\mu D_\mu - m_k)\Psi_k, \quad (2.1)$$

with:

$$G_{\mu\nu} = \partial_\mu A_\nu - \partial_\nu A_\mu - ig[A_\mu, A_\nu] \quad (2.2)$$

$$D_\mu \Psi_k = (\partial_\mu - igA_\mu)\Psi_k \quad (2.3)$$

$$A_\mu = \sum_{a=1}^8 A_\mu^a \lambda^a / 2 \quad (2.4)$$

where  $\psi_k$  denotes the quark fields with the flavor index  $k$ .  $G_{\mu\nu}$  is the gauge field strength tensor of the gluon fields  $A_\mu^a$  and  $\lambda^a$  are the eight  $SU(3)$  Gell-Mann matrices. The interaction strength is defined by a running coupling constant:

$$\alpha_s(\mu) = \frac{4\pi}{\beta_0 \ln(\mu^2/\Lambda_{QCD}^2)} \quad (2.5)$$

Here  $\beta_0 = 11 - 2N_f/3$ ,  $\mu$  is the energy scale and  $\Lambda_{QCD} \approx 0.2$  GeV is the QCD scale parameter. Because the coupling strength of QCD is not independent of the momentum scale, problems arise when the theory is to be solved analytically. Even in the vacuum QCD is very complicated as the gluons are massless and their interactions not dampened by a small coupling parameter. In the region of small  $\alpha_s$  perturbative approaches are valid but this is not so as the coupling becomes large. At large and intermediate couplings, the region where also the interesting hadronic physics takes place, QCD is not analytically solvable and other methods have to be applied.

One of these methods is lattice QCD. Here different actions, resembling the physics of QCD are evaluated with Monte Carlo sampling methods on a numerical grid. Though promising, lattice calculations are incredibly demanding on computer power and the results are very dependent on the computational power available. At the moment lattice calculations are still restricted on observables in non-dynamic systems of QCD.

Since it is not possible to describe systems of hadrons from the quark level, one has to begin with models that already include hadronic degrees of freedom. This is reasonable as we know that many hadronic states exist and that they are somehow created through the interactions of QCD. Using this method one formulates an effective Lagrangian that reproduces some fundamental features and symmetries of the QCD Lagrangian but is formulated in a hadronic language. One has to be carefull, as such an approach is usually only valid in a certain applicability region of QCD, but often proves valuable in understanding some fundamental features of QCD. Such models are usually referred to as effective models of quantum chromo dynamics.

### 2.2.1 Symmetries

Symmetries are an important concept in physics. Technically one defines a symmetry, with respect to a variable, whenever the action  $S$  is invariant under a variation of the Lagrange function  $L$ . Let's assume the variable  $\Phi$  is transformed like:

$$\Phi \longrightarrow \Phi + \delta\Phi \quad (2.6)$$

If a symmetry with respect to  $\Phi$  is present:

$$S = \int dx^4 L(\Phi + \delta\Phi) = \int dx^4 L(\Phi) \quad (2.7)$$

Following the Noether theorem [1] we know that we can assign a conserved current  $J_\mu$  to every symmetry ( $\partial^\mu J_\mu = 0$ ).

Examples for this are the energy conservation which follows from an invariance regarding a time transformation or the momentum conservation which is connected to an invariance under a spatial transformation.

The QCD Lagrangian possesses the symmetries off the strong interaction. One of them is the invariance under a  $U(1)$  transformation,

$$\Psi(x) \rightarrow \exp(i\theta)\Psi(x), \quad (2.8)$$

which results in the conservation of the baryon number current  $\bar{\Psi}\gamma^\mu\Psi$  and the conservation of the baryon number:

$$B = \frac{1}{3} \int d^3x \Psi^\dagger \Psi \quad (2.9)$$

#### Chiral symmetry

Chirality is the property of an object or system that says that it cannot be brought into congruence with its mirror image by a rotation around the mirror axis. The wavefunction of a fermion for example can be divided into two pieces which can interchange through a parity transformation. The associate quantum mechanical quantity is called chirality.

One can define a vectorial,

$$\psi \rightarrow \psi' = \exp(-i\Theta_V^a G_a)\psi \approx (1 - i\Theta_V^a G_a)\psi \quad (2.10)$$

and axial transformation.

$$\psi \rightarrow \psi' = \exp(-i\gamma_5 \Theta_A^a G_a)\psi \approx (1 - i\gamma_5 \Theta_A^a G_a)\psi. \quad (2.11)$$

where  $\psi$  is the wavefunction of a defined quark flavor.  $\Theta$  is the transformation parameter.  $\gamma_5 = i\gamma_0\gamma_1\gamma_2\gamma_3$  ( $\gamma_\mu$  are the Dirac matrices) and the  $G_a$  are the generators of the corresponding symmetry group. If the QCD Lagrangian is symmetric with respect to these

transformations it has a chiral symmetry. The conserved currents associated with this symmetry are the vector currents:

$$V_a^\mu = \bar{\psi} \gamma^\mu \frac{\lambda_a}{2} \psi \quad (2.12)$$

and the axialvector currents:

$$A_a^\mu = \bar{\psi} \gamma^\mu \gamma_5 \frac{\lambda_a}{2} \psi \quad (2.13)$$

### Breaking of chiral symmetry

The above is only true in the case of zero quark masses. Introducing a quark mass in the Lagrangian adds terms of the form:

$$L_{m_i} = m_i \bar{\psi} \psi, \quad (2.14)$$

where  $m_i$  are the current quark masses. From experiment these are.

$$m_u = 1.5 - 4 \text{ MeV}, \quad m_d = 4 - 8 \text{ MeV}, \quad m_s = 80 - 130 \text{ MeV}. \quad (2.15)$$

The mass term breaks the chiral symmetry of the QCD Lagrangean explicitly. But since the masses of the light flavors are very small this symmetry breaking is only very weak and one often speaks of an approximate chiral symmetry.

If chiral symmetry was an exact (or approximate) symmetry of QCD, this would lead to a degeneracy between states of different parity. The  $\rho$  meson for example would be degenerate with the  $a_1$ . In the vacuum this is not the case. In fact we observe a wide range of hadronic states with a mass hierarchy. Table (2.3) lists the properties of the particles of the lowest baryonic octet. These composite particles should be the lowest mass eigenstates of QCD. As one can see the masses are rather large when compared to the bare quark mass [18, 19].

Name	Short	Mass [MeV]	Elektric Charge [e]
Proton	$p$	938.3	+1
Neutron	$n$	939.6	0
Lambda	$\Lambda$	1115.6	0
Sigma	$\Sigma^+$	1189.4	+1
Sigma	$\Sigma^0$	1192.6	0
Sigma	$\Sigma^-$	1197.4	-1
Xi	$\Xi^0$	1314.9	0
Xi	$\Xi^-$	1321.3	-1

Table 2.3: Particles of the spin 1/2-baryon octet (from [14])

Name	Short	Mass [MeV]	Electric charge [e]
Pion	$\pi^+$	139.57	+1
Pion	$\pi^-$	139.57	-1
Pion	$\pi^0$	134.97	0
Eta	$\eta$	547.8	0
Kaon	$K^+$	493.7	+1
Kaon	$K^-$	493.7	-1
Kaon	$K^0$	497.6	0
Kaon	$\bar{K}^0$	497.6	0

Table 2.4: Particles of the pseudoscalar octet (from [14])

In addition the Goldstone theorem [20] tells us that if a symmetry is broken spontaneously, the spectrum of the theory must contain  $(p - k)$  massless particles (where  $(p - k)$  is the number of operators that break the symmetry). As can be seen in table (2.4) the pseudoscalar mesons (and the mesons in particular) are much lighter than most other hadronic states of QCD, and could be identified with as the Goldstone modes of QCD.

In other words the chiral symmetry of QCD is most likely spontaneously broken in the vacuum. This means that while the Lagrangian of QCD is still symmetric with respect to the chiral transformation, the energetically most favorable state in the vacuum is not. The masses of the baryons are large due to the spontaneous breaking of chiral symmetry and the pions are massive Goldstone bosons because chiral symmetry is also broken explicitly.

This fundamental knowledge about the symmetries of QCD led to the development of numerous effective models. These models are based on an effective Lagrangian which has some or many of the symmetries of QCD and therefore should be able to capture certain physical aspects of the theory. An introduction into some basic models will be given in Appendix (A).

### 2.2.2 Deconfinement

The deconfinement aspect of quantum chromo dynamics describes the fact that we can only observe states that are color neutral. That means, as a single quark carries a color charge we will never be able to directly observe a quark. Since gluons are massless and they do also carry a color charge they can easily interact with each other. In the case of a strong coupling strength these interactions dominate the QCD dynamics.

Figure 2.1 shows the free energy, which is proportional to the potential, of a heavy quark in the vacuum (solid line). As one can see, the potential rises linearly with the distance and therefore one would need an infinite amount of energy to separate a colored object (like a quark) from the heavy quark. The real problem arises from the fact that the colored field,

which increases in energy the more the quark is pulled apart, will at one point create a quark-antiquark pair, thus creating now again two colorless objects which can depart from one another.

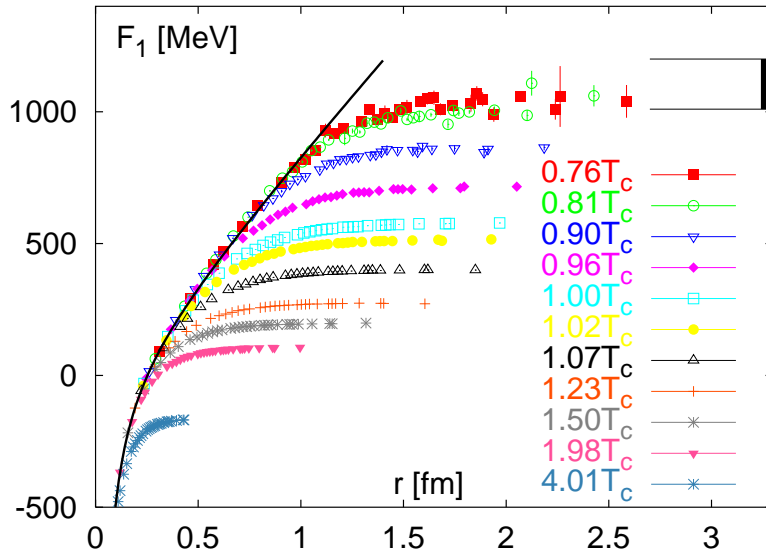


Figure 2.1: The free energy of a heavy quark in the vacuum (solid line) and at different temperature as calculated from the lattice (Taken from [21]).

In the pure gauge sector (the pure gluonic theory without quarks) a deconfinement phase transition can be connected to the breakdown of the QCD  $Z(3)_f$  symmetry [22] ( $Z(3)$  is a center symmetry which implies invariance with respect to a simple phase multiplication [23]).

This phase transition has a well defined order parameter, the Polyakov loop (or Wilson-Polyakov loop) which is the trace of the Wilson line defined as:

$$L(\vec{x}) = \mathcal{P} \exp \left( i \int_0^\beta A_4 dx_4 \right) \quad (2.16)$$

with  $\beta = 1/T$  the inverse temperature and  $A_4 = iA_0$  the zero component of the gauge field.

In the presence of dynamical quarks this might change and is still under debate if the Polyakov loop and the breakdown of center symmetry are still good order parameters for deconfinement or maybe only approximate.

## 2.3 Heavy ion collisions

The above considerations all hint to the fact that some interesting new physics can be expected if one is able to produce a medium that is either very hot or very dense. In both cases one can expect the chiral condensate ( $\langle \bar{\psi}\psi \rangle$ ), which is responsible for the spontaneous breaking of chiral symmetry, to melt. This would lead to a restoration of chiral symmetry and a drastic change in the properties of the particles in the matter created. In addition one expects at some point to reach a temperature/density at which deconfinement can be realized and even a quasi free gas of quarks and gluons can be formed (QGP).

Experimentally such a system is not easily produced. High energy heavy ion collisions aim at creating a system hot and dense enough simply by smashing gold or lead ions at very large energies against each other. In this process the kinetic energy is transformed into compressional energy and heat and, if the collision lasts long enough, a fireball of very hot QCD matter can be created. By changing the beam energy, and therefore the energy available for heating, and the system size one hopes to explore wide regions of the phase diagram of QCD especially the existence of a QGP [24, 25]. In the recent years several collider programs have performed collisions at different beam energies. At the SIS (SchwerIonen Synchrotron) at the GSI (Gesellschaft für SchwerIonenforschung) near Darmstadt experiments with the lowest energies ( $E_{\text{lab}} \approx 2A$  GeV) were performed [26, 27, 28]. At the Brookhaven National Lab (BNL) near New York, experiments were performed at the AGS (Alternating gradient Synchrotron) for energies of  $E_{\text{lab}} \approx 2 - 11A$  GeV [29, 30, 31] and after that with the Relativistic Heavy Ion collider (RHIC) ( $\sqrt{s} = 56 - 200$  GeV).

At the Super Proton Synchrotron (SPS), located at the CERN facility near Geneva much data was taken in the intermediate energy region of  $E_{\text{lab}} = 20 - 160A$  GeV [32, 33, 34, 35, 36, 37, 38]. In this energy regime the data show interesting features in several observables which are not yet fully understood. Future experiments at the FAIR (Facility for Anti-proton and Ion Research), next to GSI, are aimed at finding more evidence for a possible change in QCD degrees of freedom at energies between  $E_{\text{lab}} = 10 - 40A$  GeV, while the Large Hadron Collider at CERN will explore incredibly high energy collisions ( $\sqrt{s} = 14$  TeV).

Figure (2.2) shows a conjectured phase diagram of QCD bulk matter. Indicated are the regions of the phase diagram where the systems, created at the different experiments, will be situated. This is only a very rough conjecture, but it still captures the main idea, that it is possible to scan a wide region of temperatures and baryon densities simply by smashing heavy ions at different beam energies.



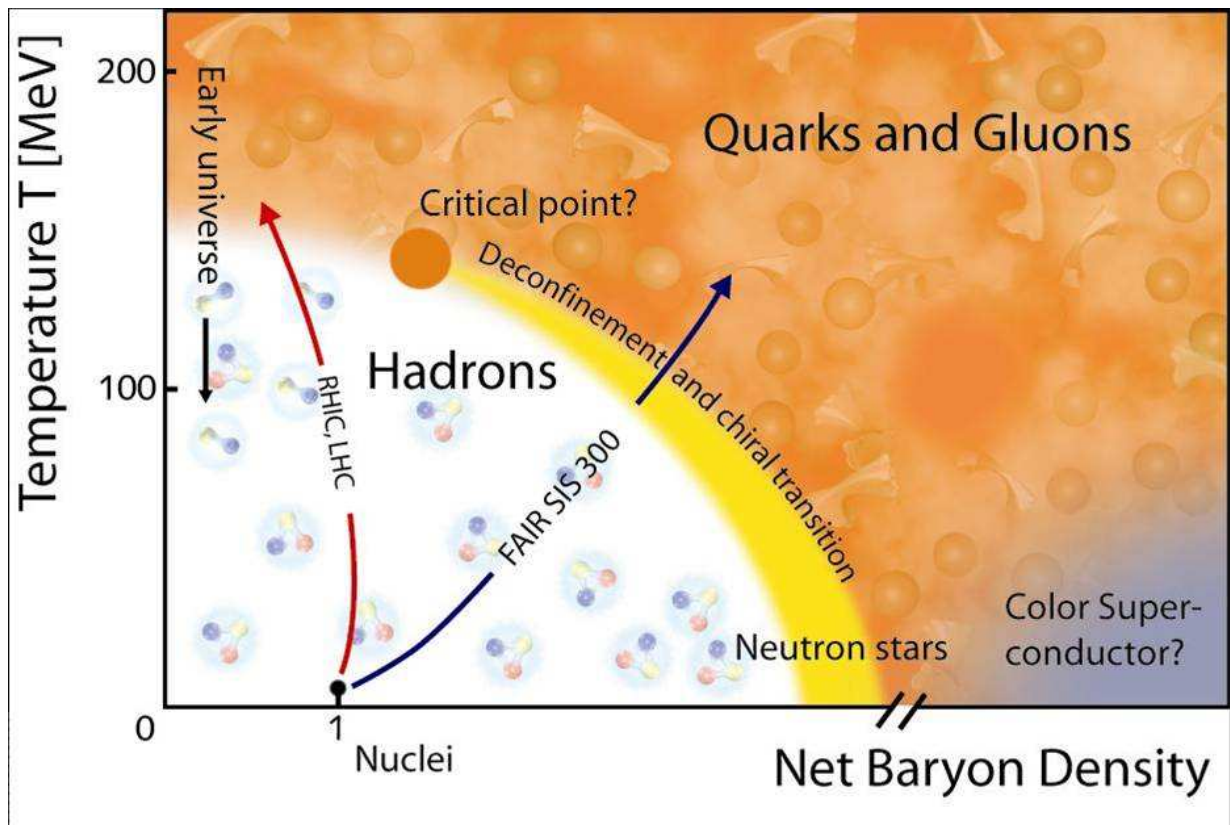


Figure 2.2: Conjectured phase diagram of QCD in terms of temperature and net baryon density. Indicated is a region of phase coexistence which ends at a critical endpoint. Also shown are possible scenarios for systems created at the RHIC and future FAIR experiments (Taken from the GSI webpage [2]).



# Chapter 3

## A model for HIC

The recent experimental results at the Relativistic Heavy Ion Collider (RHIC), suggesting the creation of a nearly perfect fluid [39, 40, 41, 42], have fueled interest in the study of bulk properties of strongly interacting matter (QCD). Heavy ion experiments at different beam energies try to map out the QCD phase diagram, especially the region where one expects a phase transition from a confined gas of hadrons to a deconfined state of quarks and gluons (QGP) [43, 44, 45, 46, 47, 48, 49, 50, 51, 52, 53, 54]. To relate any experimental observables to the properties of the matter produced in heavy ion collisions, a profound understanding of the thermodynamics of QCD has to be obtained and integrated in model simulations of these collisions.

In general one tries to segment a heavy ion collision (HIC) at relativistic energies into three phases, each lasting only a few  $fm/c$ .

1. Initial pre-equilibrium phase:

This phase begins when the nucleons of the target and projectile first collide with relativistic energies. These so called initial collisions can be described as binary collisions of two nucleons as for example in proton proton collision experiments. The kinetic energy of the nucleons is transferred into the mass of produced particles as well as fields, which can be of partonic (quarks) and hadronic type. Shortly after the initial collisions have occurred the produced particles and fields can start to interact with the reaction products of different constituent collisions. If enough particles are created and the energy or particle density is high enough the system can move to phase 2.

2. Equilibrium expansion phase:

If the produced particles had enough time to scatter multiple times, the hot system may reach a state of local thermal equilibrium, which means that it can be characterized by intensive quantities like the pressure, energy and particle. The system therefore should show collective behavior and may be described by a hydrodynamic approach.

### 3. Decoupling phase:

After the system dilutes, the condition of local thermal or chemical equilibrium may not be fulfilled anymore and the system starts to decouple. The hadrons, having the vacuum properties as we know them, are formed and after their last scattering may fly into a detector to be measured.

This is of course only a simplistic view of what really occurs, nevertheless the most important aspects can be captured in this simple sequence. A model that aims at describing a heavy ion collision at relativistic energies therefore has to be able to reproduce all of these phases.

The equilibrium phase is usually described by a hydrodynamic model, where effects of a phase transition can be easily introduced by use of the equation of state. In general, the equations of hydrodynamics conserve energy and moment and, for ideal hydrodynamics, also the entropy. As the initial and final phases are governed by out-of-equilibrium dynamics the hydrodynamic prescription is not valid here. For these phases a microscopic transport approach based on the Boltzmann equations is a much more suitable approach. Such a microscopic description has been applied quite successfully to the partonic as well as to the hadronic stage of heavy ion collisions [55, 56, 57]. However, explaining hadronization and the phase transition between the hadronic and the partonic phase on a microscopic level is one of the main issues to be resolved. It is therefore difficult to find an appropriate prescription of the phase transition in such a microscopic approach.

One has to find a way to incorporate, into a single model, a non-equilibrium Boltzmann approach for the initial and final phase and couple this in a physically consistent way to a hydrodynamic description of the dense phase.

Various so called micro+macro hybrid approaches have been launched during the last years. The NEXSpheRIO approach uses initial conditions that are calculated in a nonequilibrium model (NEXUS) followed by an ideal hydrodynamic evolution [58, 59, 60, 61, 62, 63, 64]. In this way event-by-event fluctuations are taken into account and the calculation mimics more realistically the experimental case. For the freeze-out they employ a continuous emission scenario or a standard Cooper-Frye calculation. Other groups, e.g. Hirano et al, Bass/Nonaka, are using smooth Glauber or CGC initial conditions followed by a full three-dimensional hydrodynamic calculation and calculate the freeze-out by a subsequent hadronic cascade. The separation of chemical and kinetic freeze-out and final state interactions like resonance decays and rescatterings are taken into account.

We will apply a transport calculation with an embedded three-dimensional ideal relativistic one-fluid calculation for the hot and dense stage of the reaction, later referred to as the hybrid model. The Ultra-relativistic Quantum Molecular Dynamics Model [65, 66] (in its cascade mode) is used to calculate the initial state of a heavy ion collision for the hydrodynamical evolution [67]. This is done to account for the non-equilibrium dynamics

in the very early stage of the collision.

### 3.1 The UrQMD model

For our investigation, the Ultra-relativistic Quantum Molecular Dynamics model (UrQMD v2.3) [65, 66] is applied to model those parts of a heavy ion collision where one assumes that local thermodynamic equilibrium is not achieved. This non-equilibrium transport approach constitutes an effective solution of the relativistic Boltzmann equation:

$$p^\mu \cdot \partial_\mu f_i(x^\nu, p^\nu) = C_i \quad . \quad (3.1)$$

This equation describes the time evolution of the distribution functions for particle species  $i$  and includes the full collision term on the right hand side. The interaction with external potentials leads to an additional term on the left hand side.

The underlying degrees of freedom are hadrons and strings that are excited in high energetic binary collisions. Mean fields can in principle be taken into account in this framework, but the model is run in the so called cascade mode without inter-particle potentials.

The projectile and target nuclei are initialized according to a Woods-Saxon profile in coordinate space and Fermi momenta are assigned randomly for each nucleon in the rest frame of the corresponding nucleus. The hadrons are propagated on straight lines until the collision criterium is fulfilled. If the covariant relative distance  $d_{\text{trans}}$  between two particles gets smaller than a critical distance that is given by the corresponding total cross section a collision takes place,

$$d_{\text{trans}} \leq d_0 = \sqrt{\frac{\sigma_{\text{tot}}}{\pi}}, \quad \sigma_{\text{tot}} = \sigma(\sqrt{s}, \text{type}). \quad (3.2)$$

Each collision process is calculated in the rest frame of the binary collision. The reference frame that is used for the time ordering of the collisions and later on also for the switchings to and from the hydrodynamic phase is the equal speed-system of the nucleus-nucleus collision (for symmetric systems the equal speed system is identical to the center of mass system).

In UrQMD 55 baryon and 32 meson species, ground state particles and all resonances with masses up to 2.25 GeV, are implemented with their specific properties and interaction cross sections. In addition, full particle-antiparticle symmetry is applied. Isospin symmetry is assumed and only flavor-SU(3) states are taken into account. The elementary cross sections are calculated by detailed balance or the additive quark model or are fitted and parametrized according to the available experimental data. For resonance excitations and decays the Breit-Wigner formalism, utilizing their vacuum properties is employed.

Towards higher energies, the treatment of sub-hadronic degrees of freedom is of major importance. In the present model, these degrees of freedom enter via the introduction of a formation time for hadrons produced in the fragmentation of strings [68, 69, 70]. String excitation and fragmentation is treated according to the Lund model. For hard collisions with large momentum transfer ( $Q > 1.5$  GeV) Pythia is used for the calculation. A phase transition to a quark-gluon state is not incorporated explicitly into the model dynamics. However, a detailed analysis of the model in equilibrium yields an effective equation of state of Hagedorn type [71, 50, 72].

The model has been used in different hybrid models, used for air shower simulations [73, 74, 75, 76, 77, 78] and heavy ion collisions [79, 50, 80, 81, 82].

It also successfully describes the yields,  $p_t$  spectra and flow of various particles in proton-proton, proton-nucleus and nucleus-nucleus collisions [83, 84, 85, 86, 87, 88, 89, 90]. A compilation of results of the actual version UrQMD-2.3 compared to experimental data can be found in [91].

## 3.2 The initial state

The coupling between the UrQMD initial state and the hydrodynamical evolution happens at a time  $t_{\text{start}}$  when the two Lorentz-contracted nuclei have passed through each other:

$$t_{\text{start}} = 2R/\sqrt{\gamma_{\text{c.m.}}^2 - 1} \quad , \quad (3.3)$$

where  $R$  is the radius of the lead nucleus and  $\gamma_{\text{c.m.}}$  the Lorentz gamma factor of the two colliding nuclei in their center of mass frame. At this start time all initial collisions have proceeded, i.e. also the initial baryon currents have decoupled from each other, and it is the earliest time at which local thermodynamical equilibrium may be achieved.

Note that the decoupling of the baryon currents is also reflected in the transparency, which means that the number of net baryons in the central rapidity bin decreases with beam energy. Figure (3.1) shows the rapidity distribution of the net baryon number after the UrQMD initial state for central pb+pb collisions at different beam energies. This shows that the model qualitatively correct reproduces the observed effect of transparency.

To allow for a consistent and numerically stable mapping of the 'point like' particles from UrQMD to the 3-dimensional spatial-grid with a cell size of  $(0.2\text{fm})^3$ , each hadron is represented by a Gaussian with a finite width. I.e. each particle is described by a three-dimensional Gaussian distribution of its total energy-, momentum- (in x-, y-, and z-direction) and baryon number-density. The width of these Gaussians is chosen to be  $\sigma = 1$  fm. A smaller Gaussian widths leads to numerical instabilities (e.g. entropy production) in the further hydrodynamical evolution, while a broader width would smear out the initial fluctuations to a large extent. To account for the Lorentz-contraction of the nuclei

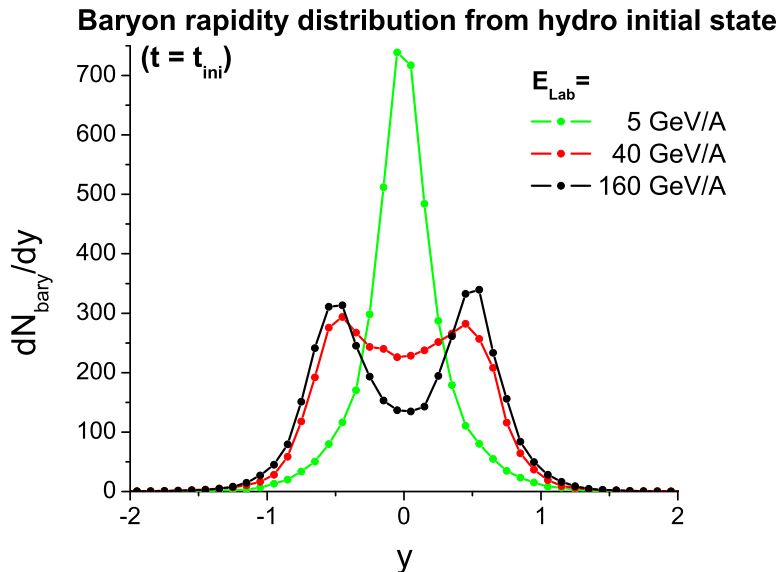


Figure 3.1: The rapidity distribution of the net baryon number after the UrQMD initial state for central pb+pb collisions at different beam energies. The lowest energy shows almost no transparency, while at the highest energy the baryon currents clearly separate in rapidity.

in the longitudinal direction, a gamma-factor (in longitudinal direction) is included.

The resulting distribution function, e.g. for the energy density, then reads:

$$\epsilon_{\text{cf}}(x, y, z) = N \exp \frac{(x - x_p)^2 + (y - y_p)^2 + (\gamma_z(z - z_p))^2}{2\sigma^2}, \quad (3.4)$$

where  $N = (\frac{1}{2\pi})^{\frac{3}{2}} \frac{\gamma_z}{\sigma^3} E_{\text{cf}}$  provides the proper normalization,  $\epsilon_{\text{cf}}$  and  $E_{\text{cf}}$  are the energy density and total energy of the particle in the computational frame, while  $(x_p, y_p, z_p)$  is the position vector of the particle. Summing over all single particle distribution functions leads to distributions of energy-, momentum- and baryon number-densities in each cell.

Instead of smearing out the initial distributions by describing the point like hadrons as Gaussian distributions, one could also obtain a smooth distribution by averaging over a large sample of UrQMD events. On the other hand, our procedure of creating an initial state is motivated by the fact, that experimental results all relate to observed (averaged) final, and not initial, states. To be able to compare to experimental results, where event-by-event fluctuations could be observed, we rather not 'eliminate' these fluctuations by averaging our initial state over a large sample of UrQMD events.

For calculations at finite impact parameter, the spectators - particles that have not interacted until  $t_{start}$  - are propagated separately from the hydrodynamic evolution. They are treated as free streaming particles until the end of the hydrodynamic phase has been reached, but after that may interact with particles coming out of the fluid dynamical phase.

### 3.3 The fluid-dynamic phase

The description of relativistic heavy ion collisions, using the equations of fluid dynamics has a longstanding tradition, beginning with Fermi and Landau [92, 93, 94, 95]. Especially collective effects can be elegantly described by fluid-dynamical approaches [96, 97, 98, 99, 100, 101, 101]. An important condition for the applicability for ideal fluid-dynamics is that the system has to be in local thermodynamic equilibrium at any time. This is of course an idealized situation and any real fluid will deviate from the ideal case. Especially in heavy ion collisions, where the bulk expansion happens on very small timescales this condition is no necessary even close to be fulfilled. Nevertheless recent experiments at the RHIC facility have claimed to have found a (s)QGP that behaves like a nearly ideal fluid, and the idea of modeling heavy ion collisions with (ideal) fluid dynamics has been revived [102, 103, 104].

The equations for relativistic fluid-dynamics are:

$$\partial_\mu T^{\mu\nu} = 0 \quad (3.5)$$

for the conservation of energy and momentum, and:

$$\partial_\mu N^\mu = 0 \quad (3.6)$$

for the conservation of the baryonic charge.  $T^{\mu\nu}$  is the relativistic energy momentum tensor and  $N^\mu$  the baryon four-current. In ideal fluid-dynamics these can be written as:

$$T^{\mu\nu} = (\epsilon + p)u^\mu u^\nu - pg^{\mu\nu} \quad (3.7)$$

$$N^\mu = nu^\mu \quad (3.8)$$

where  $\epsilon$ ,  $p$  and  $n$  are the energy density, pressure and net baryon number density in the local rest frame of the fluid.  $u^\mu$  is the four velocity of the fluid with respect to a reference frame and  $g^{\mu\nu}$  is the metric tensor. To close this system of equations one needs an additional input which is usually referred to as the equation of state of the form  $p = p(\epsilon, n)$ , where  $p$  is the pressure:

$$\frac{\partial N^0}{\partial t} + \nabla \cdot (N^0 \vec{v}) = 0 \quad (3.9)$$

$$\frac{\partial T^{00}}{\partial t} + \nabla \cdot (T^{00} \vec{v}) = -\nabla \cdot (p \vec{v}) \quad (3.10)$$

$$\frac{\partial T^{0i}}{\partial t} + \frac{\partial}{\partial x_i} \left( \sum_i T^{0i} v_i \right) = -\frac{\partial}{\partial x_i} p \quad (3.11)$$



To solve this set of equations we use a SHASTA (SHarp And Smooth Transport Algorithm) program code as described in [105]. This numerical code solves equations (3.9) on a numerical euclidean grid of 200 grid points in every spatial direction. The length of a 3 dimensional cubical cell is 0.2 fm which leads to time steps of  $dt = 0.08$  fm in order to avoid non-causal effects in the propagation (Courant criterion).

Although ideal fluid dynamics models have been very successful in describing data from experiments at the RHIC (see e.g. [106] ) a next step would be to allow deviations from the equilibrium assumption in our hybrid model. This would mean that we have to introduce a viscous (see Appendix C) fluid dynamics code in our model. Such codes, in full 3+1 dimension, are currently under development and the inclusion of such a viscous fluid dynamics description in the hybrid model is subject of future investigation.

### 3.4 The freezeout and final state

After the system dilutes the particles are expected to decouple, which is called the freeze out process. From this point on the fluid-dynamical description is not valid anymore as the system is now very far from local thermodynamic equilibrium. One then has to find a hypersurface at which all the fluid elements of the hydrodynamical evolution are transformed back into the known hadrons which are then propagated in the hadronic cascade of UrQMD. This is in fact a non-trivial task as one needs to conserve all relevant quantities like energy baryon number and the entropy. In general one also distinguishes between a chemical and thermal freeze out. The first being the point when the chemical composition of the system is finally fixed (i.e. particle ratios) and the latter being the point of the last scatterings for the produced particles. In our model the so called freeze out is rather the transition from the fluid-dynamical description to the non-equilibrium transport approach, after which the particles decouple dynamically.

This transition point has to be defined in a reasonable way. In our model we assume that this transition occurs at some fixed energy density ( $\approx 4$  to 5 times the nuclear ground state density). This corresponds to a curve in the  $T - \mu_b$ -plane where the phase transition between hadrons and quarks is expected. In this transition region the fluid-dynamical and transport description should both be valid approaches.

When such a transition hypersurface is defined, the fluid-dynamical fields can then be mapped to hadrons according to the Cooper-Frye prescription [107]:

$$E \frac{dN}{d^3p} = \int_{\sigma} f(x, p) p^{\mu} d\sigma_{\mu} \quad (3.12)$$

where  $f(x, p)$  are the boosted Fermi or Bose distributions of the respective particle species and  $d\sigma_{\mu}$  is a normal vector of the hypersurface. Serving as an input for the distribution functions are the temperature and particle species dependent chemical potentials. These parameters follow from the equation of state as a function of the densities (i.e.  $T = T(\epsilon, \rho)$ )

and  $\mu_i = \mu_i(\epsilon, \rho)$ . In general one would define such a hypersurface as the 3-dimensional surface between cells that are above and below this criterion. In practice, finding this hypersurface numerically, especially when the density is a fluctuating function, can be numerically very challenging. We therefore restricted our model to two different much simpler freeze out hypersurfaces. The first being the isochronous freeze out (IF) the second being the gradual freeze out (GF). Both will be discussed in turn.

1. Isochronous freeze out (IF):

The hydrodynamic evolution is stopped, if the energy density of all cells drops below five (or four) times the ground state energy density (i.e.  $\sim 730\text{MeV}/\text{fm}^3$  for five times). The hydrodynamic fields are mapped to particle degrees of freedom via the Cooper-Frye equation on an isochronous hyper-surface. This means that  $d\sigma_\mu = (dV, 0, 0, 0)$ . The advantage of this prescription is, that energy, momentum and particle number is fully conserved on the transition hypersurface, which is easily constructed numerically. As the evolution is stopped at a fixed point in time (in the computational frame) the temperature and chemical potentials do not take a fixed value but rather have a distribution as a function of coordinate space.

This method however has a shortcoming if the beam energy for the heavy ion collision exceeds  $40A$  GeV. At those energies the time in the local rest frame of the matter which is flowing in beam direction exhibits a strong Lorentz dilatation. The matter at large rapidities therefore has less proper time to cool down as the matter at mid-rapidity (the hydrodynamic calculation is performed in the center-of-mass frame of the collision and the time is measured in this frame), which leads to a non-flat distribution of the freeze out temperature as a function of rapidity.

2. Gradual freeze out (GF):

To account for the large time dilatation at large rapidities we also introduced a slightly different freeze out procedure called the gradual freeze out. At higher energies (above  $40A$  GeV) the isochronous hypersurface increasingly differs from an iso- $\tau$  hypersurface ( $\tau$  is the proper time). To mimic an iso- $\tau$  hypersurface we therefore freeze out full transverse slices, of thickness  $\Delta z = 0.2\text{fm}$ , whenever all cells of that slice fulfill our freeze-out criterion. By doing this we obtain a rapidity independent freeze-out temperature even for the highest beam energies. For lower energies the two procedures yield identical results for the temperature distributions.

The hydrodynamic fields, in a given slice, are transformed to particle degrees of freedom via the Cooper-Frye equation on an isochronous time-like hypersurface in the computational frame (the hypersurface normal is again  $d\sigma_\mu = (dV, 0, 0, 0)$ ).

As different longitudinal slices have different freeze out times,  $d\sigma_\mu$  should of course also have a space like component. Such a parametrization of the hypersurface is not easily dealt with numerically (especially since our system has locally fluctuating densities and therefore an inhomogeneous hypersurface). In a realistic set up, where the longitudinal expansion of the system is about 10 fm, we obtain a total difference in particle production of about 10% when compared with an analytically solvable Bjorken scenario. The error in particle production per rapidity interval grows for larger rapidities. In consequence, we expect the calculated rapidity distributions, of particles produced at the highest SPS energies ( $E_{\text{lab}} = 160A$  GeV), to show the largest effect of our choice of  $d\sigma_\mu$ . More precisely, we expect the present rapidity distributions at the highest energies to be lower at mid-rapidity and broader at high rapidities, as compared to results with the correct  $d\sigma_\mu$ . As a remark, it is possible to numerically extract the correct parametrization of the full hypersurface using digital image processing techniques [3], and then compare these results with data acquired with our simplified hypersurface.

The actual production of the hadronic particles is based on a Monte Carlo sampling of Eqn. 3.12, on the predefined hypersurface, and follows the general steps:

1. The particle numbers  $N_i$  are calculated according to the following formula,

$$N_i = n_i \cdot \gamma \cdot V_{\text{cell}} = \int d^3p f_i(x, p) \cdot \gamma \cdot V_{\text{cell}} \quad (3.13)$$

where the index  $i$  runs over the different particle species like, e.g.,  $\pi$ , p,  $\rho$  or  $\Delta$ .  $\gamma$  is the boost factor between the computational frame and the cell.  $V_{\text{cell}}$  is the volume of the cell in the computational frame and  $n$  is the particle number density. All cells with temperatures that are lower than 3 MeV are discarded from the following procedure because of numerical reasons. The local rest frame equilibrium distribution function is denoted by  $f_i(x, p)$ . To simplify the calculation, a relativistic Boltzmann distribution is used for all particles, except pions.

$$f_i(x, p) \propto \exp(-(E_i - \mu_i)/T) \quad (3.14)$$

It has been checked, that the relativistic Boltzmann approximation is sufficient to describe all particle species it is applied to. For the Boltzmann distribution the momentum integration leads to the following result for the particle number density

$$n_i = \frac{4\pi g m^2 T}{(2\pi)^3} \exp\left(\frac{\mu}{T}\right) K_2\left(\frac{m}{T}\right) \quad (3.15)$$

where  $g$  is the degeneracy factor for the respective particle species,  $m$  is the mass of the particle to be produced,  $T$  the temperature of the cell and  $K_2$  is the modified Bessel function. The chemical potential  $\mu$  includes the baryo-chemical potential and the strangeness chemical potential in the following way

$$\mu = B \cdot \mu_B + S \cdot \mu_S \quad (3.16)$$

where  $S$  is the quantum number for strangeness and  $B$  is the baryon number.

For pions the Bose distribution has to be taken into account because the pion mass is on the order of the temperature of the system. In this case, the momentum integration involves an infinite sum over modified Bessel functions

$$n_\pi = \frac{g_\pi m_\pi^2 T}{(2\pi)^2} \sum_{k=1}^{\infty} \frac{1}{k} K_2 \left( \frac{km_\pi}{T} \right). \quad (3.17)$$

To calculate the number of particles in the computational frame the particle number density has to be multiplied with the Lorentz-stretched volume of the cell ( $V_{\text{cell}} = (0.2)^3 \text{fm}^3$ ).

2. The average total number of particles in the cell,  $\langle N \rangle$ , is the sum over all particle numbers  $N_i = n_i \gamma V_{\text{cell}}$

$$\langle N \rangle = \sum_i N_i. \quad (3.18)$$

3. The total number of particles emitted from a cell,  $N_i$ , is obtained from a Poisson distribution according to  $P(N) = \frac{\langle N \rangle^N}{N!} e^{-\langle N \rangle}$ .

In the limit of small mean values, the Poisson distribution becomes  $P(1) \approx \langle N \rangle$ . Thus it can be decided by one random number between 0 and 1 if a particle is produced in the respective cell. If the random number is smaller than  $\langle N \rangle$  one particle is produced and there is no particle production otherwise. The full Poisson distribution is used, if the particle number  $\langle N \rangle$  is larger than (0.01). This assures an accuracy better than 1 %.

4. The particle type is chosen according to the probabilities  $N_i/\langle N \rangle$ .
5. The  $I_3$  component of the isospin is distributed randomly because UrQMD assumes full isospin symmetry. To conserve the overall charge of the system and the initial isospin-asymmetry the probability to generate the isospin component that leads to the right value of the charge that should be obtained in the end is favored. The other isospin components are exponentially suppressed. The power of the exponential is proportional to the difference of the total charge generated by this produced particle and the required value  $\exp -(|\Delta Q_{\text{new}}| - |\Delta Q_{\text{old}}|)$ , where  $\Delta Q$  is the charge difference.
6. The 4-momenta of the particles are generated according to the Cooper-Frye equation (see Eqn. 3.12). For baryons and strange mesons the chemical potentials for baryon number and strangeness are taken into account.

7. The particle vector information is transferred back into the UrQMD model. The subsequent hadronic cascade calculation incorporates important final state effects as, e.g., rescatterings of the particles and resonance decays.

The particle production is done in a sequence to ensure that all important quantum numbers as energy, baryon number, electric charge and strangeness are fully conserved. Note that while the charges (electric, baryon and strange charge) are interger values which can be conserved exactly, the energy is not. As we do not want to artificially rescale any particle momenta to not introduce any bias in momentum dependend observables, the last partical which is produced by our freeze out routine will usually violate energy conservation (either to much or to few energy). Nevertheless we have checked the the violation on an event-by-event basis is less than 0.01% and that the energy is fully conserved when averaged over many events.

After the particles are created according to our prescription, they proceed in their evolution in the hadronic cascade (UrQMD) where rescatterings and final decays are calculated until all interactions cease and the system decouples.



# Chapter 4

## The EoS

Serving as an input for the fluid dynamical calculation the equation of state (EoS) strongly influences the dynamics of an expanding system. Since the actual EoS of hot and dense QCD matter is still not precisely known, it may seem disadvantageous to have this additional uncertainty in the model. On the contrary it may prove to be an important trait of the model to be able to study changes on the dynamics of the bulk matter when changing the EoS thus finding observables for a phase transition in hot QCD matter.

In QCD one can define two different phase transitions, the first being the chiral phase transition associated with chiral symmetry restoration in the vanishing quark mass limit, where the chiral condensate serves as a well defined order parameter. In the limit of heavy quarks, a deconfinement phase transition with the Polyakov loop as order parameter, is assumed. Physical quarks however have intermediate masses and one would expect that at least the deconfinement order parameter is not so well defined anymore. There could even be some mixing of the two order parameters, accounting for some lattice QCD observation that deconfinement and chiral restoration occur at the same temperature (at least at  $\mu_B = 0$ ) [108, 109, 110, 111, 112].

Such lattice calculations at finite temperature are an important tool for the investigation of the QCD phase diagram. For the thermodynamics of the pure gauge theory high accuracy data is available [113], and the equation of state (EoS) of strongly interacting matter at vanishing chemical potential is reasonably well understood [114, 115]. Here lattice predicts a rapid crossover for the deconfining and chiral phase transitions.

At finite baryo-chemical potential, lattice calculations suffer from the so called sign problem. There are several different approaches to obtain results at finite  $\mu_B$  [116, 112, 117, 118, 119, 120, 121, 122], but yet no clear picture, especially about the existence and location of a possible critical end point, has emerged.

Recent considerations based on connecting the large  $N_c$  limit with real-world QCD draw an even more exotic picture of the phase diagram, where the critical temperatures of the

deconfinement and chiral phase transitions disconnect and depart in the region of high net baryon densities [123].

In the following we will discuss the different equations of state we have developed and introduced in the hybrid model. Since the actual first principle calculation of the EoS of QCD is still in its fledgling states we have to rely on effective models that incorporate fundamental properties of QCD and then try to draw conclusions from thereon.

## 4.1 The Hadron Resonance Gas (HRG)

Besides the stable hadrons of the lowest multiplets (see section 2.2.1) there exists a multitude of excited states of hadrons. These states have usually a lifetime of the order of several  $fm/c$ . Many states are well known and measured up to high precision but because of their large width, numerous are not very well defined (for a list of all known and probable states see [14]). In a hadronic system at high temperature one would expect such resonant states to be created and destroyed incessantly. Therefore the equation of state of QCD, at large temperatures, but below the deconfinement phase transition, should be well described by a gas of hadronic resonances. This argument is supported by the fact that many thermal models, including all more or less reliably known masses are able to explain the particle multiplicities as they are measured at heavy ion experiments [191, 193, 271, 192, 272].

There are even attempts to combine results on thermodynamics from the lattice with those from a hadronic resonance gas which is expected to be the correct description of matter below  $T_c$  [124].

In the following we will use a hadron gas which is comprised of all reliably known hadronic resonances with masses up to 2.2 GeV. This represents the same degrees of freedom as are included in the UrQMD model. The thermodynamic quantities then simply follow from the integration of the corresponding Fermi and Bose distributions:

$$\begin{pmatrix} \epsilon_i \\ P_i \\ n_i \end{pmatrix} = \frac{g_i}{2\pi^2} \int_{m_i}^{\infty} d\epsilon \frac{\sqrt{\epsilon^2 - m_i^2}}{\exp\left(\frac{\epsilon - \mu_i}{T}\right) \pm 1} \begin{pmatrix} \epsilon^2 \\ \frac{1}{3}(\epsilon^2 - m_i^2) \\ \epsilon \end{pmatrix}, \quad (4.1)$$

where  $m_i$  is the mass of the  $i$ -th hadron and  $g_i$  its degeneracy. The entropy density  $s$  then follows from the Euler relation:

$$e = -p + sT + \sum_i \mu_i \rho_i \quad (4.2)$$

The HRG is a very important ingredient of the hybrid model, because the active degrees of freedom on both sides of the transition hypersurface have to be equivalent to ensure the conservation of important quantities (e.g. entropy). For the HRG this is the case, as it has the same degrees of freedom as the UrQMD model. In any other EoS the hadrons



acquire effective masses due to interactions, or the model even includes quark and gluonic degrees of freedom, and therefore this equivalence condition is only approximately fulfilled. To solve this problem we change the active equation of state after the last step of the hydrodynamical evolution (from any other EoS to the HRG), thus obtaining the correct temperatures and chemical potentials for the particle distributions at the freeze out.

### 4.1.1 Including quarks

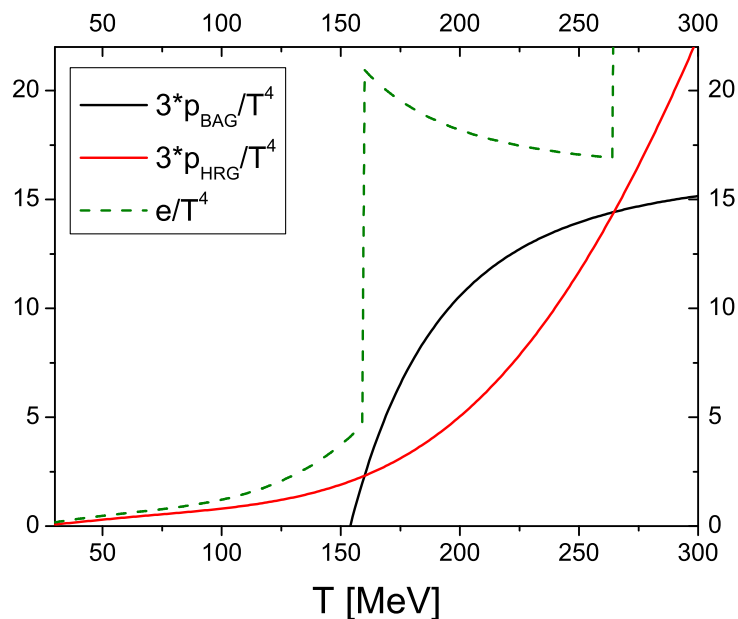


Figure 4.1: Three times the pressure over  $T^4$  as a function of the temperature at  $\mu_B = 0$  for the HRG (red line) and QGP (black line). The green line is the energy density over  $T^4$  for the phase construction and clearly shows two discontinuities at  $T_{c1} \approx 160 \text{ MeV}$  and  $T_{c2} \approx 270 \text{ MeV}$ .

Early on there have been attempts to incorporate a QGP phase into hadronic models. This is usually done via a Maxwell construction. This means that one calculates the pressure as a function of temperature and chemical potential for both the hadronic and QGP phase and then assumes that the stable phase is the one with the larger pressure.

For the pressure in the QGP phase one can apply a standard MIT bag model [125] with 3 massless quark flavors:

$$p_{\text{QGP}}(T, \mu_B) = \frac{11\pi^2}{20} T^4 + \frac{1}{9} \mu_B^2 T^2 + \frac{1}{162\pi^2} \mu_B^4 - B, \quad (4.3)$$

where  $\mu_B = 3\mu_q$  is the baryon chemical potential and  $B = (235 \text{ MeV})^4$  is the bag constant. The pressure of the HRG is calculated as shown in equation (4.1). Figure (4.1) shows the pressure over  $T^4$  for both the QGP (black curve) and the HRG (red curve) as a function of the temperature at  $\mu_B = 0$ . Both curves intersect at  $T \approx 160 \text{ MeV}$  which would then correspond to the critical temperature  $T_c$  of a first order phase transition. This means that the order parameter on the phase transition (in this case this is the energy density depicted as the green dashed line) exhibits a discontinuity at  $T_c$ . The problem that occurs when matching a HRG to a QGP comes obvious when one continues to increase the temperature. As can be seen in in figure (4.1) there is a second intersection point at which the pressure of the HRG again becomes larger than the pressure of the QGP. Eventually one could circumvent this problem by simply ignoring this second phase transition, as hadrons should not exist above the first critical temperature.

Continuing this procedure to finite chemical potentials reveals the true shortcoming of this model. As the chemical potential increases more and more baryonic resonances become thermodynamically activated. This means that for some finite value of  $\mu_B = 3\mu_q$  the pressure of the HRG is always larger than the pressure of the quark gluon plasma and therefore no phase transition occurs. Figure 4.2 shows the phase diagram in the  $T - \mu_B$ -plane as it results from our considerations. One can see the line of the first order phase transition and the grey region in which the QGP is the stable phase. Above a chemical potential of  $\mu_b \approx 600 \text{ MeV}$  the HRG is the stable phase for any value of  $T$ .

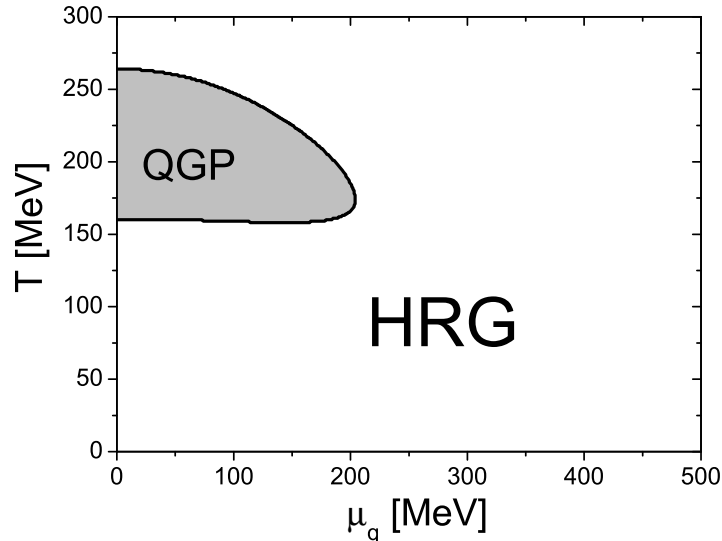


Figure 4.2: Phase diagram for a HRG + QGP phase construction. The solid line depicts the phase transition line of first order between the HRG phase and the QGP phase.

### 4.1.2 Excluded volume corrections

The discussed problem can eventually be overcome if one introduces a repulsive hadronic interaction. In [126] these interactions are provided by a hard-core van der Waals repulsive interaction. It follows from the fact that hadrons, instead of being point like, have a finite volume:

$$v = \frac{1}{2} \cdot \frac{4}{3} \pi (2r)^3 \quad (4.4)$$

Including the effects of finite hadron volumes leads to a correction of the  $i$ 'th particles chemical potential:

$$\tilde{\mu}_i = \mu_i - v_i P \quad (4.5)$$

where  $P$  is the sum over all partial pressures. All thermodynamic quantities can then be calculated with respect to the temperature  $T$  and the new chemical potentials  $\tilde{\mu}_i$ . To be thermodynamically consistent, all densities ( $\tilde{e}_i$ ,  $\tilde{\rho}_i$  and  $\tilde{s}_i$ ) have to be multiplied by a volume correction factor  $f$ , which is the ratio of the total volume  $V$  and the reduced volume  $V'$ , not being occupied:

$$f = \frac{V'}{V} = (1 + \sum_i v \rho_i)^{-1} \quad (4.6)$$

The actual densities then are:

$$e = \sum_i f \tilde{e}_i \quad (4.7)$$

$$\rho_i = f \tilde{\rho}_i \quad (4.8)$$

$$s = \sum_i f \tilde{s}_i \quad (4.9)$$

This procedure effectively reduces the active hadronic degrees of freedom and therefore the pressure as a function of temperature for the HRG. Nevertheless this approach still has some weaknesses.

The first is that the applied excluded volume approach is not valid if the hadrons are packed to close together. As this is a classical approach this means that at large chemical potential (large baryon densities), this leads to superluminal speeds of sound which is unphysical. Secondly, this type of model still is based on a strict separation of phases, the HRG on the one side and the QGP on the other. This means that the phase transition will always be of first order. Lattice studies at  $\mu_B = 0$  on the other hand suggest a very smooth crossover which could never be realized in such a model. To model such a crossover, both asymptotic degrees of freedom, hadrons and free quarks, must be included in a self-consistent model with a single partition function. Our aim was to supply such a model which will be described in the following sections.

## 4.2 The Chiral hadronic model

In our approach we derive the EoS of hot and dense nuclear matter using a single model for the hadronic and quark phase [127, 128, 129, 130]. The model includes the correct asymptotic degrees of freedom, namely a free gas of quarks and gluons at infinite temperature, and a gas of hadrons having the correct vacuum properties at vanishing temperature. The model also predicts the structure of finite nuclei, nuclear and neutron matter properties and a first order liquid-vapor phase transition. The two phase transitions that are expected from QCD, the chiral and deconfinement transitions, are also included in a consistent manner.

In the following we will show how we describe the different phases of QCD and how we combine them in a single model.

We describe the hadronic part of the EoS, using a flavor-SU(3) model which is an extension of a non-linear representation of a sigma-omega model including the pseudo-scalar and vector octets of mesons and the baryonic octet and decuplet ([131, 132, 133]).

The Lagrangian density of the model in mean field approximations reads:

$$L = L_{kin} + L_{int} + L_{meson}, \quad (4.10)$$

where besides the kinetic energy term for hadrons, the terms:

$$L_{int} = - \sum_i \bar{\psi}_i [\gamma_0 (g_{i\omega} \omega + g_{i\phi} \phi) + m_i^*] \psi_i, \quad (4.11)$$

$$\begin{aligned} L_{meson} = & -\frac{1}{2}(m_\omega^2 \omega^2 + m_\phi^2 \phi^2) \\ & -g_4 \left( \omega^4 + \frac{\phi^4}{4} + 3\omega^2 \phi^2 + \frac{4\omega^3 \phi}{\sqrt{2}} + \frac{2\omega \phi^3}{\sqrt{2}} \right) \\ & + \frac{1}{2}k_0(\sigma^2 + \zeta^2) - k_1(\sigma^2 + \zeta^2)^2 \\ & - k_2 \left( \frac{\sigma^4}{2} + \zeta^4 \right) - k_3 \sigma^2 \zeta \\ & + m_\pi^2 f_\pi \sigma \\ & + \left( \sqrt{2} m_k^2 f_k - \frac{1}{\sqrt{2}} m_\pi^2 f_\pi \right) \zeta, \\ & + \chi^4 - \chi_0^4 + \ln \frac{\chi^4}{\chi_0^4} - k_4 \frac{\chi^4}{\chi_0^4} \ln \frac{\sigma^2 \zeta}{\sigma_0^2 \zeta_0}. \end{aligned} \quad (4.12)$$

represent the interactions between baryons and vector and scalar mesons, the self-interactions of scalar and vector mesons, and an explicitly chiral symmetry breaking term. The index  $i$  denotes the baryon octet and decuplet. Here, the mesonic condensates (determined in mean-field approximation) included are the vector-isoscalars  $\omega$  and  $\phi$ , and the scalar-isoscalars  $\sigma$  and  $\zeta$  (strange quark-antiquark state). Assuming isospin symmetric matter, we can neglect the  $\rho$ -meson contribution in Eq. 4.12.

The last four terms of (4.12) were introduced to model the QCD trace anomaly [132], where the dilaton field  $\chi$  can be identified with the gluon condensate (See Appendix B for a detailed discussion on the trace anomaly and scale invariance).

The effective masses of the baryons (of the octet) are generated by the scalar mesons except for an explicit mass term ( $\delta m_N = 120$  MeV):

$$m_b^* = g_{b\sigma}\sigma + g_{b\zeta}\zeta + g_{b\chi}\chi + \delta m_b, \quad (4.13)$$

while, for simplicity and in order to reduce the number of free parameters, the masses of the decuplet baryons are kept at their vacuum expectation values. Since the dilaton is essentially frozen in the nuclear ground state, the couplings of the baryons to the dilaton ( $\chi$ ) is introduced to keep the bare mass of the nucleon small and still retain a moderate value for the sigma-coupling strength. With the increase of temperature/density, the  $\sigma$  field (non-strange chiral condensate) decreases its value, causing the effective masses of the particles to decrease towards chiral symmetry restoration. The coupling constants for the baryons [134] are chosen to reproduce the vacuum masses of the baryons, nuclear saturation properties and asymmetry energy as well as the  $\Lambda$ -hyperon potentials. The vacuum expectation values of the scalar mesons are constrained by reproducing the pion and kaon decay constants. (See tables 4.1 - 4.3 for the explicit values of the model parameters)

### 4.3 The PNJL model

In contrast to the chiral hadronic models, the PNJL model was introduced in [135, 136] as an effective chiral quasi-quark model that incorporates a mean field like coupling to a color background field. It has often been shown to reproduce many general features of lattice results at  $\mu_B = 0$  [137, 138, 139, 140, 141, 142, 143, 144, 145, 146, 147, 148, 149, 150, 151, 152, 153, 154, 155, 156, 157, 158]. In later comparisons we will use a very basic parametrization of the two-flavor PNJL model and extend it to incorporate a repulsive vector interaction. The thermodynamic potential of our parametrization reads:

$$\Omega = U(\Phi, \Phi^*, T) + \sigma^2/2G_S - \omega^2/2G_V - \Omega_q \quad (4.14)$$

with

$$\begin{aligned} \Omega_q &= 2N_f \int \frac{d^3p}{(2\pi)^3} \left\{ T \ln \left[ 1 + 3\Phi e^{-(E_p - \mu_q^*)/T} + 3\Phi^* e^{-2(E_p - \mu_q^*)/T} + e^{-3(E_p - \mu_q^*)/T} \right] \right. \\ &\quad + T \ln \left[ 1 + 3\Phi^* e^{-(E_p + \mu_q^*)/T} + 3\Phi e^{-2(E_p + \mu_q^*)/T} + e^{-3(E_p + \mu_q^*)/T} \right] \\ &\quad \left. + 3\Delta E_p \Theta(\Lambda^2 - \vec{p}^2) \right\} \end{aligned} \quad (4.15)$$

Where  $\Phi$  is the traced Polyakov loop after averaging:

$$\Phi = 1/3 Tr \langle L \rangle = 1/3 Tr e^{i\phi/T} \quad (4.16)$$

where the Wilson line is a  $3 \times 3$  matrix in the fundamental representation in color space defined as:

$$L(\vec{x}) = \mathcal{P} \exp \left( i \int_0^\beta A_4 dx_4 \right) \quad (4.17)$$

The dynamical mass of the quarks  $m = m_0 - \sigma = m_0 - G_S \langle \bar{\Psi} \Psi \rangle$  is the same as in the NJL model and the vector coupling induces an effective chemical potential for the quarks  $\mu_q^* = \mu_q + \omega = \mu_q + G_V \langle \Psi^\dagger \Psi \rangle$ . The two auxiliary fields  $\sigma$  and  $\omega$  are controlled by the potential terms and the last term includes the difference  $\Delta E_p$  between the quasi particle energy and the energy of free quarks. The NJL part of the model has 4 parameters, the bare quark mass for the  $u$ - and  $d$ -quarks (assuming isospin symmetry), the three-momentum cutoff of the quark-loop integration  $\lambda$  and the coupling strengths  $G_S$  and  $G_V$ . To reproduce realistic values for the pion mass and decay constant as well as the chiral condensate, we take these values to be [136]:  $m_{u,d} = 5.5$  MeV,  $G_S = 10.08$  GeV<sup>-2</sup>,  $\Lambda = 651$  MeV ( $G_V$  will be left as a model parameter to study the influence of the vector coupling on our results). The thermodynamics of  $\Phi$  (and  $\Phi^*$ ) are controlled by the effective potential  $U(\Phi, \Phi^*, T)$  [159]:

$$U = -\frac{1}{2}a(T)\Phi\Phi^* + b(T) \ln[1 - 6\Phi\Phi^* + 4(\Phi^3\Phi^{*3}) - 3(\Phi\Phi^*)^2] \quad (4.18)$$

with  $a(T) = a_0T^4 + a_1T_0T^3 + a_2T_0^2T^2$ ,  $b(T) = b_3T_0^3T$ .

This choice of effective potential satisfies the  $Z(3)$  center symmetry of the pure gauge Lagrangian. In the confined phase,  $U$  has a minimum at  $\Phi = 0$ , while above the critical Temperature  $T_0$  its minimum is shifted to finite values of  $\Phi$ . The logarithmic term appears from the Haar measure of the group integration with respect to the SU(3) Polyakov loop matrix. The parameters  $a_0, a_1, a_2$  and  $b_3$  are fixed, as in [159], by demanding a first order phase transition in the pure gauge sector at  $T_0 = 270$  MeV, and that the Stefan-Boltzmann limit is reached for  $T \rightarrow \infty$ . The self consistent solutions are obtained by minimizing the thermodynamic potential with respect to the fields  $\sigma, \omega, \Phi$  and  $\Phi^*$ .

PNJL-type models have been used recently to successfully describe lattice results on bulk properties of a strongly interacting matter [135, 136]. These constituent quark models seem to have the correct degrees of freedom in the asymptotic regime of free quarks and gluons but lack the rich hadronic spectrum.

## 4.4 Including quarks in the chiral model

In our approach (later referred to as the Quark-Hadron model) we combine, in a single model, a well-established flavor-SU(3) hadronic model with a PNJL-type quark-gluon description of the highly excited matter. This allows us to study the chiral-symmetry and confinement-deconfinement phase structure of the strongly interacting matter at high temperatures and densities. In addition we obtain an equation of state of hadronic and quark

matter that is applicable over a wide range of thermodynamical conditions and that can therefore be used in heavy-ion simulations with very different beam energies.

The extension of the hadronic SU(3) model to quark degrees of freedom is constructed in analogy to the PNJL model. The sigma model uses the Polyakov loop  $\Phi$  as the order parameter for deconfinement.  $\Phi$  is defined via  $\Phi = \frac{1}{3}\text{Tr}[\exp(i \int d\tau A_4)]$ , where  $A_4 = iA_0$  is the temporal component of the SU(3) gauge field. One should note that one must distinguish  $\Phi$ , and its conjugate  $\Phi^*$  at finite baryon densities [160, 112, 161], as they couple differently to the quarks, respective antiquarks.

In our approach the effective masses of the quarks are generated by the scalar mesons except for a small explicit mass term ( $\delta m_q = 5$  MeV and  $\delta m_s = 105$  MeV for the strange quark):

$$\begin{aligned} m_q^* &= g_{q\sigma}\sigma + \delta m_q, \\ m_s^* &= g_{s\zeta}\zeta + \delta m_s, \end{aligned} \quad (4.19)$$

with values of  $g_{q\sigma} = g_{s\zeta} = 4.0$ .

Vector type interactions introduce an effective chemical potential for the quarks and baryons, generated by the coupling to the vector mesons:

$$\mu_i^* = \mu_i - g_{i\omega}\omega - g_{i\phi}\phi \quad (4.20)$$

A coupling of the quarks to the Polyakov loop is introduced in the thermal energy of the quarks. Their thermal contribution to the grand canonical potential  $\Omega$ , can then be written as:

$$\Omega_q = -T \sum_{i \in Q} \frac{\gamma_i}{(2\pi)^3} \int d^3k \ln \left( 1 + \Phi \exp \frac{E_i^* - \mu_i^*}{T} \right) \quad (4.21)$$

and

$$\Omega_{\bar{q}} = -T \sum_{i \in Q} \frac{\gamma_i}{(2\pi)^3} \int d^3k \ln \left( 1 + \Phi^* \exp \frac{E_i^* + \mu_i^*}{T} \right) \quad (4.22)$$

The sums run over all quark flavors, where  $\gamma_i$  is the corresponding degeneracy factor,  $E_i^*$  the energy and  $\mu_i$  the chemical potential of the quark. Note that we neglect the 2 and 3 quark contributions present in the PNJL model.

All thermodynamical quantities, energy density  $e$ , entropy density  $s$  as well as the densities of the different particle species  $\rho_i$ , can be derived from the grand canonical potential. In our model it has the form:

$$\frac{\Omega}{V} = -L_{int} - L_{meson} + \frac{\Omega_{th}}{V} - U \quad (4.23)$$

Here  $\Omega_{th}$  includes the heat bath of hadronic and quark quasi particles. The effective potential  $U(\Phi, \Phi^*, T)$  which controls the dynamics of the Polyakov-loop was discussed in the previous section. In our approach we adopt the ansatz (4.18) proposed in [136].

Note that  $T_0$  remains a free parameter to adjust the actual critical temperature, of both phase transitions, when both, quarks and hadrons, couple to the scalar fields.

As has been mentioned above, the Lagrangian of the chiral model contains dilaton terms to model the scale anomaly. These terms constrain the chiral condensate, if the dilaton is frozen at its ground state value  $\chi_0$ . On the other hand, as deconfinement is realized, the expectation value of the chiral condensate should vanish at some point. On account of this we can couple the Polyakov loop to the dilaton in the following way:

$$\chi = \chi_0 (1 - 0.5(\Phi\Phi^*)) \quad (4.24)$$

Here we assume a hard part for the dilaton field, which essentially stays unchanged over a wide range of temperatures, and a soft part which vanishes when deconfinement is realized. Hence, allowing the chiral condensate to also approach zero.

Until now all hadrons are still present in the deconfined and chirally restored phase. Since we expect them to disappear, at least at some point above  $T_c$ , we have to include a mechanism that effectively suppresses the hadronic degrees of freedom, when deconfinement is achieved.

In previous calculations baryons were suppressed by introducing a large baryon mass shift for non-vanishing  $\Phi$  [134].

In the following the suppression mechanism will be provided by excluded volume effects as discussed above. Including effects of finite-volume particles, in a thermodynamic model for hadronic matter, was proposed some time ago [162, 163, 164, 165]. We will use an ansatz similar to that used in [166, 167](see section 4.1.2), but modify it to also treat the point like quark degrees of freedom consistently.

If one introduces a particle of radius  $r$  into a gas of the same particles, then the volume excluded is not just the simple spherical volume, but one-half times the volume of a sphere with radius  $2r$ :

$$v = \frac{1}{2} \cdot \frac{4}{3}\pi(2r)^3 \quad (4.25)$$

It is easy to understand that if all other particles also have a radius  $r$  then the excluded volume is much bigger than just the volume of a single particle.

We expect the volume of a meson to be smaller than of a baryon we have to introduce the quantity  $v_i$  which is the volume excluded of a particle of species  $i$ . Since we only distinguish between baryons, mesons and quarks. Consequently  $v_i$  can only assume three values:

$$\begin{aligned} v_{Quark} &= 0 \\ v_{Baryon} &= v \\ v_{Meson} &= v/a \end{aligned} \quad (4.26)$$



where  $a$  is a number larger than one. In our calculations we assumed it to be  $a = 8$ , which would mean that the radius  $r$  of a meson is half that of a baryon. Note that we neglect any possible Lorentz contraction effects on the excluded volumes as introduced in [168, 169].

The modified chemical potential  $\tilde{\mu}_i$  which is connected to the real chemical potential  $\mu_i$ , of the  $i$ -th particle species, is obtained by the relations 4.5 to 4.7.

Note that in this configuration the chemical potentials of the hadrons are decreased by the quarks, but not vice versa. In other words as the quarks start appearing they effectively suppress the hadrons by changing their chemical potential, while the quarks are only affected through the volume correction factor  $f$ .

Our implementation of finite-volume corrections as outlined above is a simple approach with as few parameters as possible and can be improved upon in various ways. For one, hadrons differ in size. The size of a hadron could even be density or temperature dependent [170]. In addition, the excluded-volume parameter of a particle does also depend on the density of the system (at dense packing a particle excludes effectively less volume). However, one should regard the variables  $v$  and  $a$  as effective parameters for capturing the qualitative effect of an excluded volume correction, which suppresses the hadrons in the quark phase.

We would like to stress that these volume corrections enable us to describe a phase transition from hadronic to quark degrees of freedom, having only one single partition function for both phases, in a thermodynamic consistent manner. Furthermore the volume corrections we apply are physically well motivated and are thoroughly discussed in older and recent literature. They model the fact that hadrons generate a repulsive hard-core interaction for the other particles in the system. This is not necessarily related to confinement. Therefore, a volume correction from the remaining mesons beyond  $T_c$  that also affect the quarks is not a contradiction to the fact that quarks can propagate freely, it is part of the residual interaction in the system, quarks feel repulsion interacting with the mesons. Our description of the excluded volume effects is admittedly simplified and parameter dependent (yet thermodynamically consistent).

The following tables give a summary of the model parameters used in this work:

Particle species $i$	$g_{i\sigma}$	$g_{i\zeta}$	$g_{i\omega}$	$g_{i\phi}$	$g_{i\chi}$	$\delta m_{0i}$
u,d	-4.0	0.0	0.0 - 3.0	0.0	$9.95 \cdot 10^{-2}$	6.0 MeV
s	0.0	-4.0	0.0	0.0 - (-7.39)	$9.95 \cdot 10^{-2}$	105.0 MeV
N	-9.90	1.17	12.01	0.0	0.298	18.0 MeV
$\Lambda$	-5.46	-2.26	8.0	-7.39	0.0	364 MeV
$\Sigma$	-3.95	-4.4	8.0	-7.39	0.0	364 MeV
$\Xi$	-1.61	-7.71	4.0	-14.78	0.0	364 MeV

Table 4.1: Coupling parameters for the hadronic chiral model

$k_0$	$k_1$	$k_2$	$k_3$	$k_4$	$g_4$
2.373	1.39	-5.55	-2.65	-0.226	60.0

Table 4.2: Parameters for the hadronic chiral model

$T_0$	$a_0$	$a_1$	$a_2$	$b_3$
220 MeV	3.51	-2.47	15.2	-1.75

Table 4.3: Parameters for the Polyakov potential

### Different parameterizations of the potential

Although the introduction of the Polyakov loop in a mean field type model like the PNJL gives reasonable results at  $\mu_B = 0$ , there are some issues when going to large chemical potentials and low temperatures. This can be seen if one calculates the entropy contribution of the Polyakov potential:

$$s_{pol} = \frac{\partial p_{pol}}{\partial T} = c(T)\Phi\Phi^* + b_3 T_0^3 \ln(1 - 6\Phi\Phi^* + 4(\Phi^3\Phi^{*3}) - 3(\Phi\Phi^*)^2) \quad (4.27)$$

For  $T = \text{const.}$  and when the value of the Polyakov approaches unity at large values of  $\mu_B$ , this contribution logarithmically goes to minus infinity:  $\Phi \rightarrow 1 \implies s_{pol} \rightarrow -\infty$ .

There has been a popular ansatz to improve the model by making  $U$  depend explicitly on  $\mu_B$ . In this approach (which we will refer to as the DE equation of state) the effective masses of the baryons and quarks are generated by the scalar mesons except for a small explicit mass term and the term containing the Polyakov field  $\Phi$  [134]:

$$m_b^* = g_{b\sigma}\sigma + g_{b\zeta}\zeta + \delta m_b + g_{b\Phi}\Phi^2, \quad (4.28)$$

$$m_q^* = g_{q\sigma}\sigma + g_{q\zeta}\zeta + \delta m_q + g_{q\Phi}(1 - \Phi). \quad (4.29)$$

With the increase of temperature/density, the scalar fields decrease in value, causing the effective masses of the particles to decrease towards chiral symmetry restoration. The Polyakov loop effectively suppresses baryons at high temperatures/densities and quarks at low temperatures/densities due to their corresponding mass shifts shown above.

The new potential  $U$  for the Polyakov loop now reads:

$$U = (a_0 T^4 + a_1 \mu_B^4 + a_2 T^2 \mu_B^2) \Phi^2 + a_3 T_0^4 \ln(1 - 6\Phi^2 + 8\Phi^3 - 3\Phi^4). \quad (4.30)$$

Additional terms, depending on the chemical potential, are fixed in order to reproduce the phase diagram at high densities. This includes a first order phase transition line in  $\mu_q$  and  $T$  that ends in a critical point, of second order, at the values obtained by lattice

calculations [171].

As can be seen in Fig. (4.3) the transition from hadronic to quark matter obtained is a crossover for small chemical potentials. At vanishing chemical potential the transition temperature is 171 MeV, determined as the peak of the change of the scalar field and the Polyakov loop. Beyond the critical end-point (at  $\mu_{c,B} = 354$  MeV,  $T_c = 167$  MeV for symmetric matter in accordance with [171]) a first order transition line begins.

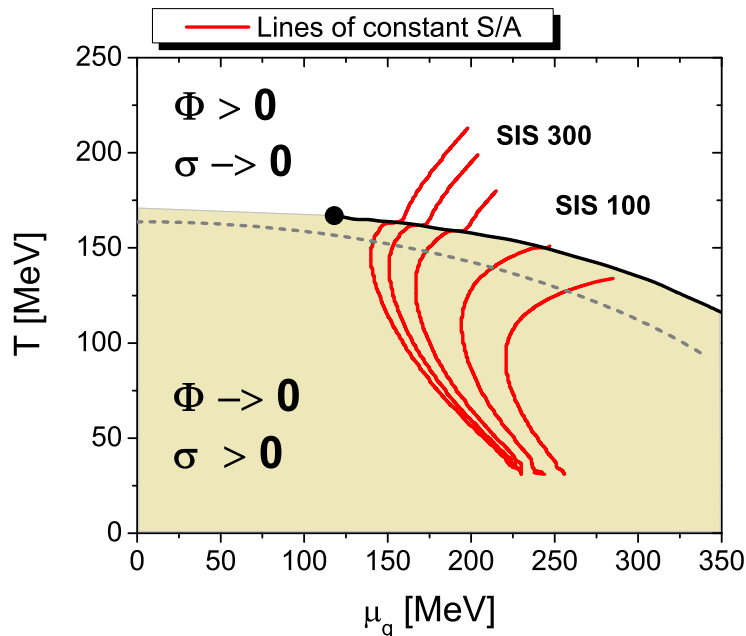


Figure 4.3: Isentropic expansion paths (red lines) in the  $T - \mu_q$  plane for very central Pb+Pb/Au+Au reactions. Isentropic expansion from the overlap model initial conditions are shown as full line in blue. Beam energies are from left to right:  $E_{\text{lab}} = 40, 30, 20, 10, 5A$  GeV. The line of the first order phase transition is indicated in black together with the critical endpoint of the model. Also shown is the line of constant energy density  $\epsilon = 4\epsilon_0$  (gray dashed).

Making the Polyakov depend explicitly on the baryon chemical potential introduces an interesting and questionable new aspect into the model. From thermodynamics we know that the derivative of the pressure with respect to the baryo chemical potential gives the net baryon number density. This means that:

$$\frac{\partial p_{\text{pol}}}{\partial \mu_B} = (3a_1\mu_B^3 + 2a_2T\mu_B^2)\Phi^2 = \rho_b^{\text{Pol}} \quad (4.31)$$

In other words the Polyakov potential which is introduced to model the pure gluonic sector now gives a contribution to the net baryon density. This contribution of course depends on the choice of the parameters, but for the parameters obtained in [134] it is of the same

order as the single quark contribution.

In addition the quark number susceptibilities, defined as the  $n$ 'th order derivatives of  $p/T^4$  with respect to  $\mu_q/T$  should now also have an additional contribution from the Polyakov potential.

#### 4.4.1 Results at zero baryochemical potential

In this section we will concentrate on the properties of the QH model, described in section (4.4), at vanishing chemical potential. Here lattice calculations suggest a crossover from the hadronic to the quark phase. Different lattice groups obtain different results for the phase transition temperature ranging from  $T_c = 160$  MeV to 200 MeV [172, 173].

For all following results we set  $T_0$ , the free parameter of the Polyakov-potential, to  $T_0 = 235$  MeV and the excluded volume parameter  $v = 1\text{fm}^3$ . This leads to a critical temperature of  $T_c \approx 183$  MeV ( $T_c$  is defined as the temperature with the largest change in the order parameters as a function of the temperature). We will also distinguish results obtained when the Polyakov loop is coupled to the dilaton in the above described manner (solid lines), and those where the dilaton is not coupled to the Polyakov loop (dashed lines).

The lattice data referred to in the following sections are taken from the HotQCD collaboration [174]. Here different actions (p4, asqtad) and lattice spacings ( $N_\tau = 6, 8$ ) were compared. Note that the transition region extracted from the lattice data lies between 185 and 195 MeV. The reader should keep in mind that different lattice groups get significantly differing results on all observables. This indicates that the systematic uncertainties on lattice data are still very large (much larger than the statistical errors which are usually plotted). In fact, recent lattice results of the HotQCD group [175] with new actions in order to improve the description of hadrons on the lattice, point to the importance of hadrons to describe the phase transition as well as explicitly state the rather slow and smooth transition from confinement to deconfinement with a wide intermediate region.

There are even attempts to combine results on thermodynamics from the lattice with those from a hadronic resonance gas which is expected to be the correct description of matter below  $T_c$  [124]. We therefore do not expect to get a good agreement of our results on thermodynamics with the lattice data below  $T_c$ .

Fig. 4.4 shows the temperature dependence for the order parameters of both, the deconfinement ( $\Phi$ ), and chiral ( $\sigma$ ) phase transition, extracted from our model and compared to lattice data. Both order parameters change smoothly with temperature. The critical temperature is found to be equal for both phase transitions. The lattice results represent a quantity which is called the subtracted chiral condensate ( $\Delta_{l,s}$ ) and which is defined in

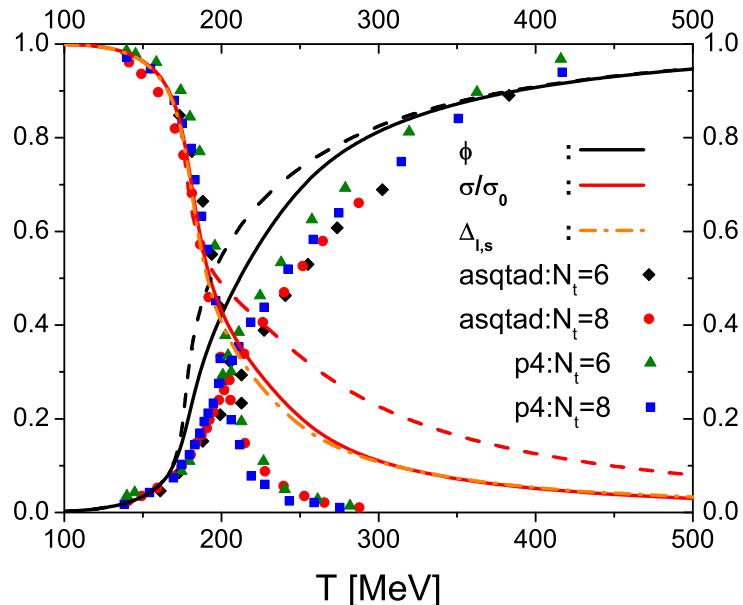


Figure 4.4: The normalized order parameters for the chiral (black, dashed line), and deconfinement (red, solid line) phase transition as a function of  $T$  at  $\mu_B = 0$ . The dashed lines depict results with the Polyakov loop-dilaton coupling described in the text. Also indicated is the subtracted chiral condensate as defined in the text (orange dotted line). The symbols denote lattice data for the subtracted chiral condensate from [174], using different lattice actions (asqtad and p4) and lattice spacings  $N_\tau$ .

the following way:

$$\Delta_{l,s}(T) = \frac{\sigma(T) - m_q/m_s \zeta(T)}{\sigma(0) - m_q/m_s \zeta(0)} \quad (4.32)$$

Here  $m_q$  and  $m_s$  refer to the bare mass of up, down and strange quarks and  $\zeta$  is the strange quark condensate.

Note that the value of the chiral condensate  $\sigma$  approaches zero only slowly. This originates from the dilaton contribution to the scalar potential in this model (the logarithmic term in eqn.(3) prevents the value of sigma to drop as fast as expected), which generates a repulsive term for small values of  $\sigma$ . Therefore the temperature dependence of the chiral condensate compares less favorably to lattice results than PNJL type models. A simple ansatz to solve this problem would be to simply remove the dilaton contribution from the model, but in the current parametrization of the hadronic model the dilaton contribution is essential for the correct description of the ground state of nuclear matter. To resolve this problem we introduced a different coupling of the dilaton to the hadrons (and quarks)

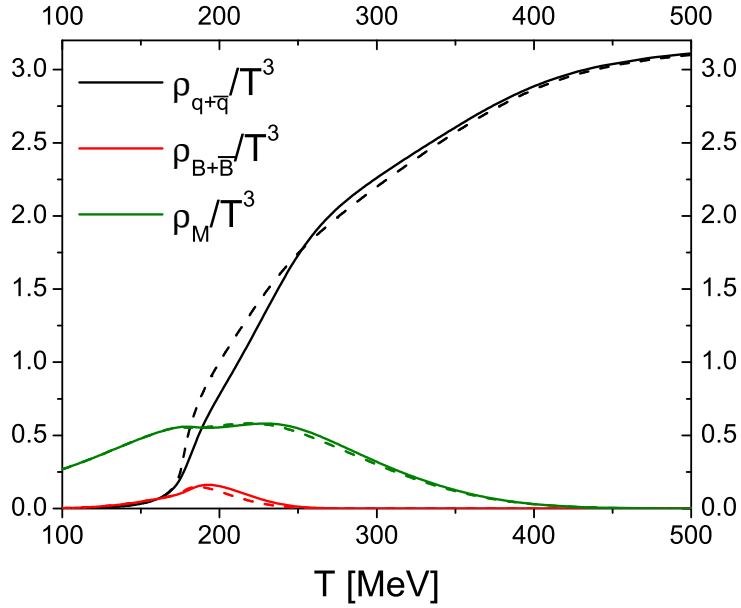


Figure 4.5: Total particle number densities for the different particle species over  $T^3$  as a function of  $T$  at  $\mu_B = 0$ . The black line shows the total number of quarks+antiquarks per volume while the green line refers to the total meson density and the red line to the number density of hadronic baryons+antibaryons. The dashed lines depict results with the Polyakov loop-dilaton coupling described in the text.

and fields (as for example outlined in [176], here part of the baryon mass is generated through coupling to the dilaton and part through coupling to the chiral condensate). In addition we coupled the dilaton to the Polyakov loop as described in section (4.4). This way we achieve a satisfactory description of nuclear ground state and a more satisfactory behavior of the chiral condensate above  $T_c$ , although the value of the chiral condensate, with dilaton coupling (solid line), does still not approach zero as fast as on the lattice.

Like in the PNJL model the parameters of the Polyakov potential are fixed by a fit to pure glue lattice data. Hence, the value of the Polyakov Loop increases somewhat faster as a function of temperature than in recent lattice calculations including quarks. The same behavior can be observed, when a PNJL type of model [157] is compared against the newest lattice results as a function of temperature (and not  $T/T_c$  which can be misleading at some point). Still, the Polyakov-dilaton coupling improves the description of the data.

Fig. 4.5 shows the total densities of quarks plus antiquarks (black lines), mesons (green lines) and baryons plus antibaryons (red lines). Below the critical temperature hadrons

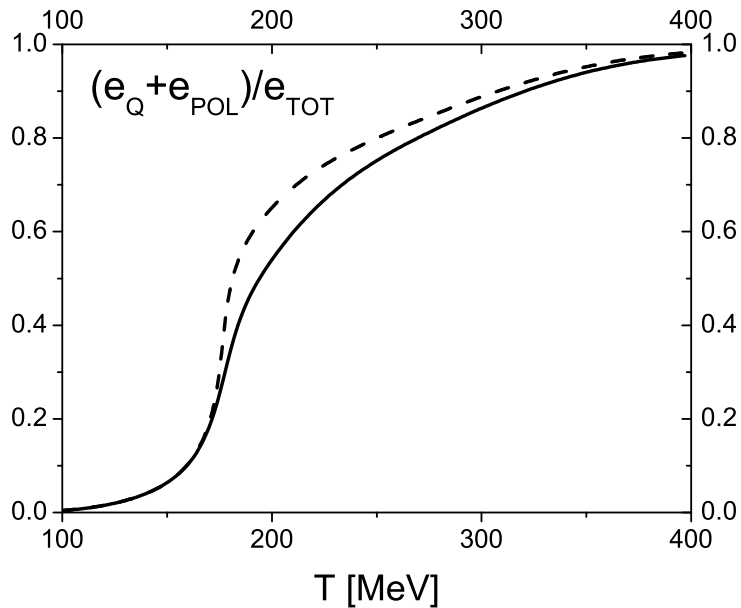


Figure 4.6: The fraction of the total energy density that can be assigned to the quark-gluon phase ( $e_{QGP}$  contains the energy of the quarks and the Polyakov potential) as a function of  $T$  at  $\mu_B = 0$ . The dashed line depicts results with the Polyakov loop-dilaton coupling described in the text.

are the dominant degree of freedom. When the quark number increases around  $T_c$ , they begin to suppress the hadrons. It is remarkable that the hadrons are still present, and not negligible, up to about  $2.0 T_c$  [177]. Especially the mesons contribute strongly to all thermodynamic quantities, since they are quite less suppressed than the baryons ( $v_M < v_B$ ) and have an essentially smaller mass.

Above  $2 T_c$  the hadrons are effectively squeezed out of the system by the presence of the quarks.

To emphasize this change in degrees of freedom, Figure (4.6) shows the fraction of the total energy density which stems from the quarks and gluons (more precisely the Polyakov potential). As expected for a crossover both degrees of freedom (hadrons and quarks) are present in the temperature range from  $0.75 - 2 T_c$ . Around  $T_c$  the fraction of the energy density, due to quarks and gluons increases rapidly. It converges to unity at around 2 times  $T_c$ .

Let us now take a closer look at different thermodynamic quantities. Figure (4.7) displays the energy density (black curve) and three times the pressure (red dashed curve), both over  $T^4$  compared to lattice data [174]. In the limit of infinite temperature, both quanti-

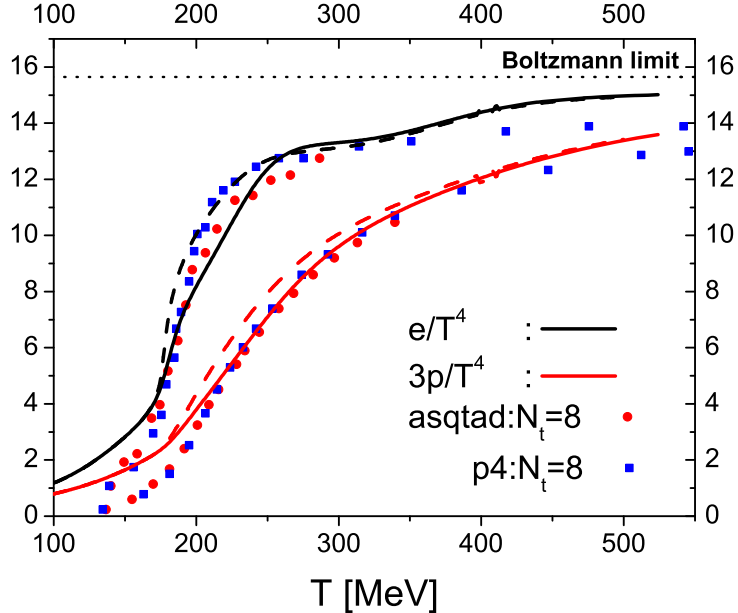


Figure 4.7: Three times the pressure (red solid line) and energy density (solid line) over  $T^4$  as a function of  $T$  at  $\mu_B = 0$ . The dashed lines depict results with the Polyakov loop-dilaton coupling described in the text. The green dotted line indicates the Boltzmann limit for an ideal gas of three massless quarks and gluons. The symbols denote lattice data from [174], using different lattice actions (asqtad and p4) and lattice spacings  $N_\tau$ .

ties should converge to the Stefan-Boltzmann limit of an ideal gas of quarks and gluons. This limit is indicated as a green dashed line. The strong increase in energy density around  $T_c$  reflects the rapid change of the relevant degrees of freedom. At three times the critical temperature the energy density is slowly converging to the Stefan-Boltzmann limit, while the pressure is converging even slower as it was also observed in PNJL calculations [138]. At temperatures below  $T_c$  our calculation gives larger values for the pressure and the energy density.

Around  $1.5 T_c$  one can observe a slight 'dip' in the energy density. This 'dip' is connected to the slow disappearance of the correction factor  $f$  of the excluded volume corrections. As has been shown above, the hadronic contribution to the densities disappears completely only at two times  $T_c$  and therefore they still exclude some portion of the volume for the quarks. The 'dip' therefore indicates the disappearance of volume correction factors for the quark phase.

In the high temperature limit, where only the quarks (and gluons) remain in the system



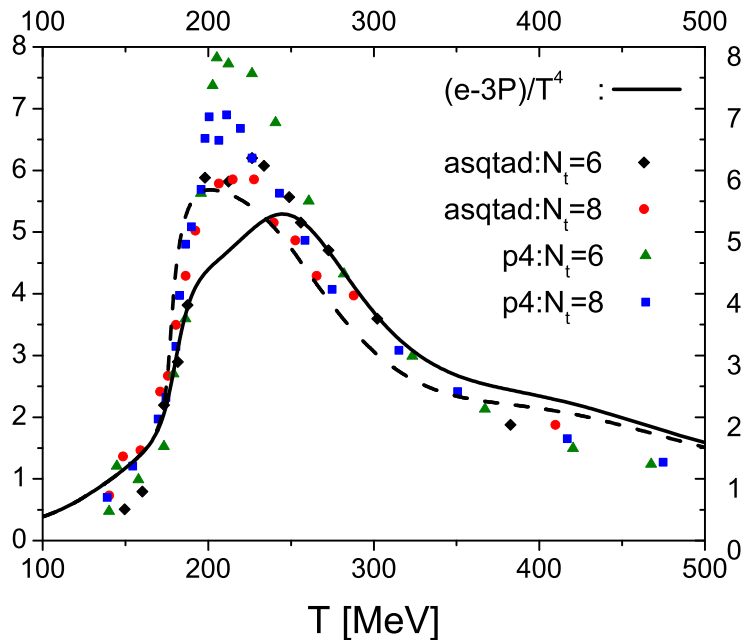


Figure 4.8: Energy density minus three times the Pressure over  $T^4$  as a function of  $T$  at  $\mu_B = 0$ . Also referred to as the interaction measure. The dashed lines depict results with the Polyakov loop-dilaton coupling described in the text. The symbols denote lattice data from [174], using different lattice actions (asqtad and p4) and lattice spacings  $N_\tau$ .

the energy density and pressure both slightly exceed the data from lattice calculations.

Figure (4.8) displays the difference of the energy density and three times the pressure over  $T^4$  (black lines). This quantity is also referred to as the 'interaction measure' in lattice calculations. In the Stefan-Boltzmann limit it is 0, while it shows a peak slightly above  $T_c$ . The height of the peak in our model is comparable to the lower bound from lattice studies [174], while its value at large  $T$  is a little bit above that from lattice calculations, because chiral restoration is not fully achieved in our model. Again we would like to stress that the agreement of the interaction measure with the lattice data is better for the case without the Polyakov-dilaton coupling, although the agreement in the order parameter is better with such a coupling. This is interesting, as it means that an agreement of both, order parameters and the interaction measure, to the lattice data seems very unlikely to achieve.

Even though our model results below  $T_c$  agree well with the lattice results for the interaction measure, the corresponding values for the energy density and pressure differ considerably,

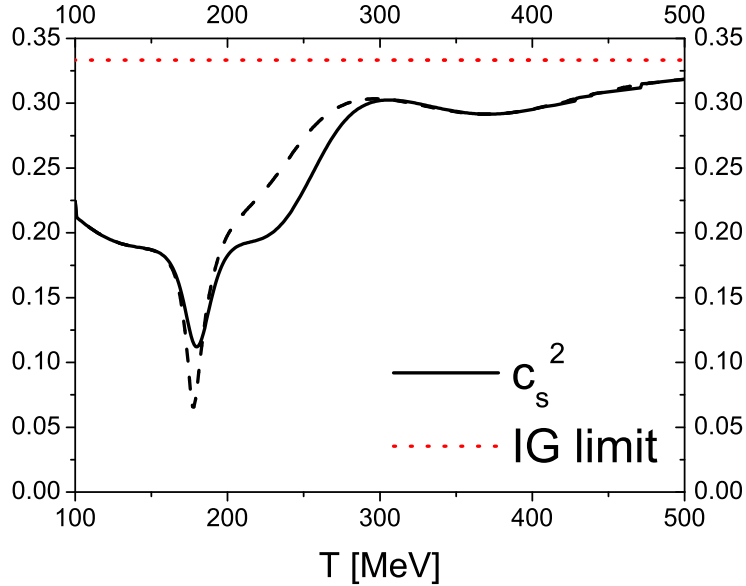


Figure 4.9: (color online) The speed of sound squared, as a function of  $T/T_c$  at  $\mu_B = 0$ .  $1/3$  is the ideal gas limit. The dashed line depicts results with the Polyakov loop-dilaton coupling described in the text.

when we compared to lattice data (Figure (4.7)). This points out that the newest lattice results still do not have the resolution to describe the hadronic part of the heat bath sufficiently well [174]. Thus, interaction effects of hadronic states in the hot system are most likely not correctly taken into account in the current lattice data. Note again that our model gives a much better description of the interaction measure as it does for the order parameters when compared to lattice. This might indicate that the conversion from the behavior of the Polyakov loop to the behavior of thermodynamic quantities might not be as proposed in a PNJL type approach.

An important property of a hot and dense nuclear medium is the speed of sound ( $c_s$ ):

$$c_s^2 = \left. \frac{dp}{de} \right|_{\mu=0} \quad (4.33)$$

It is not only closely related to expansion dynamics but also controls the way perturbations (sound- and shock-waves) travel through the fireball [97]. Figure (4.9) shows the speed of sound squared as a function of temperature. As the temperature increases towards  $T_c$  one can clearly observe a softening of the EoS due to the crossover. At very high temperature the speed of sound converges toward its ideal gas limit of  $c_s^2 \rightarrow 1/3$ . The dip above  $T_c$  is

again related to the excluded volume corrections. Note that even though the change of degrees of freedom from hadrons to quarks proceeds as a crossover, there is still a substantial softening (i.e.  $c_s^2$  goes down to 0.07). This behavior is comparable to results obtained with different versions of the PNJL model [157, 141]. It is a result of the fit of the Polyakov loop potential to pure glue data, resulting in a steeper increase of the order parameter when compared to lattice results including quarks.

Our model has essentially two free parameters,  $T_0$  and the excluded volume parameter. we checked that varying the volume parameter  $v$  by a factor of 2 does not alter the temperature dependence of the Polyakov loop as it is controlled mainly by the Polyakov potential (and therefore the parameter  $T_0$ ). Even the phase transition temperature  $T_c$  of the chiral phase transition is not affected by the volume parameter. For smaller values of the volume the chiral phase transition becomes slightly steeper (a faster increase with temperature). The thermodynamic quantities change at maximum about 10% around  $T_c$ , but the qualitative behavior of the hadrons being suppressed by the quarks stays unchanged. It is rather a question of how much the hadrons get suppressed at a given Temperature and therefore how much they still contribute in the region of phase coexistence. At some point above  $T_c$  the hadrons are removed for any value of the volume parameter.

#### 4.4.2 Results at nonzero baryochemical potential

Most of the physical observables we have accurate knowledge of are measured in the vacuum and, concerning the scales used in this work, at almost zero temperature. Important observables for our work are for example the vacuum masses of the hadrons and the properties of nuclear ground state matter. So before extending our work to the realm of finite baryon density and finite temperature we need to make sure that our model gives reasonable results at zero temperature. First we want to investigate the behavior of the different particle densities, at  $T = 0$ , as a function of net baryon density. Here the repulsive vector interaction, transmitted by the vector field  $\omega$ , starts to play a more important role than the attractive interaction originating from the  $\sigma$  field. In our model the vector interaction strength  $g_{n\omega}$  of the nucleons can easily be constrained by demanding reasonable values for the nuclear binding energy and saturation density. This is not the case for the quark vector-interaction strength. The only reasonable constraint on their part would be to demand that there are no free quarks present in the nuclear ground state.

Figure (4.10 left) shows the densities of quarks (red lines) and protons (black lines) as a function of net baryon density compared to the nucleon density from the purely hadronic model (grey dashed line). In the case of no repulsive quark vector interaction (dotted lines) the free quarks appear already before the ground state density. This would mean that there is no nuclear liquid-gas phase transition and no physical nuclear ground state. If we introduce a finite quark vector interaction strength of  $g_{q\omega} = 3.0 \approx g_{n\omega}/3$  the quarks appear only at larger densities.

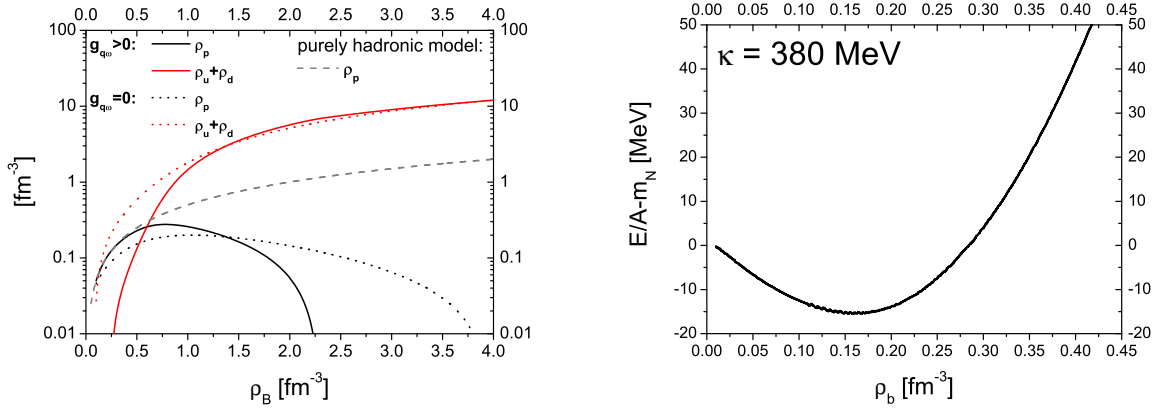


Figure 4.10: Left: Densities of the different particle species as a function of net baryon density at  $T = 0$ . The grey dashed line is the result from the purely hadronic model and serves as a baseline comparison. The red lines show the results for the quark densities while the proton densities are depicted in black. Results with a quark vector interaction strength of  $g_{q\omega} = 3.0$  are shown as solid lines while the dashed lines are results with  $g_{q\omega} = 0$ . Right: Binding energy per nucleon as a function of net baryon density at  $T = 0$  for  $g_{q\omega} = 3.0$ . The minimum is located at  $\approx 0.16 \text{ fm}^{-3}$  and the corresponding binding energy is  $E/A - m_N \approx -16 \text{ MeV}$ . The resulting incompressibility is  $\kappa \approx 380 \text{ MeV}$ .

In this scenario we can obtain reasonable values for the nuclear ground state saturation density ( $\rho_0 \approx 0.16 \text{ fm}^{-3}$ ) as well as the binding energy ( $E/A - m_N \approx -16 \text{ MeV}$ ) as can be seen in Figure (4.10 right). We can also calculate the incompressibility modulus at ground state density, defined as  $\kappa = 9(dp/d\rho_b)_{T=0, \rho_b=\rho_0}$  and obtain a result of  $\kappa \approx 380 \text{ MeV}$ . This value is somewhat larger as expected [178] and is due to the hard core repulsive interactions which make the system rather incompressible. We have checked that in fact the speed of sound does stay below  $c_s = 1$  for any density or temperature.

Since our model does not sustain the difficulties that lattice calculations have, when going to finite densities, we can simply extend our investigations to finite chemical potentials ( $\mu_B = 3\mu_q \neq 0$ ) and temperature. As for the case at  $T = 0$  any repulsive vector interaction for the quarks may change the picture of the phase diagram. The value of the repulsive interaction strength  $g_{q\omega}$  is not constraint by any first principle calculation. It could even be a function of temperature and density. For simplicity we will compare two cases,  $g_{q\omega} = 0$  and  $g_{q\omega} = 3$ , to show the qualitative changes of the phase diagram when different values of the vector coupling strength are assumed.

For calculations at finite  $\mu_B$ , the strange quark chemical potential  $\mu_s$  also plays an important role. If one assumes, that the total net strangeness is globally conserved, hadronic

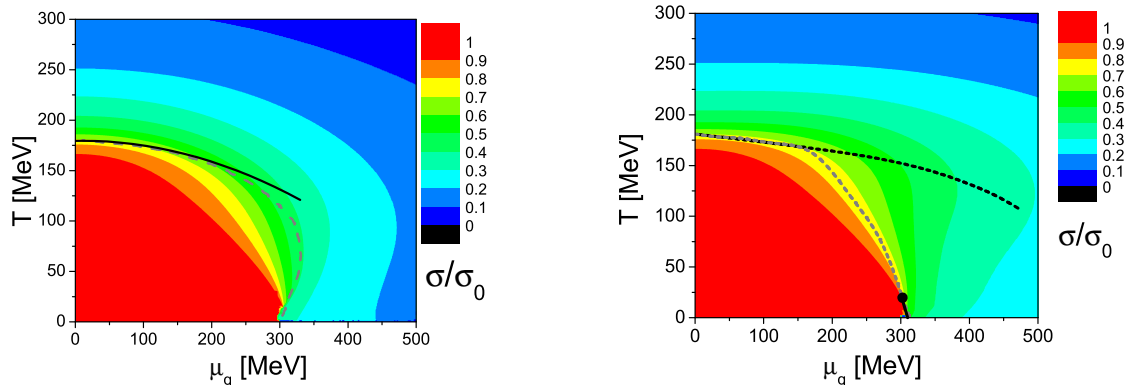


Figure 4.11: Contour plot of the normalized chiral condensate  $\sigma/\sigma_0$  as a function of temperature and quark chemical potential. The black solid line, starting at  $T = 0$  and  $\mu_q = 316\text{MeV}$  shows the liquid-gas phase transition. The dashed grey line depicts the continuation of the liquid gas transition, which becomes a crossover at  $T \approx 16\text{MeV}$ . The black dashed line corresponds to the deconfinement crossover, which falls together with a very smooth second chiral crossover.

Left: results with quark vector coupling  $g_{q\omega} = 3.0$

Right: results with quark vector coupling  $g_{q\omega} = 0.0$

chemistry induces a non zero chemical potential for the strange quark, while it vanishes for the case of a free quark gas (note that we use the strange quark chemical potential  $\mu_s$ , not the chemical potential of the strange charge  $\mu_S = \mu_q - \mu_s$ ). In the present work we always constrain the net strangeness to be zero, but one should also investigate the phase structure of a system where this is not fulfilled. Work along this line is in progress.

Figure (4.11) displays contour plots of the chiral condensate  $\sigma$  (normalized to its ground state value  $\sigma_0$ ) in the  $T - \mu_q$  phase diagram for the two values of the repulsive quark interaction strength. It is apparent to see that in both cases the chiral phase transition is a smooth crossover for all chemical potentials. Only at very low temperatures the iso- $\sigma$  lines converge a first order phase transition. In the case of  $g_{q\omega=3}$  this can be identified with the nuclear liquid-gas phase transition, which is first order at zero temperature (displayed in the plot as the solid black line with a critical endpoint at  $T_c \approx 16\text{MeV}$ ). As mentioned above, if the repulse vector interaction strength of the quarks is smaller, they already appear at or before the nuclear ground state and cause the first order jump in the order parameter. At high temperature and high chemical potentials the lines of constant  $\sigma$  are even farther apart than a vanishing net baryon density, indicating an even smoother crossover than at  $\mu_q = 0$ . We can still calculate the derivative of the order parameter with respect to the temperature and chemical potential. The grey dashed lines where this gradient has his maximum in the phase diagram. The black dashed lines indicate a second, very

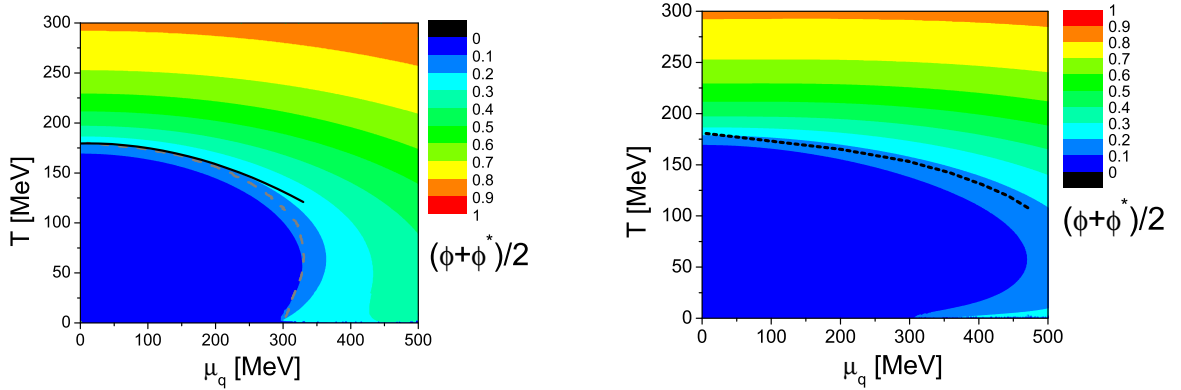


Figure 4.12: Contour plot of the average Polyakov loop  $\frac{\phi+\phi^*}{2}$ , order parameter of the deconfinement phase transition, as a function of temperature and quark chemical potential. The black dashed line corresponds to the deconfinement crossover.

Left: results with quark vector coupling  $g_{g\omega} = 3.0$

Right: results with quark vector coupling  $g_{g\omega} = 0.0$

small maximum in this derivative, which is caused by a rapid change in the deconfinement order parameter, the Polyakov loop. This indicates that the largest change in the chiral condensate is governed by hadronic interactions and not by the appearance of the quarks.

The observation of a smooth crossover can also be found in the contour plot of the Polyakov loop as a function of  $T$  and  $\mu_q$ , in Figure (4.12). Here again results for two different values of the repulsive vector interaction are shown. The black dashed lines are indicating the maximum of the derivative of the Polyakov loop with respect to temperature and chemical potential. There is a visible difference in the chiral (grey dashed) and deconfinement (black dashed) phase transitions at high chemical potentials. While the chiral condensate already drops at the liquid gas phase transition  $\mu_q \approx 313$  MeV, the Polyakov loop remains small until much higher chemical potentials.

This behavior is very interesting as it means that, in some parts of the phase diagram, chiral symmetry is partially restored while quarks are still confined. This can be made more clear if one looks at the fraction of the total energy density which can be contributed to quarks and gluons (more precisely quarks and the Polyakov potential). This fraction ( $e_{\text{QGP}}/e_{\text{TOT}}$ ) is plotted in Fig. (4.13), using  $g_{g\omega} = 3$ , in the phase diagram where we again indicated the largest change in the chiral condensate (grey dashed line) and the Polyakov loop (black dashed line). Again one observes, at high chemical potentials and intermediate temperatures, a phase which consists only partly of quarks and hadrons, while chiral symmetry is partially restored.

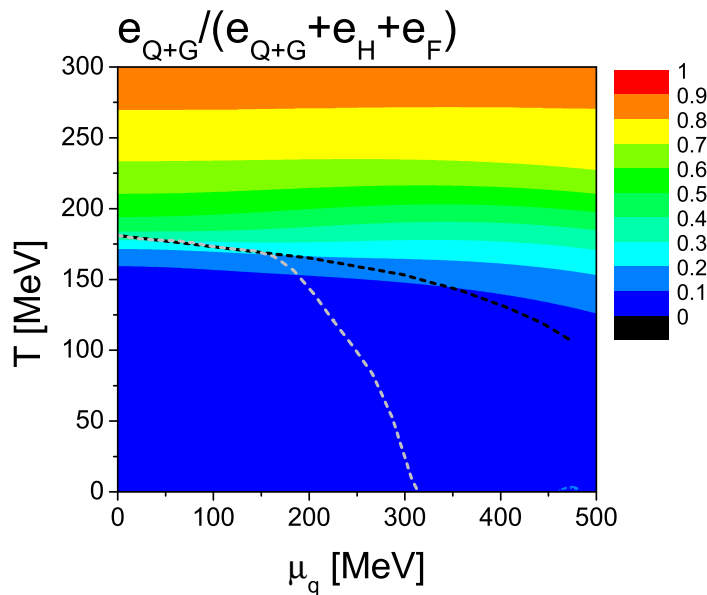


Figure 4.13: Contour plot of the fraction of the total energy density which comes from the quark contribution and the Polyakov loop potential. The value for the quark repulsive interaction is  $g_{q\omega} = 3$ . The dashed grey line indicates where the change of the chiral condensate with respect to  $T$  and  $\mu_q$  has a maximum while the solid black line shows the same for the change of the Polyakov loop.

### 4.4.3 Susceptibilities

Lattice results at finite chemical potentials are often obtained as Taylor expansion of the thermodynamic quantities in the parameter  $\mu/T$  around zero chemical potential [112]. In the Taylor expansion of the pressure  $p = -\Omega$ , the coefficients, which can be identified with the quark number susceptibilities, follow from:

$$\frac{p(T, \mu_B)}{T^4} = \sum_{n=0}^{\infty} c_n(T) \left(\frac{\mu_B}{T}\right)^n \quad (4.34)$$

$$c_n(T) = \frac{1}{n!} \left. \frac{\partial^n (p(T, \mu_B)/T^4)}{\partial (\mu_B/T)^n} \right|_{\mu_B=0} \quad (4.35)$$

In our approach we explicitly calculate the pressure at finite  $\mu_B$  and then extract the expansion coefficients numerically. The results for the second coefficient calculated for the PNJL model and QHM model, compared to lattice results [179], are shown in figures (4.14) and (4.15). One can clearly observe that the best description can be obtained when quark vector interactions are turned off. Any form of repulsive interaction strongly decreases the value of the second order coefficient above  $T_c$ . The lattice results on the other hand quickly

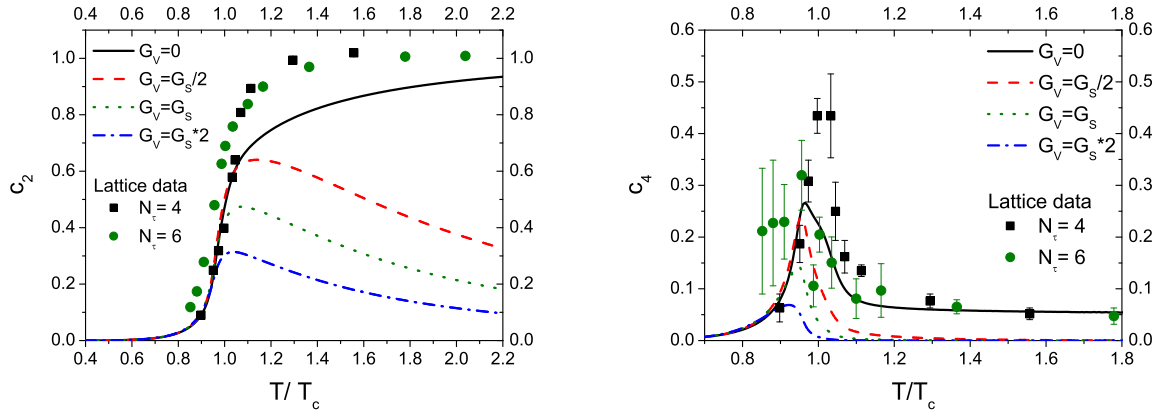


Figure 4.14: Left: The second order quark number susceptibility from the PNJL model, with different strengths of the vector interaction, as a function of  $T$  over  $T_c$ . Black solid line: no vector interaction, red dashed line:  $G_V = G_S/2$ , green dotted line:  $G_V = G_S$ , blue dash dotted line  $G_V = 2G_S$ .

Right: The fourth order quark number susceptibility from the PNJL model, with different strengths of the vector interaction, as a function of  $T$  over  $T_c$ . Black solid line: no vector interaction, red dashed line:  $G_V = G_S/2$ , green dotted line:  $G_V = G_S$ , blue dash dotted line:  $G_V = 2G_S$ .

reach a value that is expected for a non-interacting gas of quarks, even right above  $T_c$ . This is in fact surprising as other thermodynamic quantities tend to favor a picture with a wide region around  $T_c$  where interactions are strong. This behavior was also reproduced by the PNJL model and the QH model while both fail to describe the fast increase in  $c_2$  right above  $T_c$ .

In this context it is noteworthy that the introduction of terms  $\propto T^2 \mu_q^2$  in the Polyakov potential (see for example section (4.4)) will give a contribution to the 2nd order coefficient. As  $c_2$  goes to unity immediately above  $T_c$  in the lattice data, this makes such a  $\mu_q$  dependence of the Polyakov loop seem very unlikely.

Next we try to disentangle the hadronic contribution to the second coefficient. As can be seen in Fig. 4.15 the dependence on the strength of the repulsive interaction below  $T_c$  is rather small and one can not exclude any scenario. In the crossover region, around  $T_c$ , differences become obvious.

The solid black line in Figure (4.15) displays the result for  $c_2$  using the standard parametrization of the QH model as described in (4.4) without any repulsive quark-quark interactions. The value of  $c_2$  only slowly approaches 1, which is mainly due to the fact that the value of the chiral condensate drops to 0 rather slow in our model and therefore the quark masses do not decrease as fast as in the PNJL approach.



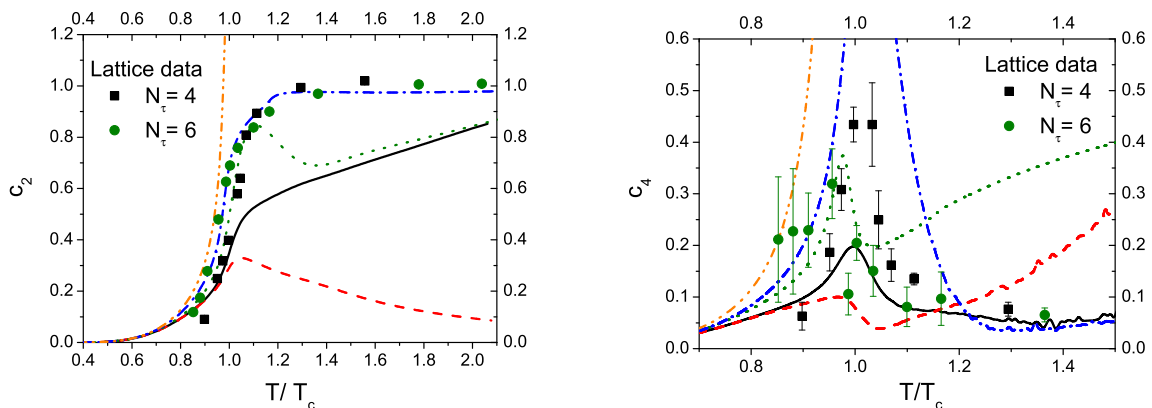


Figure 4.15: Left: The second order quark number susceptibility from the QH model, with different strengths of the vector interaction, as a function of  $T$  over  $T_c$ . Black solid line:  $g_{N\omega} \neq 0, g_{q\omega} = 0, v = 1$ , red dashed line:  $g_{N\omega} \neq 0, g_{q\omega} = g_{N\omega}/3, v = 1$ , green dotted line:  $g_{N\omega} = 0, g_{q\omega} = 0, v = 1$ , blue dashed dotted line:  $g_{N\omega} \neq 0, g_{q\omega} = 0, v = 0$ , orange dash dot dot line:  $g_{N\omega} = 0, g_{q\omega} = 0, v = 0$ .

Right: The fourth order quark number susceptibility from the QH model, with different strengths of the vector interaction, as a function of  $T$  over  $T_c$ . Black solid line:  $g_{N\omega} \neq 0, g_{q\omega} = 0, v = 1$ , red dashed line:  $g_{N\omega} \neq 0, g_{q\omega} = g_{N\omega}/3, v = 1$ , green dotted line:  $g_{N\omega} = 0, g_{q\omega} = 0, v = 1$ , blue dashed dotted line:  $g_{N\omega} \neq 0, g_{q\omega} = 0, v = 0$ , orange dash dot dot line:  $g_{N\omega} = 0, g_{q\omega} = 0, v = 0$ .

Including repulsive vector interactions for the quarks gives a result which is similar to the one obtained from the PNJL (red dashed line). Here the repulsive interactions strongly decrease the value of  $c_2$ .

Turning off all repulsive interactions, vector interactions for quarks and hadrons as well as the excluded volume corrections (orange dash dot dotted line), leads to a drastic overestimation of  $c_2$ . This is expected as all hadronic degrees of freedom are present at and above  $T_c$  if the excluded volume effects are turned off. Therefore one largely overestimates the effective degrees of freedom.

On the other hand if the repulsive vector interactions are turned on only for the hadrons one obtains a rather good description of the lattice results (blue dash dotted line). In this parametrization the hadrons are also still present in the system up to arbitrary high temperatures, as the excluded volume effects are still turned off, and therefore all thermodynamic quantities are largely over predicted.

To remove the hadronic contributions from the system we introduced excluded volume cor-

rections as described above. This leads to a pronounced dip in  $c_2$  above  $T_c$  (green dotted line), indicating that our excluded volume approach is either too simplified or all hadronic contributions are already vanishing completely right above  $T_c$  or that the lattice results are still not accurate enough to sufficiently resolve effects of hadron-hadron interactions.

The fourth order coefficients calculated for the PNJL and QH model are shown on the right side of figures (4.14) and (4.15). Although the errors on the lattice results are still significant our results for  $c_4$  support the statements made for  $c_2$ . At temperatures above  $T_c$  a gas of free non-interacting quarks, without any hadronic contribution, gives the only reasonable description of the data already slightly above  $T_c$ . While the height of the peak does depend on the strength of the vector coupling, we observe also a strong dependence on the slope of the change of the order parameters around  $T_c$ , which is larger in the QH model as compared to the PNJL model. Notice that the parametrization shown as the blue dash-dotted line, which gave the best description for  $c_2$ , overestimates  $c_4$  around  $T_c$  drastically. This is simply because all thermodynamic quantities are over-predicted in this case and therefore the densities as well as the order parameters increase steeper as they do in the lattice calculations.

#### 4.4.4 Distillation

Until now we have restricted ourselves to calculations at vanishing net strangeness. As strangeness is conserved under the strong interaction this seems reasonable when describing heavy ion collisions where the strong interaction is the most important force. Nevertheless there are possible mechanisms which may separate the strange from the anti-strange particles in a heavy ion collision, either dynamically or chemically. In the following we will discuss a possible scenario for a chemical separation which could occur if one has a phase coexistence of quarks and hadrons, which was called a strangeness distillation.

First we need to estimate for which values of net strangeness per baryon we could expect to see interesting signatures, like stable or metastable clusters of strange matter.

Calculations within our hadronic effective chiral mean field model [131, 132] (see chapter 4.2) predict that stable and metastable strange matter can be created when the net strangeness of the bulk matter becomes larger than  $f_s > 0.4$ . In this simple estimate we set the strength of the hyperon coupling to the strange scalar field  $\zeta$  to a value of  $n_s g_2$  ( $n_s$  is the number of strange quarks in the hyperon), rescaling the other couplings to keep the correct vacuum masses of the particles. The full line in Fig. 4.16 shows the corresponding values of lowest energy of a system of free nucleons and hyperons for a given  $f_s$  (net strangeness per baryon). Beyond a value of  $g_2 \approx 2$  one obtains a bound state for fixed  $f_s$ . For even higher values of the coupling strength absolutely stable hypermatter at  $f_2 \approx 1.2$  is obtained.

In the following we will shortly discuss how such values for  $f_s$  can be produced in experiment. It was shown that strangeness can be separated in phase space within a hadronic

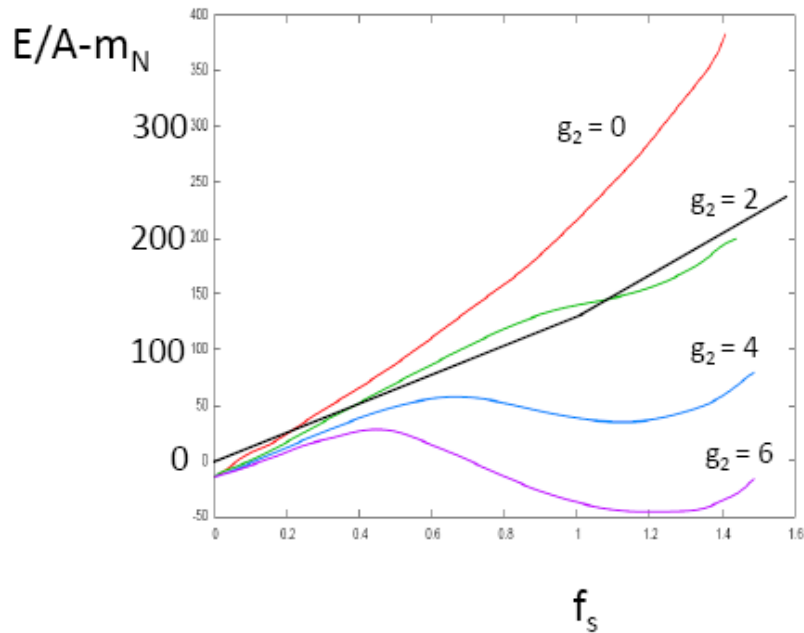


Figure 4.16: Binding energy per particle as a function of strangeness per baryon for different values of the hyperon interaction with the scalar field  $\zeta$  ( $g_2$ ).

transport model (UrQMD) [180]. This separation is a result of the non equilibrium nature of the early phase of a heavy ion collision.

Furthermore, in equilibrated fireballs, strangeness can be separated by a distillation process [181]. In addition the emission of Kaons can further enrich the produced fireball with strangeness [182]. In the following we will give an estimate on the distillation process which would occur in HIC. For our calculations we apply our QH equation of state that had been described in chapter (4.4). The model has a wide region of phase coexistence in the phase diagram, which gives room for a possible distillation scenario.

For the time evolution of the baryon density of the fireball we assume a simple Björken expansion where:

$$\rho_b(t) = \rho_0 \frac{t_0}{t} \quad (4.36)$$

with  $t_0$  being the starting time of the evolution (in our case  $t_0 = 5\text{fm}$ ). The initial density,  $\rho_0$ , follows from a geometric overlap model which gives

$$\rho_0 = 2 \gamma_{c.m.} 0.16\text{fm}^{-1} \quad (4.37)$$

$$\epsilon_0 = 2 m_N 0.16\text{fm}^{-1} \gamma_{c.m.}^2 \quad (4.38)$$

with  $\gamma_{c.m.} = \sqrt{E_{Lab}/A/2m_N + 1}$ .

Figure (4.16 right) shows the time evolution of the strangeness per baryon fraction for a fireball that is created at a Pb+Pb collision at  $E_{lab} = 40A$  GeV. The two vertical lines set the limits to where one would expect a chemical freeze out to occur. Beyond this time, the system decouples and should not be treated as being in chemical equilibrium. The solid lines depict the strangeness fraction in the different phases, while the fireball has no net strange charge. This reflects the original strangeness distillation process as proposed in [181]. In our model this process will lead to a strangeness fraction of  $f_s \approx 0.2$  of the remaining quark droplet, at freeze out.

As has been proposed in [182] the strangeness fraction can even increase more during the course of the fireballs evolution due to emission of Kaons, as anti-Kaons are more abundant at high baryon densities than Kaons. The fireball itself therefore becomes loaded with net strangeness. As proposed in [182] we assume that the emission of kaons and pions (changing the entropy per baryon ratio  $S/A$ ) can be described by the following emission equations:

$$\frac{d(S/A)}{dt} = -\frac{1}{N_B} 4\pi \left( \frac{3}{4\pi} \frac{N_B}{\rho_B} \right)^{2/3} 4\rho_\pi \quad (4.39)$$

$$\frac{df_s}{dt} = -\frac{1}{N_B} 4\pi \left( \frac{3}{4\pi} \frac{N_B}{\rho_B} \right)^{2/3} 4(\rho_K - \rho_{\bar{K}}) \quad (4.40)$$

Here,  $N_B$  is the total baryon number of the fireball and  $\rho_i$  are the densities of the corresponding particle species (baryons, pions and kaons). In combination with the distillation process, the quark part of the system can obtain a strangeness fraction of up to  $f_s \approx 0.5$ . This could in turn result in the formation of a (meta-)stable cluster of quarks or hadrons.

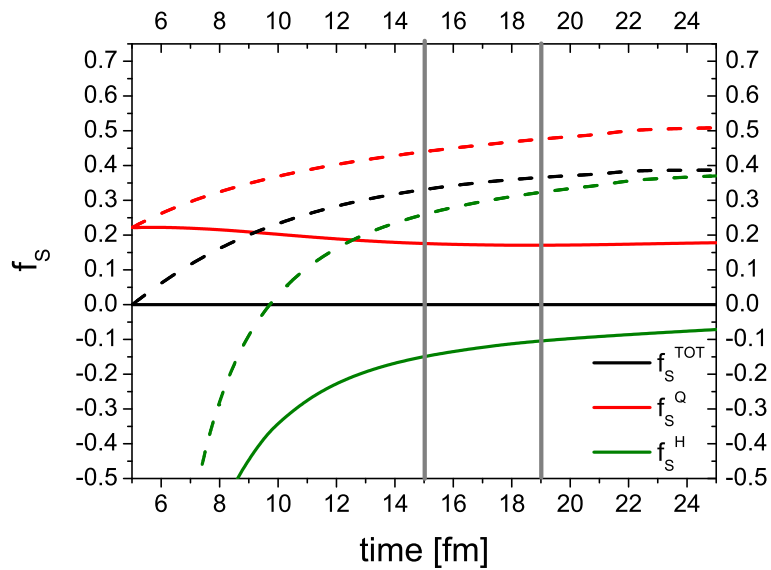


Figure 4.17: Time evolution of the strangeness per baryon fraction for the 2 coexisting phases (hadrons or quarks) in a heavy ion collision at  $E_{lab} = 40A$  GeV. The solid line corresponds to results where the fireball has vanishing net strangeness while the dashed line shows results where emission of Kaons is included.



# Chapter 5

## Results

In this chapter we will discuss the results that were obtained using the above described hybrid model to heavy ion collisions. We will discuss model parameter dependencies on bulk observables and, more importantly, the dependence on the equation of state. In the second part we will discuss model calculations on the production of hypernuclei. This is not necessarily related to the equation of state, but an interesting topic nevertheless.

### 5.1 Investigating bulk matter properties

Bulk matter properties have a long time been the center of attention when looking for a signature for the deconfinement phase transition. Starting at particle ratios and multiplicities where for example the peak structure in the excitation function of the  $K^+/\pi^+$  ratio was sought to be a signal for the quark gluon plasma [183, 52] the attention is also on different flow observables.

Such an observable would be for example the average transverse momentum of different particle species produced. As the expansion dynamics are controlled by the EoS surely the average momentum should be sensitive on the equation of state. If a first order phase transition occurs, this is usually seen in a softening of the EoS and therefore a slower overall expansion.

A more detailed study can be done when examining not only the average momentum but also different moments of a multipole expansion of the average momentum. The first moment, the so called 'directed flow'  $v_1 = \langle p_x/p_T \rangle|_y$  is zero at mid-rapidity due to momentum conservation, but could very well depend on the equation of state a finite values of  $y$ .

The second order momentum anisotropy, the 'elliptic flow'  $v_2 = \langle p_x - p_y \rangle/p_T$  is defined with respect to the two transverse directions. In non-central heavy ion collisions this is of great interest as the initial shape of the fireball is not symmetric in the transverse plane but rather has an almond like shape. This means that the initial pressure gradients

in the x-direction are different from those in the y-direction. This spacial anisotropy is then transformed in a momentum anisotropy which can be measured. The magnitude of the anisotropy depends on the pressure gradients at work and therefore directly on the equation of state. In the following we will discuss how the results, from our hybrid model, on these different observables depend on the parameters of the model as well as the equation of state that is used.

### 5.1.1 Strangeness ratios with the HRG

At CERN-SPS energies evidence for the creation of this new state of matter is claimed, e.g., with observations of an enhanced  $K/\pi$  ratio ('horn') and the step in the mean transverse mass excitation function for various hadron species. Especially the low energy (high  $\mu_B$ ) program at SPS showed a culmination of exciting results. Therefore, the production of hadrons containing strange quarks is a very interesting topic to study in this energy regime (at the FAIR facility and at critRHIC), as they have to be newly created and their production mechanism is different comparing for example the QGP to a hadron gas. Whether a QGP phase is necessary to reproduce the experimentally measured yields, is not yet clear [184, 185, 186, 187, 188].

Models that describe observed particle yields simply from a thermal heat bath, including canonical corrections for strangeness, have become quite popular recently [189, 190, 193]. These models usually rely on two parameters per beam energy, the temperature and baryo-chemical potential at which the chemical freeze out of the hadronic system occurs. Although successful in describing the data such models do not offer any explanation to whether why the hadronic system is in thermal and chemical equilibrium nor why all particles should freeze out at the same temperature.

Using our hybrid model for particle production we also assume that the system is in local thermal equilibrium throughout the whole evolution, not trying to explain why and how this occurs. In this sense it is not superior to any thermal model for particle production. On the other hand, in the case of the chemical decoupling, our model does not assume any fixed temperature, but a region in temperature in which the system undergoes a change from an equilibrated system to a system out of equilibrium. The hybrid model describes both these phases with the appropriate scheme (either fluid dynamics or transport theory) and therefore gives an alternative view on the final process of particle production.

First we compare particle ratios from the two frameworks i.e., the pure transport calculation (grey line) and the hybrid approach using a HRG equation of state (black line). In figure (5.1) the excitation functions of different particle ratios (at mid-rapidity), including strange baryons, are shown for central Au+Au/Pb+Pb collisions for center of mass energies of  $\sqrt{s} = 2 - 200$  AGeV. We also compare two different freeze-out criteria;  $4 \epsilon_0$  (solid line) and  $5 \epsilon_0$  (dashed line).

Within the hybrid model calculation the production of strange particles is enhanced, due



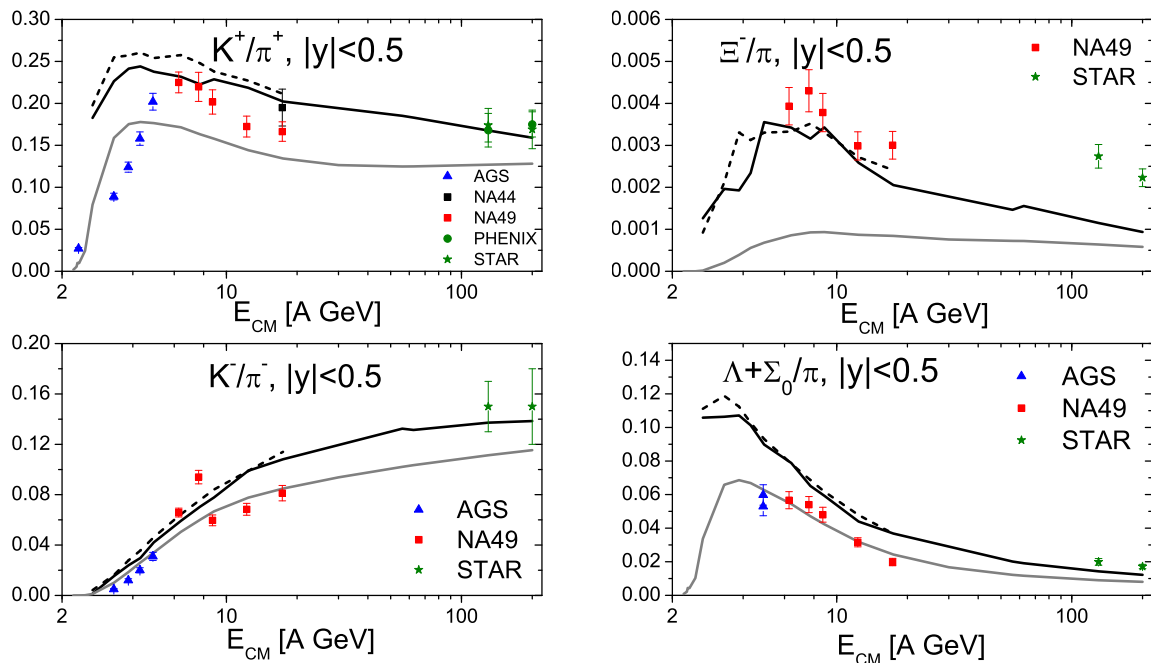


Figure 5.1: Excitation functions for kaon to pion ratios (left) and strange baryon to pion ratios (right) from most central heavy ion collisions at energies of  $E_{c.m.} = 2 - 200$  AGeV. Compared are two hybrid model calculations (black lines), UrQMD 2.3 (grey lines) and results from experiments [194, 183, 195, 196, 197, 198, 37, 199]. The two black lines represent results for different freeze out criteria  $4 \epsilon_0$  (solid line) and  $5 \epsilon_0$  (dashed line).

to the establishment of local thermal equilibrium. This leads to an improved description of multi-strange particle ratios at energies above  $\sqrt{s} \approx 5$  AGeV, while at lower energies the non-equilibrium approach seems to provide a better description of the data. Especially the 'horn' structure in the  $K^+/\pi^+$  ratio is reproduced without the explicit inclusion of a phase transition. As in thermal model studies we contribute it to a transition from a baryon dominated to a meson dominated regime in the phase diagram, reached at SPS energies. Note that the transport model is not able to reproduce the 'horn' structure in the  $K^+$  to  $\pi^+$  ratio. This was explained by an over-estimation of the pion yields rather than the actual  $K^+$  production rate [200].

### 5.1.2 Freezeout dependence

To be able to compare results applying different equations of state we first have to get a handle on the freeze out dependence of our results. The freeze out is still one of the open questions in modeling off heavy ion collisions. In our approach it is taken care of dynamically within the UrQMD approach. Still we have to define a transition density at which we

change from the fluid dynamical to the transport picture. This switching criterion, also referred to as the freeze out density, can be treated as a free parameter. Furthermore we have introduced two different prescriptions for the freeze out, the isochronous (IF) and gradual freeze out (GF). In this Section we address the  $4\pi$  multiplicity (Figs. 5.2-5.3, upper plots) and the mean transverse mass (Figures 5.2-5.3, lower plots) excitation functions for pions, protons and kaons calculated in the hybrid approach with a hadronic EoS to compare different transition prescriptions. The dotted line corresponds to the results directly after the isochronous hydrodynamic freeze-out without final state interactions (FSI). Immediate decay of the resonances is taken into account to provide comparable multiplicity results. All other calculations include the hadronic afterburner, however with different transition prescriptions applied: the isochronous freeze-out (dashed line with circles), the gradual freeze-out (full line with squares) and the gradual freeze-out with varied freeze-out energy density criterion  $4\epsilon_0$  (dashed-dotted line with triangles).

The results are calculated for central Au+Au/Pb+Pb collisions at midrapidity ( $|y| < 0.5$ ) from  $E_{\text{lab}} = 2-160A$  GeV. In general, one observes that the mean transverse mass increases as a function of energy, because more energy becomes available that can be distributed in the transverse plane and the expansion phase lasts longer.

Let us start the detailed discussion with the pions as being the most abundant hadrons. The pion multiplicity (Figure 5.2, left) is completely insensitive to the freeze-out procedure while the mean transverse mass at higher energies is decreased if the gradual freeze-out procedure is applied. The final state interactions and the variation of the freeze-out criterion do only weakly alter the results for pions. At AGS energies, the calculations are well in line with the data while at SPS energies where the hydrodynamic stage is a major part of the evolution the pion multiplicity stays below the data and the mean transverse mass exceeds the experimental data. We attribute these observations to the entropy conservation in the hydrodynamic evolution and the violent transverse expansion because of high pressure gradients.

Next, we explore the production and expansion of the baryon charge. In contrast to the previous case, the proton multiplicity (Figure 5.2, right) is almost constant over the whole energy range. The final rescatterings lead in this case to a slightly higher multiplicity and an increased mean transverse mass. The protons acquire more transverse flow during the hadronic stage after the hydrodynamic evolution. As already observed for the pions the gradual freeze-out leads to a flattening of the transverse mass excitation function. Varying the energy density criterion (squares vs triangles) indicates only a weak dependence on this parameter.

Finally, we address strange particles. Figure 5.3 shows the results for positively and negatively charged kaons respectively. The kaon multiplicities are nicely reproduced, if the isochronous freeze-out procedure is applied with or without final state interactions. The mean transverse mass in the same calculation is too high at top SPS energies due to the

violent transverse expansion because of the comparably stiff hadronic EoS. For  $K^-$  the final rescatterings lead to an increase in the mean transverse mass because the low  $p_T$   $K^-$  are easily absorbed on the surrounding baryons. In the gradual freeze-out scenario the kaon production is enhanced by roughly 10% due to the higher average temperatures at the transition point from hydrodynamics to the transport description at higher energies. For the kaon multiplicity the variation of the freeze-out criterion leads to a slight decrease of the yields when going from the gradual to the isochronous scenario. This reflects the sensitivity of the kaon yield to the temperature at the transition point between hydrodynamics and the final state hadron cascade. The mean transverse mass excitation functions are flatter with the gradual freeze-out scenario which leads to a better description of the experimental data.

Overall, the hybrid calculation with the gradual freeze-out procedure reproduces the multiplicities and the shape of the mean transverse mass excitation function best, in many cases there is even good quantitative agreement with the experimental data.

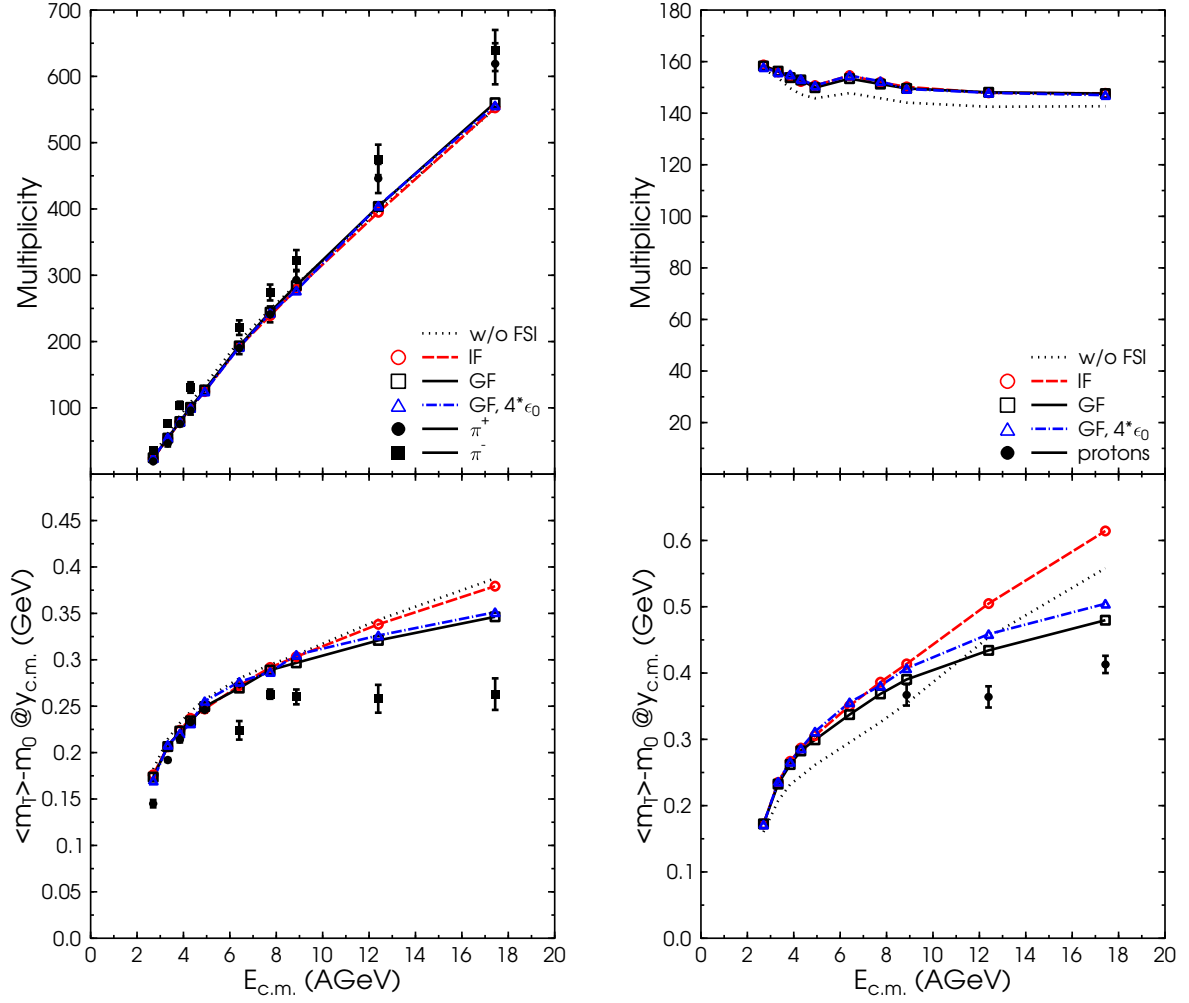


Figure 5.2: The multiplicity ( $4\pi$ , top) and the  $\langle m_T \rangle$  (bottom) excitation function for pions (left) and protons (right) in central ( $b < 3.4$  fm) Au+Au/Pb+Pb collisions at  $E_{\text{lab}} = 2 - 160$  AGeV is shown. The lines depict different freeze-out prescriptions for the hybrid model calculation with the hadron gas equation of state, while the symbols depict experimental data [37, 183, 195, 201].

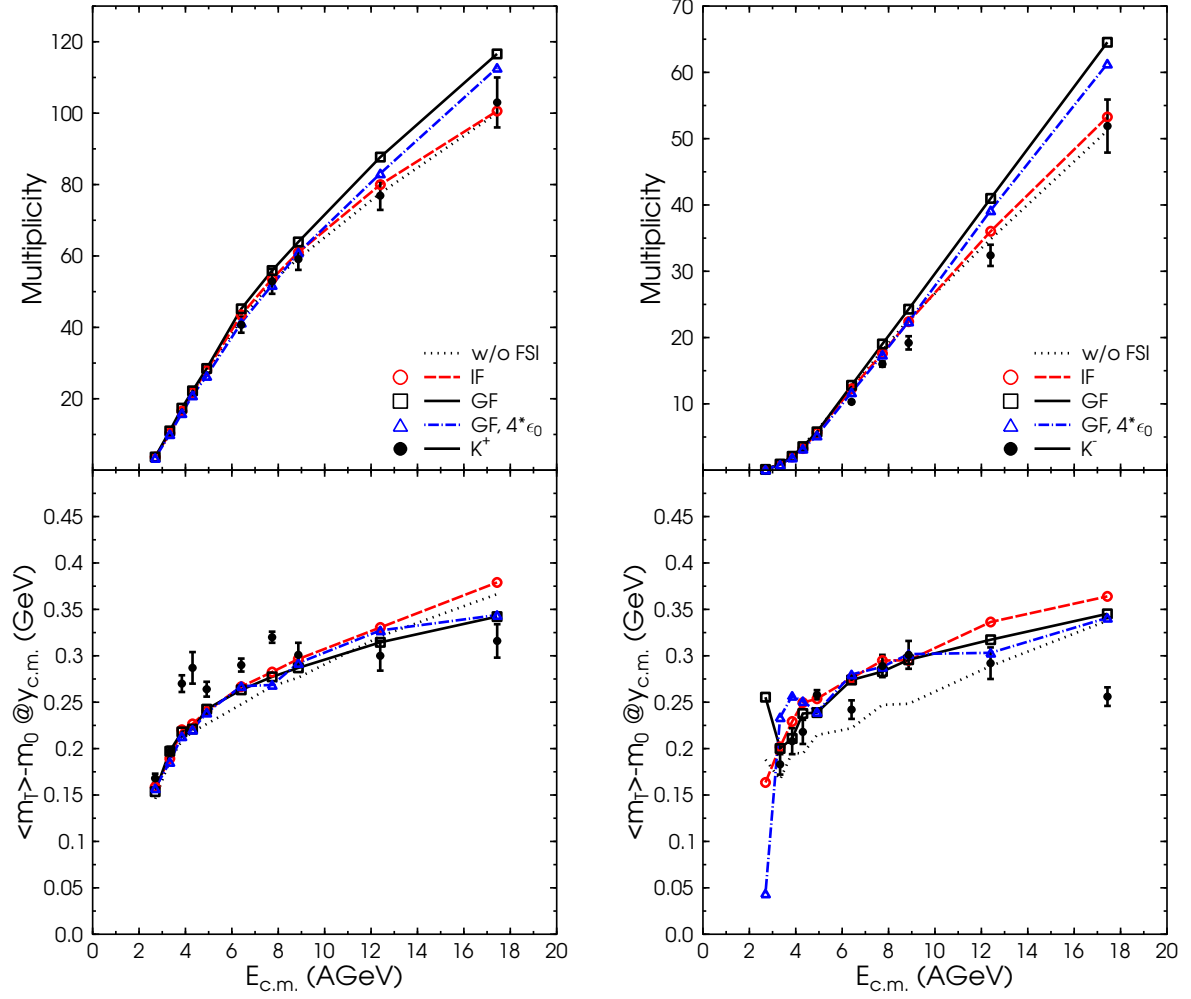


Figure 5.3: The multiplicity ( $4\pi$ , top) and the  $\langle m_T \rangle$  (bottom) excitation function for positively/negatively (left/right) charged kaons in central ( $b < 3.4$  fm) Au+Au/Pb+Pb collisions at  $E_{\text{lab}} = 2 - 160$  AGeV is shown. The lines depict different freeze-out prescriptions for the hybrid model calculation with the hadron gas equation of state, while the symbols depict experimental data [37, 183, 195, 30].

### 5.1.3 The speed of sound

An important property of a hot and dense nuclear medium is the speed of sound ( $c_s$ ):

$$c_s^2 = \left. \frac{dp}{d\epsilon} \right|_{S/A} = \left. \frac{dp}{de} \right|_n + \frac{n}{\epsilon + p} \left. \frac{dp}{dn} \right|_\epsilon. \quad (5.1)$$

It is not only closely related to expansion dynamics but also controls the way perturbations (sound waves) travel through the fireball. Figure (5.4) shows  $c_s$  as a contour plot in the  $\epsilon - n$  phase diagram of the DE equation of state with a  $\mu_q$  dependent Polyakov potential, introduced in section (4.4). Here  $\epsilon$  is the energy density and  $n$  the net baryon number density, both given in units of the ground state values ( $\epsilon_0 = 146 \text{ MeV}/\text{fm}^3$ ,  $n_0 = 0.159 \text{ fm}^{-3}$ ).

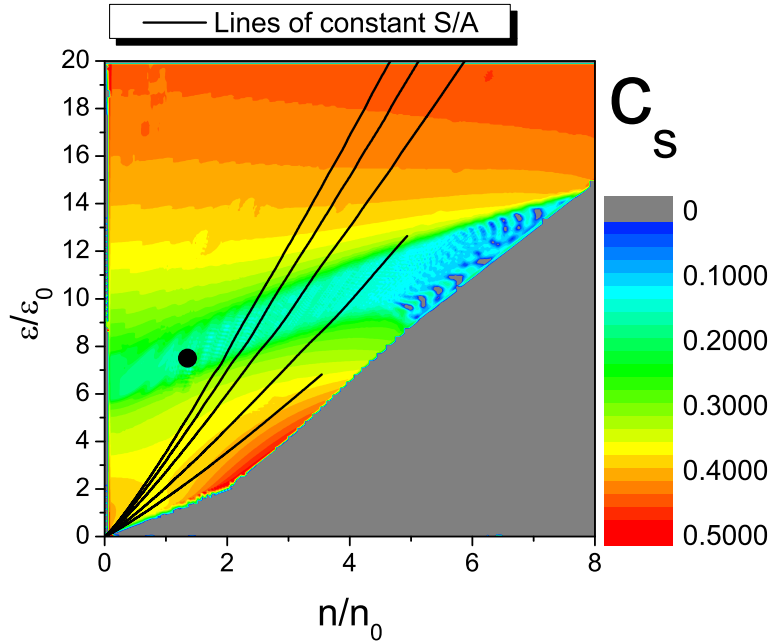


Figure 5.4: Isentropic expansion paths (black lines) and contours of the speed of sound in the  $\epsilon$ - $n$  phase diagram. The beam energies, associated with the lines, are the same as in Figure (4.3). The gray region relates to unphysical combinations of  $\epsilon$  and  $n$  ( $T \leq 0$ ). The critical endpoint of the model is displayed as the black dot.

One can clearly see the reduction of the speed of sound (softening) of the EoS in the mixed phase. The question now is, does this softening translate to a visible signal in particle properties?

To get a first approximation on how large the effect on bulk observables will be, we can calculate the average speed of sound during the fluid dynamical evolution of hybrid model calculations for most central heavy ion collisions with center of mass energies of  $\sqrt{s} =$

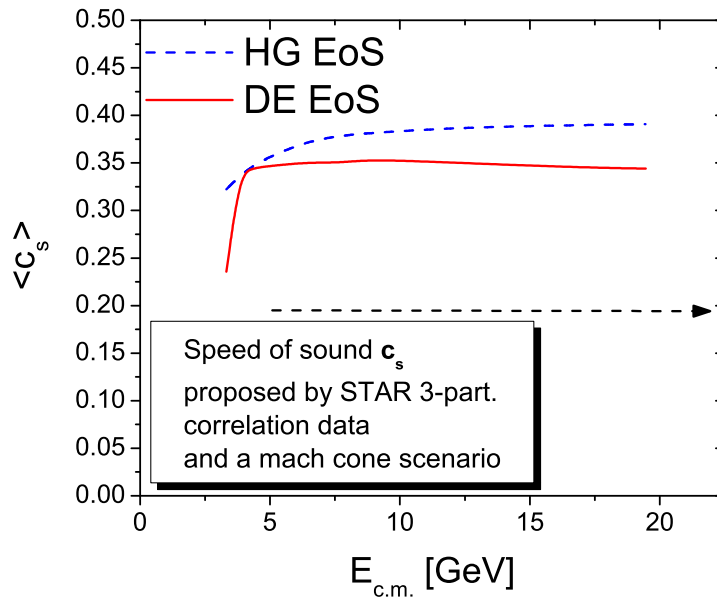


Figure 5.5: Excitation function of the averaged speed of sound in most central A+A collisions. The deconfinement EoS (red solid line) is compared to the hadron resonance gas (blue dashed line). Indicated is also the speed of sound extracted from 3 particle correlation studies at the STAR experiment [202].

3 – 20 GeV. We define the average  $\langle c_s(t) \rangle$  at a given time  $t$  as the average speed of sound over all fluid cells weighted with the energy density of that cell

$$\langle c_s(t) \rangle = \frac{\sum_{i,j,k} c_{i,j,k} \epsilon_{i,j,k}}{\sum_{i,j,k} \epsilon_{i,j,k}} \quad (5.2)$$

where the  $c_s$  of every cell can be deduced from the EoS as a function of energy and baryon number density. The speed of sound  $\langle c_s(t) \rangle$  is then averaged over the whole time evolution, where every time step has the same statistical weight.

Figure (5.5) shows the excitation function of the averaged speed of sound for both equations of state considered. The hadron resonance gas (blue dashed line) yields higher values of  $\langle c_s \rangle$  than the DE EoS (red solid line). This is expected, since the phase transition leads to a softening of the EoS. Still, in both cases the averaged speed of sound is well above  $0.3 c$ , and the difference is on a 10% level.

It was proposed, that a conical Mach wave created by in medium jets traversing the hot and dense system of a relativistic nuclear collision, could provide the means to experimentally measure the speed of sound in the fireball. Indeed, experiments at the RHIC claim to have observed conical emission in heavy-ion collisions. Applying a 3-particle correlation

method, the Mach angle  $\theta_M$  was extracted from data [202]. In a simple Mach cone picture this angle can easily be related to the speed of sound:

$$\cos(\theta_M) = c_s/v_p, \quad (5.3)$$

where  $v_p$  is the velocity of the projectile creating the wave (usually  $v_p$  is considered to be close to the speed of light). This simple approximation leads to an estimate for the speed of sound of  $\langle c_s \rangle \approx 0.2 c$ .

Since any partonic jet, which would produce a Mach wave, is created in the very early stage of the collision and traverses the medium until freeze-out, the observed angle should be related to a time average of  $c_s$  and not the speed of sound at some specific point in time. Because the system spends quite a substantial amount of time close to the phase transition region, where the EoS is soft, the averaged speed of sound is much lower than the limit for an ultrarelativistic gas  $\sqrt{1/3}$ . Still, due to the time and space average, it is substantially larger than the speed of sound in the transition region. Although the experimental result, obtained at much larger beam energies (and therefore smaller chemical potentials), is not directly related to our results at lower energies, the excitation function of  $\langle c_s \rangle$  shows a saturation at rather moderate energies and, therefore an even lower speed of sound in systems created at RHIC seems unlikely.

#### 5.1.4 Comparisons of different EoS

After these rather technical studies, we turn now to the investigation of different EoS. To exemplify the effects of the different underlying dynamics we contrast the hybrid model calculations with the pure hadronic transport calculation (UrQMD-2.3, dotted lines in figures (5.6) and (5.7)). By comparing this calculation with the hybrid calculation (employing the HRG EoS, full line with squares in figures (5.6) and (5.7)) one can estimate the effect of viscosities and the non-equilibrium dynamics. For the hybrid model calculations the gradual freeze-out with the criterion of  $5\epsilon_0$  (or  $4\epsilon_0$ ) is applied. The dashed-dotted line with triangles corresponds to the calculation with the chiral hadronic equation of state (CH) while the dashed line with circles depicts the bag model EoS with a strong first order phase transition to a hadronic model (BM).

Figure (5.6) shows the multiplicity and the mean transverse mass excitation functions for pions and protons. The yields are reduced in the hybrid model compared to the pure transport calculation because of entropy conservation during the ideal hydrodynamic evolution. The changes in the EoS do not affect the multiplicities. The mean transverse mass that is more sensitive to the pressure in the transverse plane is changed. For pions the chiral EoS gives similar results as the hadron gas calculation while the bag model EoS decreases the mean transverse mass at high energies as it is expected for a first order phase transition. The pure transport calculation reproduces the flattening in the intermediate energy regime best.



For the protons Fig. 5.6 (right) the opposite behavior can be observed. In this case, the BM EoS leads to a higher transverse mass than the chiral EoS which is still higher than the hadronic calculation. UrQMD-2.3 shows the strongest flattening again. The high baryon density regions, where most of the protons are produced at hydrodynamic freeze-out, are perhaps more sensitive to the early stage of the collision where the BM EoS exhibits a higher pressure (in the QGP phase) and the softening due to the mixed phase is only reflected in the mean transverse mass of mesons. The net baryon density is explicitly propagated in the hydrodynamic evolution. Therefore, the final distribution of the baryochemical potential at the transition from hydrodynamics to the hadronic cascade reflects the dynamics during the evolution and is sensitive to the initial stopping. The mesons are only influenced by the temperature distribution that mainly depends on the energy density distribution.

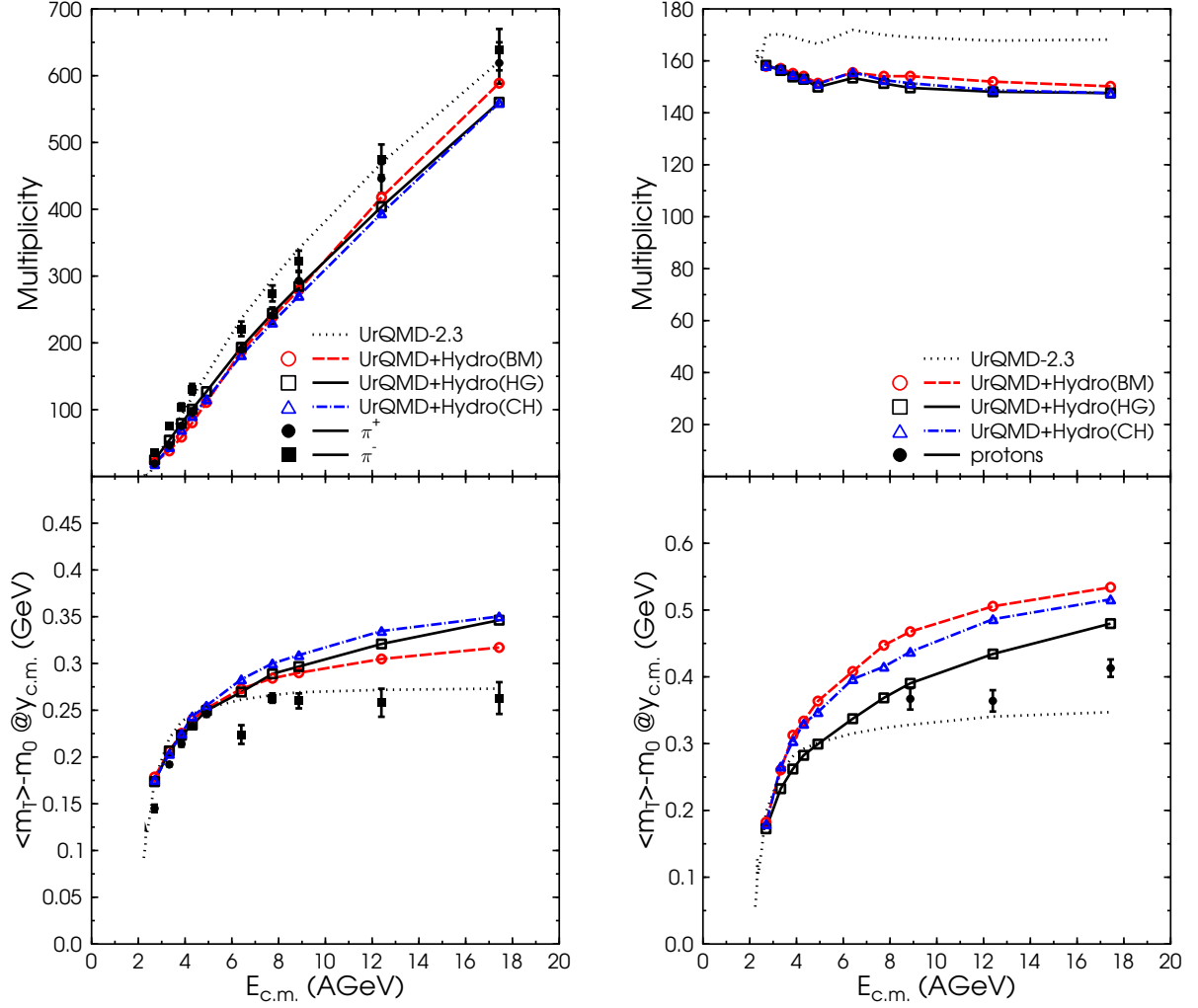


Figure 5.6: The multiplicity ( $4\pi$ , top) and the  $\langle m_T \rangle$  (bottom) excitation function for pions (left) and protons (right) in central ( $b < 3.4$  fm) Au+Au/Pb+Pb collisions at  $E_{\text{lab}} = 2 - 160$  AGeV is shown. The lines depict hybrid model calculations with different equations of state and the pure transport calculation in comparison to the experimental data [37, 183, 195, 201].

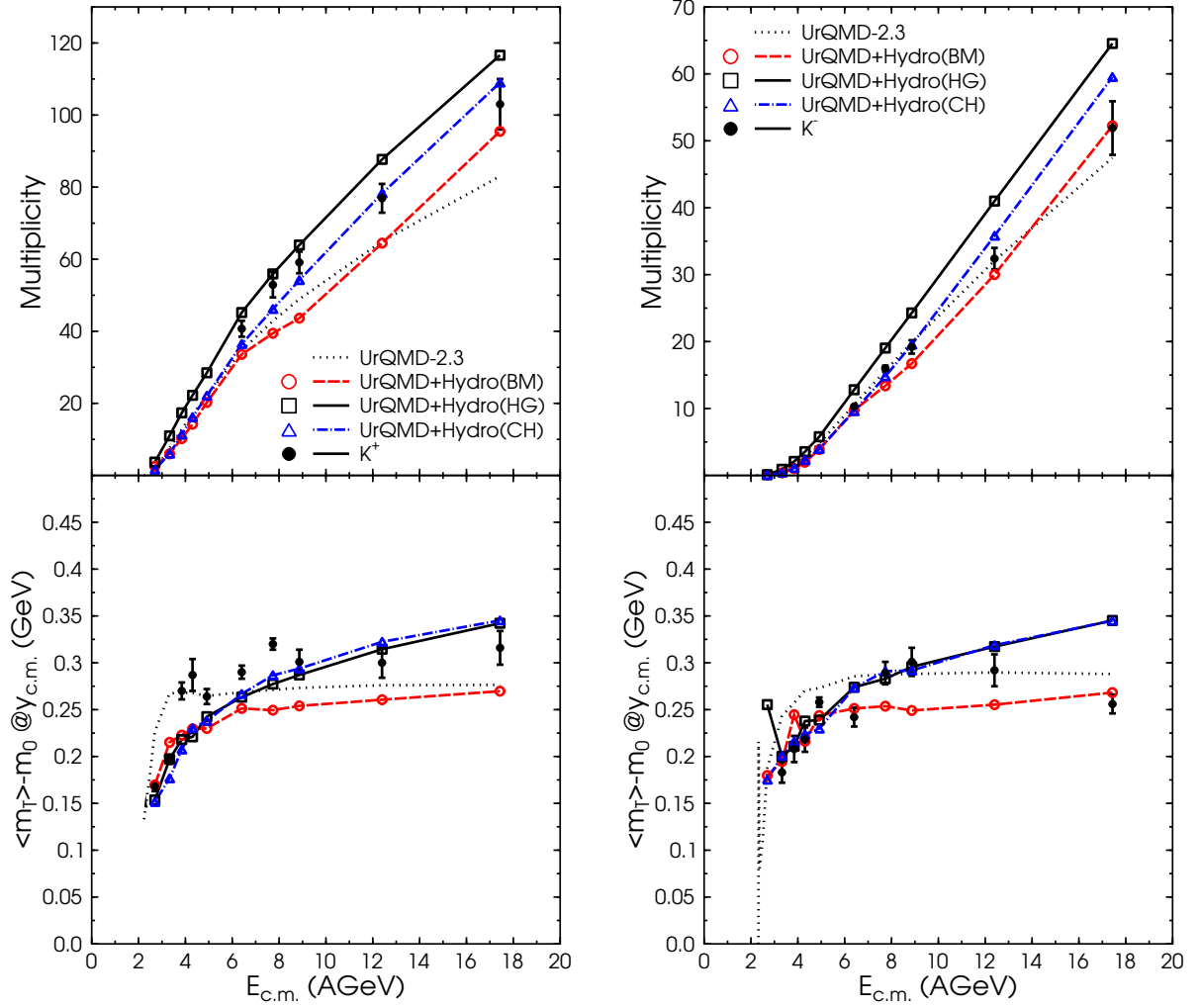


Figure 5.7: The multiplicity ( $4\pi$ , top) and the  $\langle m_T \rangle$  (bottom) excitation function for positively/negatively (left/right) charged kaons in central ( $b < 3.4$  fm) Au+Au/Pb+Pb collisions at  $E_{lab} = 2 - 160$  AGeV is shown. The lines depict hybrid model calculations with different equations of state and the pure transport calculation in comparison to the experimental data (symbols)[37, 183, 195].

Figure (5.7) shows the results for different EoS for positively and negatively charged kaons. Since the qualitative results are the same in both cases we will refer to kaons in the following without distinguishing the charges. The kaon multiplicities are higher in the hybrid model calculation as compared to the pure transport simulation, because strange particles are produced according to thermal distributions during the Cooper-Frye transition. The string and resonance dynamics in UrQMD-2.3 lead to an underestimation of strange particle yields while the mean transverse mass excitation function flattens at high AGS energies due to non-equilibrium effects. The multiplicities and the mean transverse mass are highest in the hadron gas hybrid calculation because the hadronic EoS is the stiffest EoS and can not be “softened” by non-equilibrium effects. Here also, the transverse expansion is more violent since the pressure and its gradients are large during the whole hydrodynamic evolution. The chiral EoS leads to a small decrease in the yields, but leaves the  $\langle m_T \rangle$  excitation function essentially unchanged. Employing the chiral EoS the temperatures at the transition from hydrodynamics to transport are a bit lower than in the purely hadronic case, but the kaons acquire approximately the same transverse momentum during the evolution. The chiral phase transition exhibits only a small latent heat and therefore the pressure gradients are not affected that much. The BM calculation with a strong first order phase transition produces lower kaon multiplicities than the other hybrid model calculations, at low SPS energies even less than the pure transport calculation. The transition temperatures in this case are the lowest due to the long duration of the hydrodynamic stage. For the kaons the flattening of the mean transverse mass excitation function due to the softening of the EoS is best visible. The mean transverse mass values are even lower than in the non equilibrium transport calculation.

In the following, we will continue and compare results from our calculations with DE equation of state (solid lines, see section (4.4)) including a first order phase transition, to those obtained when a HRG (dotted lines) is applied to the hydrodynamic evolution. All results shown are obtained by applying the hybrid model to most central ( $b < 3.4$  fm) heavy ion reactions (Au+Au/Pb+Pb) in a broad energy range from  $E_{\text{lab}} = 4 - 160A$  GeV.

Figure (5.8) shows the total yields of different particle species as a function of center-of-mass energy of the colliding nuclei. One can clearly see that the total multiplicities of pions and kaons reproduce the experimental data (squares) reasonably well. Multistrange hyperons like the  $\Xi^-$  are overestimated at the lowest energies, but follow the data very nicely at energies above  $E_{\text{lab}} = 11A$  GeV (At lower energies strangeness should be suppressed due to the chemical non-equilibrium of strangeness). This hints to the fact that strangeness is thermalized in heavy ion collisions at energies down to  $E_{\text{lab}} \approx 11A$  GeV. Only in the sector of heavy anti-baryons (i.e.  $\Xi^+$ ) the model yields too few particles in the full range of energies investigated. One can clearly see that the excitation functions of total particle multiplicities do not show any signal of the change of the underlying EoS. In contrast, this observable seems much more sensitive to the treatment of chemical particle freeze out.

An alternative and more microscopic way to understand an enhancement in the production

of multi-strange (anti-)baryons is related to the fragmentation of the initial color flux tubes. While one usually assumes that the initially produced color strings fragment independently, a high density of strings may allow for a recombination of color charges at the string ends, resulting in the formation of a fused string with an enhanced color field (known as color ropes) [203, 204]. These objects may be seen as an alternative to QGP formation. Extensive studies within the RQMD model have shown that particle creation from these strong color fields results in a substantial enhancement of multi-strange (anti-)baryons [205, 206].

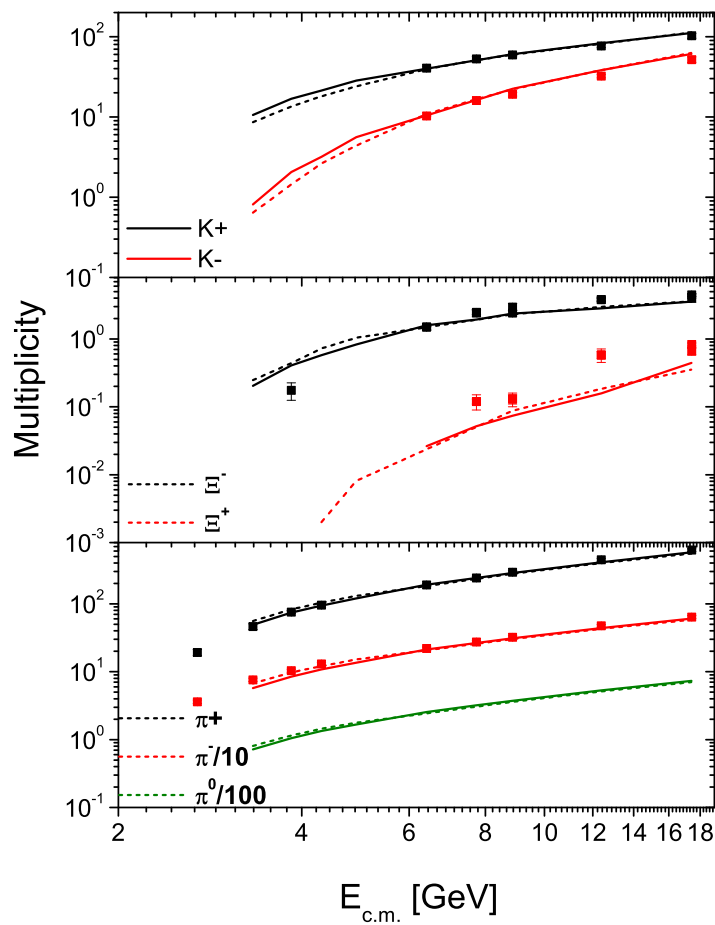


Figure 5.8: Total  $4\pi$  multiplicities of pions (lower panel),  $\Xi$ 's (middle panel) and kaons (upper panel). Data [198, 207, 208, 37, 183, 209, 210, 199, 211, 212, 213] are indicated by squares.

Next we turn to the rapidity distributions of different particles (pions, kaons and protons). Figure (5.9) shows the rapidity distributions for pions, kaons and protons at three different beam energies, again for the HRG and DE equation of state (dotted and solid lines).

For the lowest energy differences in the proton rapidity spectra can be observed, although both are, within error bars, in agreement with the data. For the  $K^+$  and  $\pi^-$  we observe a good agreement up to energies of  $E_{\text{lab}} = 40A$  GeV, while at the highest energies ( $E_{\text{lab}} = 160A$  GeV) both hybrid model calculations deviate from experiment. This may be related to our approximate choice of the hypersurface normal  $d\sigma_\mu^{(1)}$ .

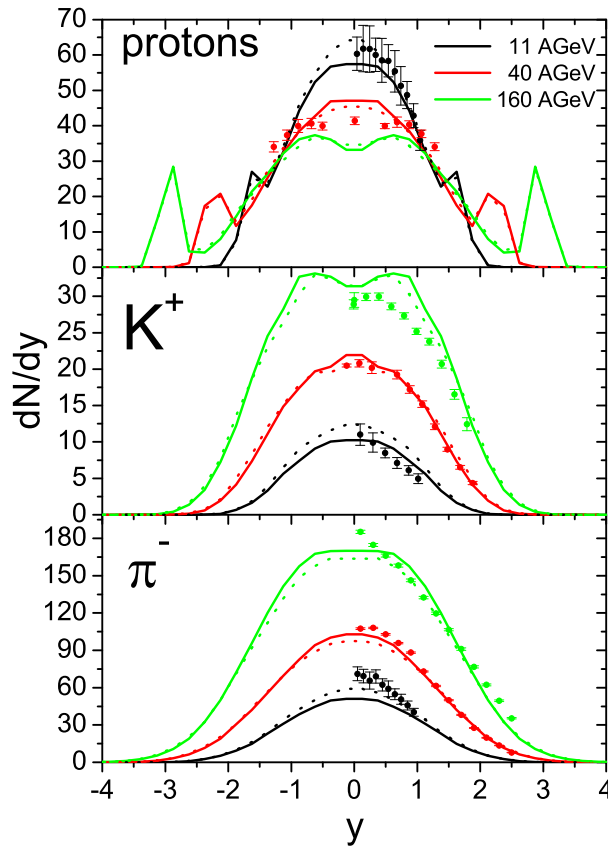


Figure 5.9: Rapidity distributions for different particle species at three different beam energies. Hybrid model calculations, DE (solid line) and HRG (dotted lines) results are compared to data (symbols) [214, 183].

<sup>1</sup>Neglecting space like components of the hypersurface leads to an overestimate of particle production at large rapidities. As we enforce baryon number conservation, the total norm of the rapidity distribution is conserved and therefore less particles should be produced at small rapidities, which can be observed in our results for the highest energies

Since the transverse momentum distributions should be sensitive to the transverse dynamics, we next turn to the investigation of the distributions of the transverse mass of different particles (pions, kaons and protons). Comparing the hybrid model calculations to data (squares), in Fig. 5.10, we find very good agreement for the lower energies. Especially the pion and kaon spectra are well in line with the data, while the proton distributions deviate slightly. Comparing the momentum distributions of the different EoS one again observes no noticeable difference between a pure hadron gas EoS and an EoS with a deconfinement transition. This hints to the fact that the final particle distributions are much more sensitive to the freeze-out procedure (thermal distribution of particles) and even more to the initial momentum distributions given by UrQMD as compared to the effects of the expansion dynamics.

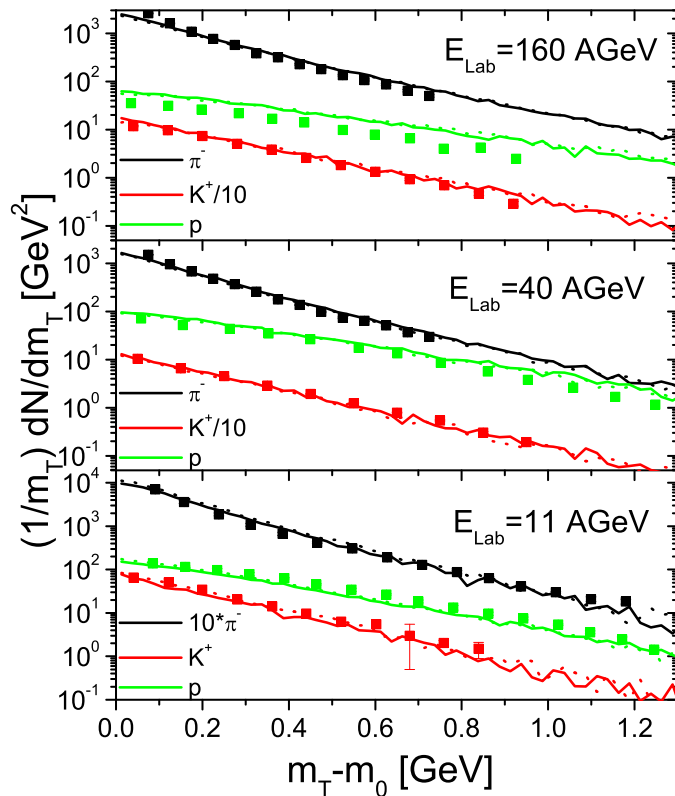


Figure 5.10: Mean transverse mass spectra of different particle species ( $\pi^-$ ,  $K^+$  and protons) at three different beam energies with the DE (solid line) and HRG (dotted lines) are compared to data [198, 30, 214, 183, 215].

Figure (5.11) shows the excitation function of the mean transverse mass of different particles, at midrapidity. Especially for the pions one observes a good agreement with data for low energies. At high energies, both hydrodynamic calculations overestimate the mean transverse momenta, while the calculation with the DE EoS gives a slightly better description of the data.

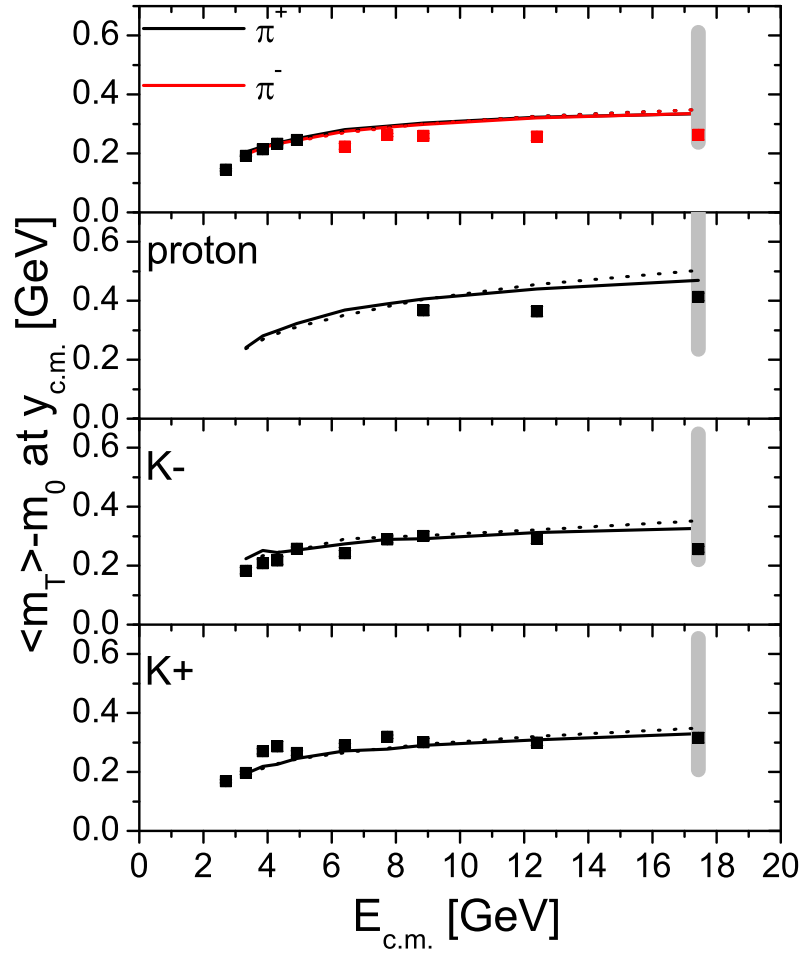


Figure 5.11: Excitation functions of the mean transverse mass of pions (upper panel), protons (upper middle panel), negatively charged kaons (lower middle panel) and positively charged kaons (lower panel) compared to data [195, 37, 183].



To get an understanding of how much the EoS can (ultimately) influence the final transverse mass spectra, we performed two additional calculations, where we set the pressure (as a function of the energy and baryon-number densities) to either 0 or  $p = 1/3\epsilon$  throughout the whole hydrodynamic evolution. These limits represent the stiffest and softest EoS possible. The results from this comparison at  $E_{\text{lab}} = 160A$  GeV are depicted in Fig. 5.11, as the gray bands, giving an upper ( $p = 1/3\epsilon$ ) and lower ( $p = 0$ ) bound on the results from the hybrid model. Note that, especially the pion mean transverse mass can only be accounted for if the (unphysically) soft EoS ( $p = 0$ ) is applied. Investigations within the hybrid model, where an EoS including a first order phase transition with a very large latent heat (very small pressure gradients) is employed, come to a similar conclusion [216]. In order to explain transverse flow data with ideal fluid dynamics in a hybrid model, an EoS with an unphysically large first order phase transition is needed.

The flattening of the mean transverse momentum as a function of beam energy was assumed to be a signal for a first order phase transition [217]. But as has been pointed out above the slow increase of the mean transverse mass at increasing beam energy can be related to non equilibrium effects, and may be modeled by the inclusion of viscous hydrodynamics.

The multiplicities are reasonable well reproduced in all the different scenarios, but the mean transverse mass excitation function reflects the different transverse pressure gradients due to the underlying EoS. The experimentally measured step-like behavior can either be attributed to a first order phase transition with an unphysically large latent heat or a softening of the EoS due to hadronic non-equilibrium effects.

To bring the calculations to a better agreement four options with different (dis)advantages may be explored:

1. Inclusion of potential interactions in the initial and/or final stage of the transport calculations. This might help to lower the mean transverse momentum of hadrons that are attracted by the potential interaction. However, it would lead to a higher pressure (and therefore  $\langle m_T \rangle$ ) especially for the protons which are already overestimated by the existing approach.
2. Changing the equation of state. Another possibility is to increase the latent heat in the bag model EoS to get a stronger effect of the softening. This would eventually reduce the  $\langle m_T \rangle$  of all hadrons bringing it nearer to the data. However, it would lead to a further increase of the expansion times due the long timespan that the system spends in the mixed phase. This lifetime increase seems not to be supported by observables, like HBT radii, that are sensitive to the lifetime of the fireball.
3. Modifications of the freeze-out. The freeze-out prescription is a further crucial ingredient as it has been shown in the last Section. In the present approach, a transition criterion on a constant hypersurface and the Cooper-Frye-approach is used. However, one might also think of a continuous emission approach to the decoupling problem

without involving the Cooper-Frye prescription. Here particle emission is integrated over various stages of the reaction and might result in a change of the transverse momentum spectra compared to the CF approach. These models have been explored e.g. in [218, 219].

4. Viscosities. All calculations with the ideal hydrodynamics intermediate stage over-predict the  $\langle m_T \rangle$ , however, the non-equilibrium approach UrQMD is generally on the lower side of the data, non-equilibrium effects seem to play an important role. Thus, adding additional viscosity during the hydrodynamic evolution might be the most promising idea to improve the overall agreement with the experimental data.

## Flow

Another observable that is deemed to be a signal for the deconfinement phase transition is the so called 'anti-flow' (or third flow component). In [99, 220, 221] it was suggested that a first-order phase transition leads to a prominent wiggle in the directed flow  $v_1 = \langle p_x/p_T \rangle$  as a function of rapidity. Data [36], indeed, show a wiggle in the directed flow in most central collisions at  $E_{\text{lab}} = 40A$  GeV. Fig. 5.12 shows  $v_1$  of pions (circles) and protons (squares) as a function of rapidity (over  $y_b$ , the beam rapidity) for different model calculations, compared to data (green stars and diamonds). Here, we compare both hybrid model calculations (with the HRG and DE equation of state) and a pure transport calculation [222] (UrQMD without any hydrodynamic stage). As one can see all models yield very similar results and none can reproduce the behavior of the proton  $v_1$ . The pion  $v_1$  is very well in line with data for both hydrodynamic calculations. Note that even the sign change for the pions as compared to protons is reproduced. Still, changing the EoS does not lead to distinguishable differences in the extracted directed flow. The directed flow seems to be mostly sensitive to the initial conditions and less to the subsequent hydrodynamical expansion. This is in line with previous findings, where the inclusion of nucleon potentials (mean field effects) in transport models improved the description of the proton directed flow as measured by experiment [223, 224].

Figure (5.12) again shows the directed flow of protons for a smaller window in rapidity. The change of sign in proton flow can be clearly seen in the data, but neither model calculation (hybrid model with and without phase transition) describes this phenomena (not even qualitatively). Disregarding this single data point, the pure transport calculation provides the best description of the directed proton flow.

Finally in figure (5.13) displays the elliptic flow of pions as a function of transverse momentum, calculated within the pure transport approach (UrQMD-2.3) and in the hybrid approach employing different equations of state (HRG, Chiral Hadronic model and BM), for mid-central ( $b=5-9$  fm) Pb+Pb collisions at  $E_{\text{lab}} = 40A$  GeV and  $E_{\text{lab}} = 160A$  GeV. The symbols represent the corresponding experimental data that have been measured by the NA49 collaboration applying different measurement methods [36]. The hydrodynamic evolution leads to higher elliptic flow values especially at higher  $p_t$  even without an explicit phase transition, while the pure transport calculation underpredicts the data. Within this new hybrid approach, with more realistic initial conditions and freeze-out prescription, the effect of viscosity and non-equilibrium dynamics seems to be much stronger than the equation of state dependence.

This finding is quite surprising since the expansion times differ for the three different scenarios as it can be estimated from the  $R_O/R_S$  ratio [225]. The overall magnitude of the pion transverse momentum is also affected by the EoS [216], but the anisotropy remains unchanged. From this, one could draw the conclusion that most of the elliptic flow is already built up during the initial scatterings in UrQMD, but we have checked that most

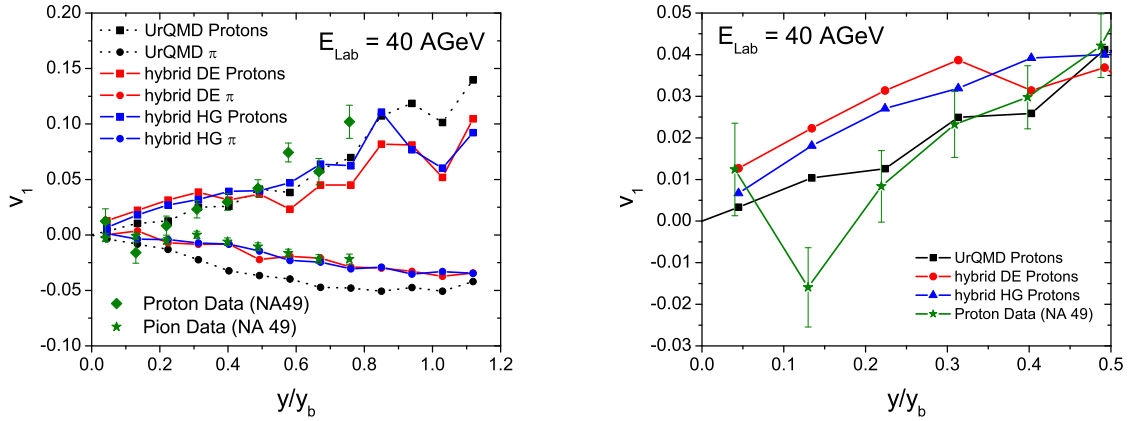


Figure 5.12: (color online) left: The directed flow  $v_1$  for pions and protons at  $E_{\text{lab}} = 40A$  GeV for both hybrid model calculations (blue HG and red DE lines) compared to default UrQMD results (black dashed lines) and data (green stars and diamonds).  $y_b$  refers to the beam rapidity [36]. right: The directed flow  $v_1$  for protons at  $E_{\text{lab}} = 40A$  GeV for both hybrid model calculations (blue triangles HG and red circles DE) compared to default UrQMD results (black squares) and data (green stars) [36].

of the flow is generated as expected during the hydrodynamic evolution. Therefore, we conclude that the effect of the softer EoS which should reduce the elliptic flow is canceled by the longer expansion times in this case.

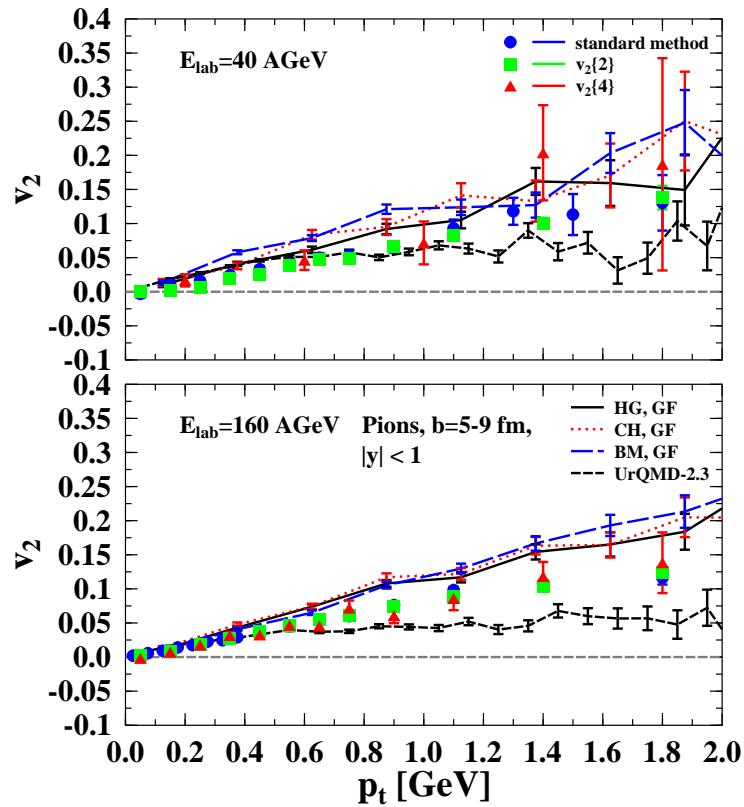


Figure 5.13: Elliptic flow of pions in mid-central ( $b=5-9$  fm) Pb+Pb collisions at  $E_{\text{lab}} = 40A$  GeV and  $E_{\text{lab}} = 160A$  GeV. The full black line depicts the hybrid model calculation with hadron gas EoS (HG), the red dotted line represents the chiral EoS (CH) and the blue long-dashed line the bag model EoS (BM) while the pure transport calculation is shown as the black dashed line (UrQMD-2.3). The colored symbols display experimental data obtained with different measurement methods by NA49 [36].

## 5.2 Production of hypernuclei in HIC

Exotic forms of deeply bound objects with strangeness have been proposed long ago (see [229]) as collapsed states of matter, either consisting of baryons or quarks. For example the  $H$  di-baryon (a six quark state) was predicted by Jaffe [230]. Later a multitude of bound di-baryon states with strangeness were proposed using quark potentials [231, 232] or the Skyrme model [233]. However, the (non-)observation of multi-quark bags, e.g. strangelets and (strange) di-baryons is still one of the open problems of intermediate and high energy physics. Most noteworthy in this respect has been the hunt for the Pentaquark over the last 10 years, which re-stimulated this field and resulted in a reported observation at the CERN SPS accelerator [35].

The early theoretical models based on  $SU(3)$  and  $SU(6)$  symmetries [234, 4] and on Regge theory [235, 236] suggest that di-baryons should exist. More recently, even QCD-inspired models predict di-baryons with strangeness  $S = 0, -1,$  and  $-2$ . The invariant masses range between 2000 and 3000 MeV [230, 237, 238, 239, 240, 241, 242, 243]. Unfortunately, masses and widths of the expected 6-quark states differ considerably for these models. Nevertheless, most QCD-inspired models predict di-baryons and none seems to forbid them.

On the conventional hadronic side, however, hypernuclei are known to exist already for a long time [244, 245]. The double  $\Lambda$  hypernuclear events reported so far are closely related to the  $H$  di-baryon [246]. Metastable exotic multi-hypernuclear objects (MEMOs) as well as purely hyperonic systems of  $\Lambda$ 's and  $\Xi$ 's were introduced in [247, 248] as the hadronic counterparts to multi-strange quark bags (strangelets) [249, 250]. Most recently, the Nijmegen soft-core potential was extended to the full baryon octet and bound states of  $\Sigma\Sigma$ ,  $\Sigma\Xi$ , and  $\Xi\Xi$  di-baryons were predicted [251]. For previous estimates of strangelet production and MEMO formation, the reader is referred to [252, 253].

A major uncertainty for the detection of such speculative states is their (meta)stability. Metastable exotic multi-hypernuclear objects (MEMOs), for example, consist of nucleons,  $\Lambda$ 's, and  $\Xi$  and are stabilized due to Pauli's principle, blocking the strong decay of the hyperons into nucleons. Only few investigations about the weak decay of di-baryons exist so far (see [243] for a full discussion and new estimates for the weak nonleptonic decays of strange di-baryons): In [254], the  $H$ -di-baryon was found to decay dominantly by  $H \rightarrow \Sigma^- + p$  for moderate binding energies. While the  $(\Lambda\Lambda)$  bound state, which has exactly the same quantum numbers as the  $H$ -di-baryon, was studied in [255]. Here, the main non-mesonic channel was found to be  $(\Lambda\Lambda) \rightarrow \Lambda + n$ . If the life time of the  $(\Lambda\Lambda)$  correlation or  $H^0$  particle is not too long, the specific decay channels might be used to distinguish between both states.

### 5.2.1 From the fireball

Massive heavy-ion reactions provide an abundant source of strangeness. More than 50 hyperons and about 30 Anti-Kaons (i.e.  $K^- + \bar{K}^0$  carrying the strange quark) are produced in central collisions of lead nuclei at the CERN-SPS low energy program and before that at the AGS (see e.g. [5]). In the near future, the Facility for Anti-proton and Ion Research (FAIR) will start to investigate this energy regime closer with much higher luminosity and state-of-the-art detector technology. This opens the exciting perspective to explore the formation of composite objects with multiple units of strangeness so far unachievable with conventional methods.

There are several searches in heavy-ion collisions for the  $H$ -di-baryon [256, 257, 258] and for long-lived strangelets [259, 260] with high sensitivities, so far with no conclusive results. In  $pN$  collisions at the Fermilab however, the  $H$ -di-baryon seems to be excluded over a wide range of Masses ( $2.194 < M_H < 2.231$  GeV) and lifetimes ( $5 \cdot 10^{-10}$  to  $1 \cdot 10^{-3}$  sec) [261]. Hypernuclei have been detected most recently in heavy-ion reactions at the AGS by the E864 collaboration [262] and the STAR collaboration [6].

Cluster	Mass [GeV]	Quark content
${}^4He$	3.750	$12q$
$H^0$	2.020	$4q + 2s$
$\alpha_q$	6.060	$12q + 6s$
$\{\Xi^-, \Xi^0\}$	2.634	$2q + 4s$
$\{4\Lambda\}$	4.464	$8q + 4s$
$\{2\Xi^-, 2\Xi^0\}$	5.268	$4q + 8s$
${}^5_{\Lambda}He$	4.866	$14q + 1s$
${}^6_{\Lambda\Lambda}He$	5.982	$16q + 2s$
${}^7_{\Xi^0\Lambda\Lambda}He$	7.297	$16q + 2s$
$\{2n, 2\Lambda, 2\Xi^-\}$	6.742	$12q + 6s$
$\{2\Lambda, 2\Xi^0, 2\Xi^-\}$	7.500	$8q + 10s$
$\{d, \Xi^-, \Xi^0\}$	4.508	$8q + 4s$
$\{2\Lambda, 2\Xi^-\}$	4.866	$6q + 6s$
$\{2\Lambda, 2\Sigma^-\}$	4.610	$8q + 4s$

Table 5.1: Properties of all considered multibaryonic states

To calculate the multiplicities of MEMOS in the FAIR energy region, we employ the introduced hybrid approach to heavy ion collisions. For the results presented here an equation of state for a hadron-resonance gas without any phase transition is used [263] (HRG). One should note that we apply a purely hadronic EoS, for energy densities where a transition to the QGP is expected. Final particle (and MEMO) multiplicities are mainly sensitive on the degrees of freedom at chemical freeze out which is reflected in the hadronic EoS.

Dynamical observables such as momentum and rapidity spectra are more sensitive on the underlying dynamics. In addition, a phase transition could catalyze a strangeness distillation process further enhancing MEMO production. However, studying the effects of a phase transition on MEMO production is left subject of future investigations.

When the energy density drops below  $5\epsilon_0$  ( $\sim 730\text{MeV}/\text{fm}^3$ ) the freeze-out is performed and MEMOs and strangelets are produced according to the Cooper-Frye description (3.12). As distinctive inputs for the distribution functions, the chemical potentials ( $\mu_s, \mu_B$ ) and masses of the MEMOs enter. Final state interactions of these MEMOs are neglected for the present study. Table (5.1) gives the properties of all multibaryonic states considered in our analysis. They are the most promising and stable candidates.

Figure (5.14) provides the total multiplicities per degeneracy factor of various types of MEMOs and strangelets in central Pb+Pb reactions at  $E_{\text{lab}} = 30A$  GeV. The yields obtained are in good comparison to the statistical model analysis [265], which is describing strange cluster production at AGS energies.

One should also note that we assume particle production from a grand canonical ensemble for all beam energies. Because local, as well as global, thermal equilibration are assumptions not necessary justified in heavy ion collisions, a microcanonical description, combined with MEMO production by coalescence, has been proposed in [242]. Due to the restrictions of energy and momentum conservation, resulting in a phase space reduction for produced strange particles a (micro)canonical description of the system strongly decreases strange particle yields [189, 190, 193].

On the other hand, thermal models are able to reproduce strange particle yields for beam energies above  $E_{\text{lab}} \approx 8A$  GeV very well, and canonical corrections become negligible above these energies [193].

Investigating strange-cluster production over a range of beam energies shows a distinct maximum in the yields of several multi strange objects. Fig. (5.15) displays the excitation function of the multiplicities of various MEMOs in central Pb+Pb reactions from the hybrid approach. The presented MEMO candidates are expected to possess binding energies up to  $E_B/A_B \approx -22$  MeV [250]. One easily observes that the upper FAIR energy region ( $\sim E_{\text{lab}} = 10 - 40A$  GeV) is ideally placed for the search of exotic multi-strange baryon clusters. At lower energies, the hyperon production cross section is too small, while at energies above FAIR, the expansion of the source and the small baryo-chemical potential suppress the formation of MEMOs and strangelets.

Using the hybrid model enables us to also explore the phase space distribution of the produced particles. Fig. (5.16) shows the rapidity density of various MEMOs in central Pb+Pb reactions at  $E_{\text{lab}} = 30A$  GeV from the hybrid approach. The production of baryon rich clusters is most pronounced in the high baryon density rapidity region. The rapidity



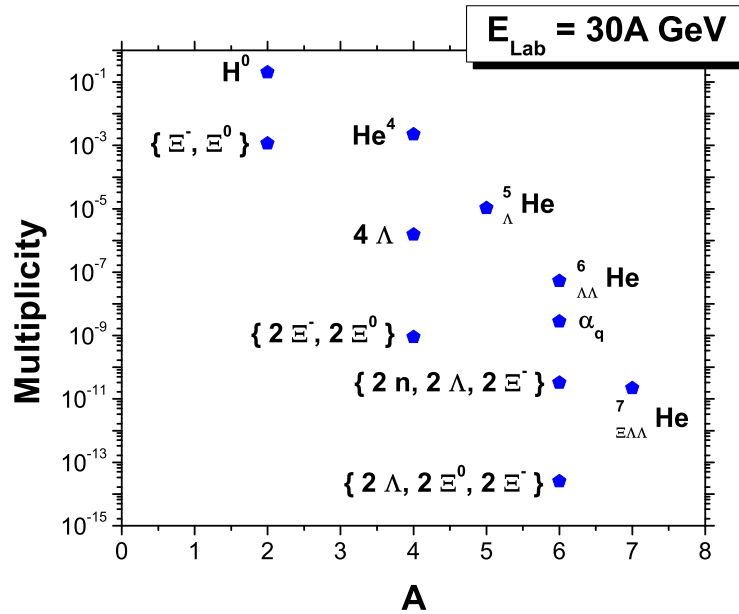


Figure 5.14: Multiplicities of various types of MEMOs and strangelets in central Pb+Pb reactions at  $E_{lab} = 30A$  GeV from the hybrid approach.

distributions for MEMOs with a larger strangeness to baryon number fraction tend to look more Gaussian like.

Figure (5.17) depicts the transverse momentum distribution of various MEMOs at midrapidity in central Pb+Pb reactions at  $E_{lab} = 30A$  GeV from the hybrid approach. The  $p_T$  spectra are rather broad as compared to usual hadrons. This is due to the large boost the MEMOs acquire due to their large mass and the fact, that they are produced predominantly in the hottest regions of the expanding system.

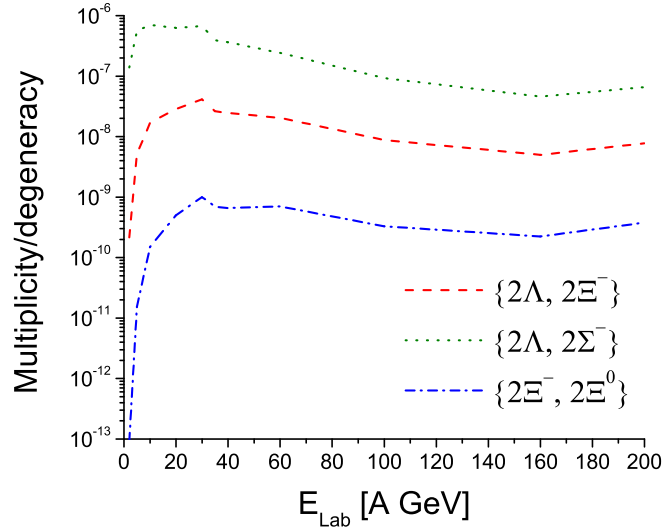


Figure 5.15: Excitation functions of the multiplicities of various MEMOs in central Pb+Pb reactions from the hybrid approach.

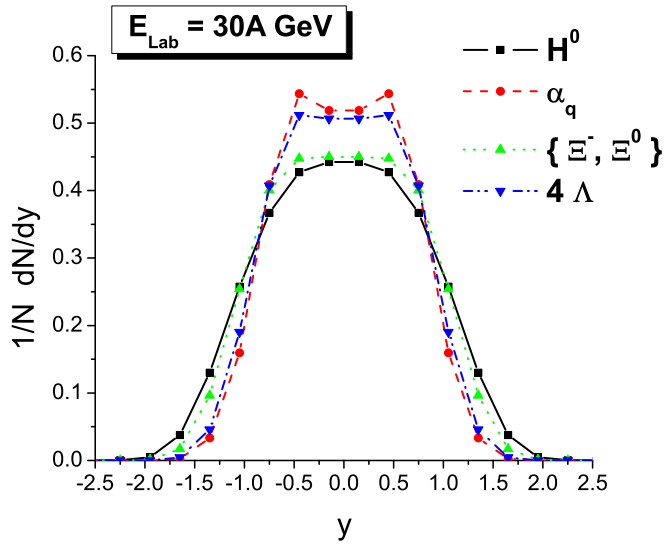


Figure 5.16: Normalized rapidity density of various MEMOs in central Pb+Pb reactions at  $E_{\text{lab}} = 30A$  GeV from the hybrid approach.

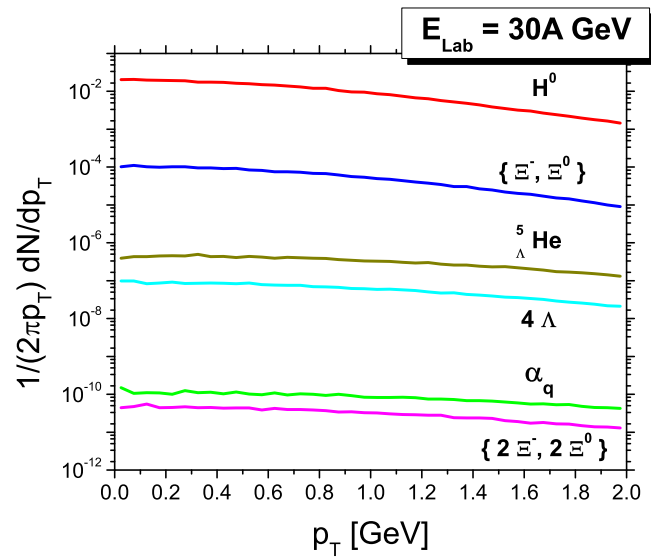


Figure 5.17: Transverse momentum spectra at midrapidity ( $|y| < 0.5$ ) of various MEMOs in central Pb+Pb reactions at  $E_{\text{lab}} = 30A \text{ GeV}$  from the hybrid approach.

The field of hypernuclear physics has come to more attention quite recently with the announcement of the detection of a single  $\Lambda$  hypernuclei at the STAR experiment, with gold beams of an energy of  $\sqrt{s} = 200A$  GeV [6]. In addition not only the hypertriton was measured, but also its anti-particle, the anti-hypertriton. This means the first ever measurement of a anti-strange composite object.

We now extend our investigations with the hybrid model on the production of light hypernuclei and MEMOs to much higher energies. Usually investigations with our hybrid approach are problematic at energies above  $E_{lab} = 160A$  GeV because of the large Lorentz contraction of the system in longitudinal direction. Because the model uses a Euclidian grid with fixed grid length in all three spacial dimensions the gradients in the longitudinal direction would soon become to large and the numerical solutions become unstable. this could only be resolved by describing the longitudinal expansion in a Lorentz invariant frame e.g. making a coordinate transformation from the spacial z-coordinate to the pseudo-rapidity  $\eta$ . Although work along this line is in progress, this would be to involved for our simple model study and therefore we adapt an alternative approach. At large beam energies the zransverse dynamics should be approximately independent from the longitudinal dynamics. This fact is usually exploited in fluid dynamical models that only propagate the thermodynamic fields in two dimensions. We therefore introduce a rapidity cut for particles that are transfered into the fluid dynamical model after the initial state from the UrQMD model. In other words, only particles with a rapidity between -2 and 2 will be transformed into the propagated fluid, while all other particles will be propagated in the transport model. This procedure of course will not be able to create physically reasonable results for observables as a function of rapidity but if only observables at mid rapidity are investigated should yield reasonable results for the RHIC and LHC energies.

Figure (5.18) shows an excitation function of the yield per  $\Lambda$  for the most likely light strange clusters and an energy range from AGS ( $\sqrt{s} \approx 10A$  GeV) to LHC energies  $\sqrt{s} \approx 1A$  TeV. As has been pointed out above, multi baryonic strange clusters are most abundant in the low energy region.

Having at hand results at  $\sqrt{s} = 200A$  GeV enables us to compare our thermal rates with rates that were calculated using a transport model and subsequent coalescence of reaction products. The colored squares in Figure (5.18) depict coalescence results from [242]. Both methods of estimating the production yields of hypernuclei give rather similar results, which means that both approaches are equally applicable.

Figure (5.19) shows our results from the hybrid model on the production of anti-hypernuclei and anti-MEMOs. As matter and anti-matter is produced more equally when the beam energy is increased, anti-cluster become accessible at the RHIC collider and more so at the LHC in the near future. Here it would not only be interesting to confirm the finding of the anti-hypertriton, but also to look at other possibly bound states like the  $\Xi$ -dibaryon and its anti-particle.

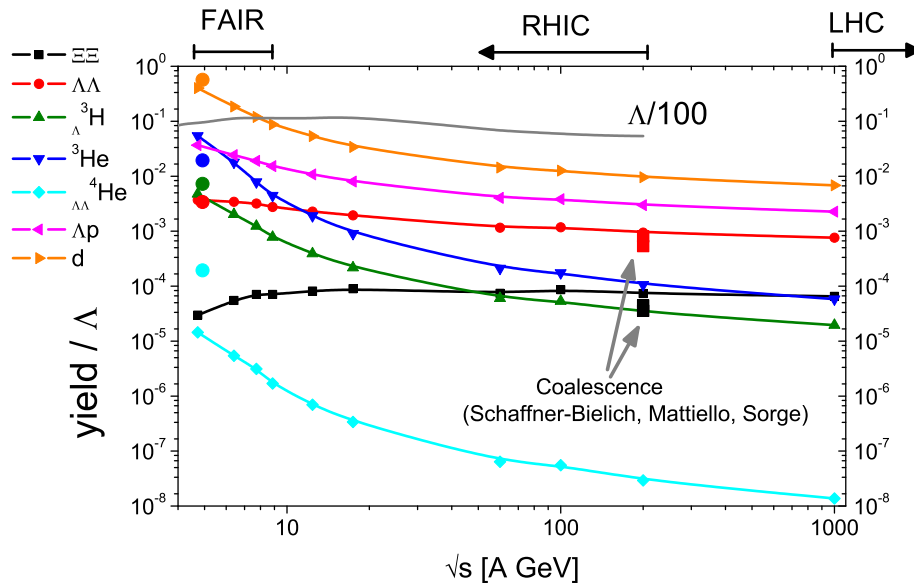


Figure 5.18: Excitation function of the multiplicity of several hypernuclei and di-baryons

As experiments with lower energy are more promising for the production of multi baryonic objects, several experiments at the future FAIR facility will perform ambitious research on hypernuclear physics. At the Panda experiment for example, precision gamma-ray spectroscopy of single and double hypernuclei will be performed to extract information on their structure, on the hyperon-nucleon and hyperon-hyperon interaction and to study of the weak decays of these objects.

As the FAIR accelerator offers an unprecedented beam intensity for heavy ion experiments, hypernuclei and multi-hypernuclear objects will be produced abundantly in the CBM experiment [266]. Here the strange matter clusters are created from a hot and dense fireball. In the following we will discuss the production of the single  $\Lambda$ -Hypernucleus from thermal equilibrium. More precisely we will calculate the following ratio  $R_H$  for central collisions of Pb+Pb and a wide range of beam energies.

$$R_H = \frac{^3\Lambda H}{^3He} \cdot p/\Lambda \quad (5.4)$$

This ratio is especially interesting, as it does not depend on the chemical potential of the particles (as fugacities cancel), and any canonical correction factors for strangeness are canceled.

For simplicity, we have neglected the contribution of the feed down from higher resonances to the  $\Lambda$  and proton yields. This contribution will be discussed later. To get a sophisticated picture of thermal production we calculate  $R_H$  with the hybrid model to heavy ion

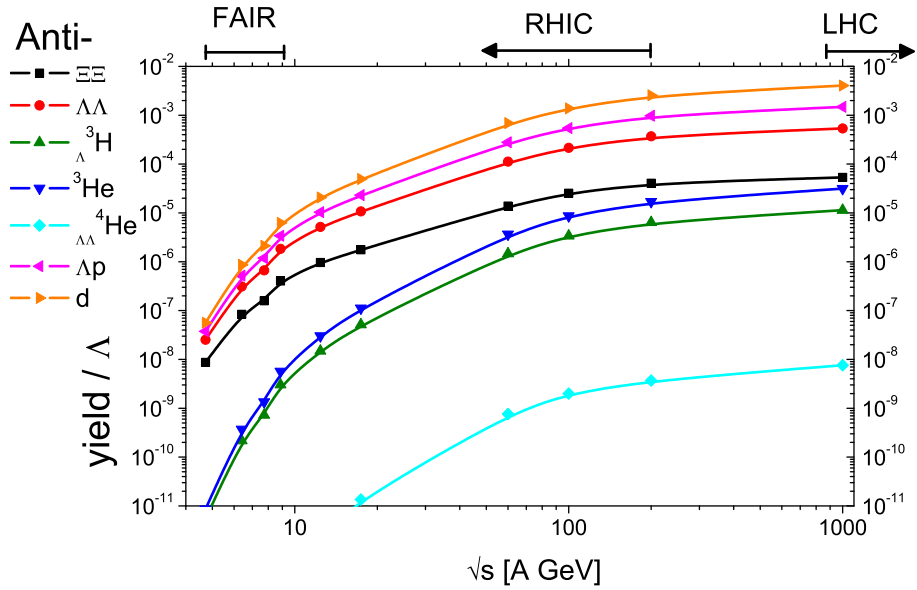


Figure 5.19: [Excitation function of the multiplicity of several anti-hypernuclei and anti-baryons]

collisions. At the transition hypersurface from Hydrodynamics to transport all particles are thermally produced according to the Cooper Frye prescription [264].

The solid line in figure (5.20) shows results on  $R_H$  from the hybrid model, extracted at the transition surface from hydrodynamics to transport.

When final state interactions (FSI), like resonance decays and creation, are explicitly included in the transport phase, the result changes significantly (dashed line). Nevertheless the it still does not depend on the beam energy. Note that we neglected contributions to  ${}^3_\Lambda H/{}^3He$  from FSI (e.g. via coalescence of decay products) which should again increase  $R_H$ .

One thing to note when calculating this ratio is the fact that, while the  $\Sigma$ -baryon does contribute significantly to the total  $\Lambda$  yield, it does not contribute to the  ${}^3_\Lambda H$  yield. Including the contribution of the  $\Sigma$  to the number of  $\Lambda$ 's changes  $R_H$  greatly, as can be seen in figure (5.20).

Comparing our different results to data taken at the AGS [268], a large discrepancy can be seen, while recent results from RHIC experiment are in line with predictions from thermal production. When the  $\Sigma$  contribution is included, our result compares more favorably with the AGS data and not the STAR data. It therefore could be that the  $\Sigma$  contribution in the experimental values has to be reclarified. Otherwise this discrepancy can be explained by the non equilibrium (not canonical) nature of strangeness production at AGS energies. The FAIR facility therefore offers the opportunity to study the production of such hypernuclei

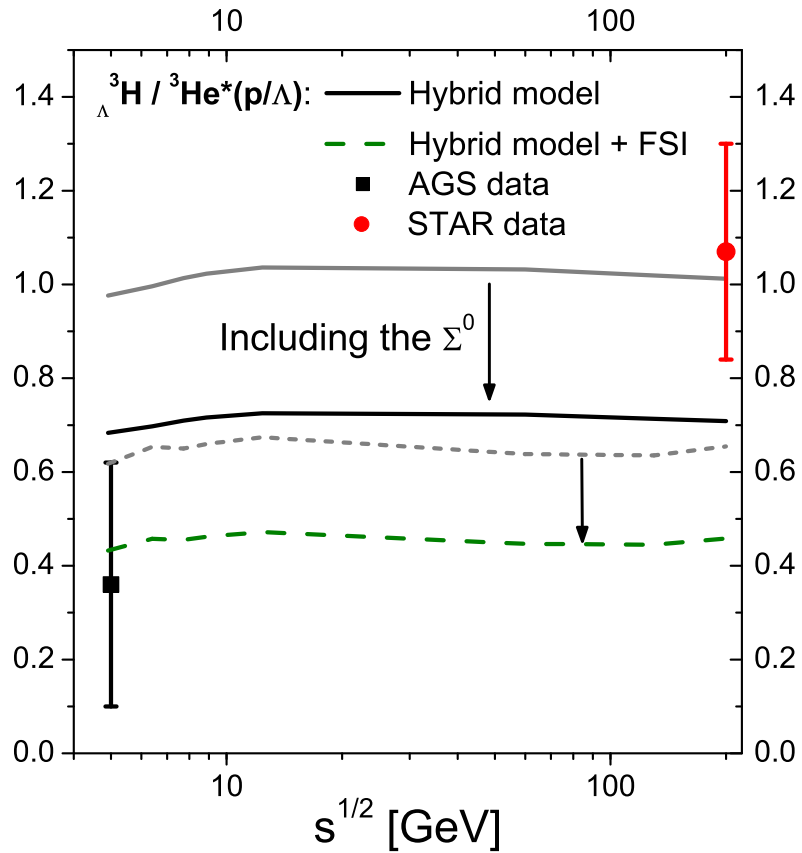


Figure 5.20: Excitation function of the ratio  $R_H$  (see text) for different model calculations compared to data [268]. The grey region indicates preliminary results from the STAR experiment [269].

over a very interesting range of beam energies. It may prove to be a unique tool to study the process of strangeness equilibration which can be closely related to the formation of a QGP [184, 185, 186, 187, 188].

### Fluctuations

For the present study so far we have assumed global as well as local strangeness conservation. These assumptions are common for models including thermal production of particles. In the following we explore if that assumption of local strangeness conservation is justified, especially in the FAIR energy regime. A relaxation of this assumption within the hybrid approach will require the explicit propagation of the strangeness density (similar to the treatment of the baryon density). A second key ingredient will be the inclusion of an equation of state that can provide  $p(\epsilon, \rho_B, \rho_s)$  with a finite  $\rho_s$ . However, first we explore if such an extension might be necessary by applying the UrQMD model without an intermediate hydrodynamic phase.

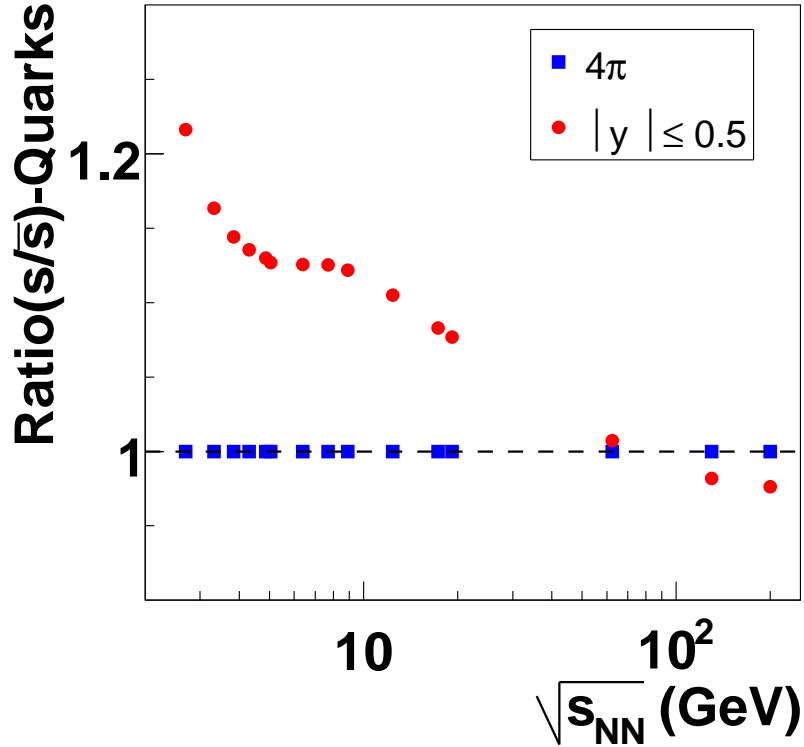


Figure 5.21: Energy dependence of the strange quark over anti-strange quark ( $s/\bar{s}$ ) ratio for central Pb+Pb/Au+Au reactions. Circles show the ratio at midrapidity, while squares show the  $4\pi$  values where the ratio is unity due to strangeness conservation.

We start with an investigation of the strangeness production and its distribution as a function of energy. Figure (5.21) depicts the energy dependence of the strange quark over anti-strange quark ( $s/\bar{s}$ ) ratio for central Pb+Pb/Au+Au reactions. The red circles present the strangeness to anti-strangeness ratio at midrapidity, while the blue squares show the  $4\pi$  values where the ratio is unity due to strangeness conservation. One clearly observes



that strangeness is not evenly distributed over rapidity, leading to an asymmetry between strange and anti-strange quarks on the level of 20% in the relevant energy regime. A similar kind of strangeness separation process has been predicted long ago within models coupling a hadron gas to a Quark-Gluon-Plasma state [181, 270]. Within these models the energy and particle number balance in the mixed phase supports a 'distillation' process that enriches the QGP phase with strangeness and the hadronic phase with anti-strangeness (See section (4.4.4)). Within the present model, however, hadronic interactions are responsible for the phase space separation of strangeness and anti-strangeness since no first order phase transition is present. Since both procedures separate strangeness in an equivalent way one can expect an even stronger strangeness separation if both effects are at work.

Figure (5.22) shows the rapidity dependence of the strange quark over anti-strange quark ( $s/\bar{s}$ ) ratio for central Pb+Pb/Au+Au reactions at AGS ( $E_{lab} = 2 - 11A$  GeV), SPS ( $E_{lab} = 20 - 158A$  GeV) and RHIC ( $\sqrt{s_{NN}} = 19 - 200$  GeV) energies. In the AGS and SPS energy regime, the ( $s/\bar{s}$ ) ratio is strongly rapidity dependent and has a pronounced peak above unity near midrapidity. At RHIC energies, the ( $s/\bar{s}$ ) ratio turns into a box shape as a function of rapidity with a plateau at unity indicating that strangeness is locally neutralized in rapidity. At the highest RHIC energies, the ( $s/\bar{s}$ ) ratio even turns slightly smaller than 1. Continuing this trend one would expect a clearly smaller than 1 ( $s/\bar{s}$ ) ratio at LHC energies. In consequence, statistical model approaches (with the constraint of strangeness conservation at mid rapidity [193]) are allowed to use midrapidity particle ratios as input for their calculations only at low RHIC energies. At lower, as well as higher energies, this procedure is not justified as strangeness neutralization does not hold for the central rapidity region. Thermal calculations, using full phase space data as an input [271, 272], and results from a thermal model including a core-corona scenario [273], generally give better descriptions of strange particle data, supporting the idea of dynamical strangeness separation, as proposed by this work.

Figure (5.23) provides the transverse momentum dependence of the strange quark over anti-strange quark ( $s/\bar{s}$ ) ratio for central Pb+Pb/Au+Au reactions at AGS ( $E_{lab} = 2 - 11A$  GeV), SPS ( $E_{lab} = 20 - 158A$  GeV) and RHIC ( $\sqrt{s_{NN}} = 19 - 200$  GeV) energies. Here one observes a strong separation of strangeness in transverse direction. With decreasing energy (increasing baryo-chemical potential) the distribution of (anti-)strangeness becomes increasingly non-uniform in momentum space. The low momentum region is depleted of strange quarks, while the high  $p_T$  region shows a strong enhancement of strange quarks compared to anti-strange quarks. This can be intuitively linked to the fact that (multi)strange baryons have a larger inverse slope than the Kaons for a given transverse velocity due to their larger masses.<sup>1</sup>

---

<sup>1</sup>If one assumes strangeness conservation as well as vanishing net baryon number at midrapidity (as is expected at very high energies) then these distributions should be flat, as particles and their antiparticles are produced in equal numbers. If the ( $s/\bar{s}$ ) ratio does deviate from unity the separation of strangeness in momentum space should still be present even at vanishing net baryon number.

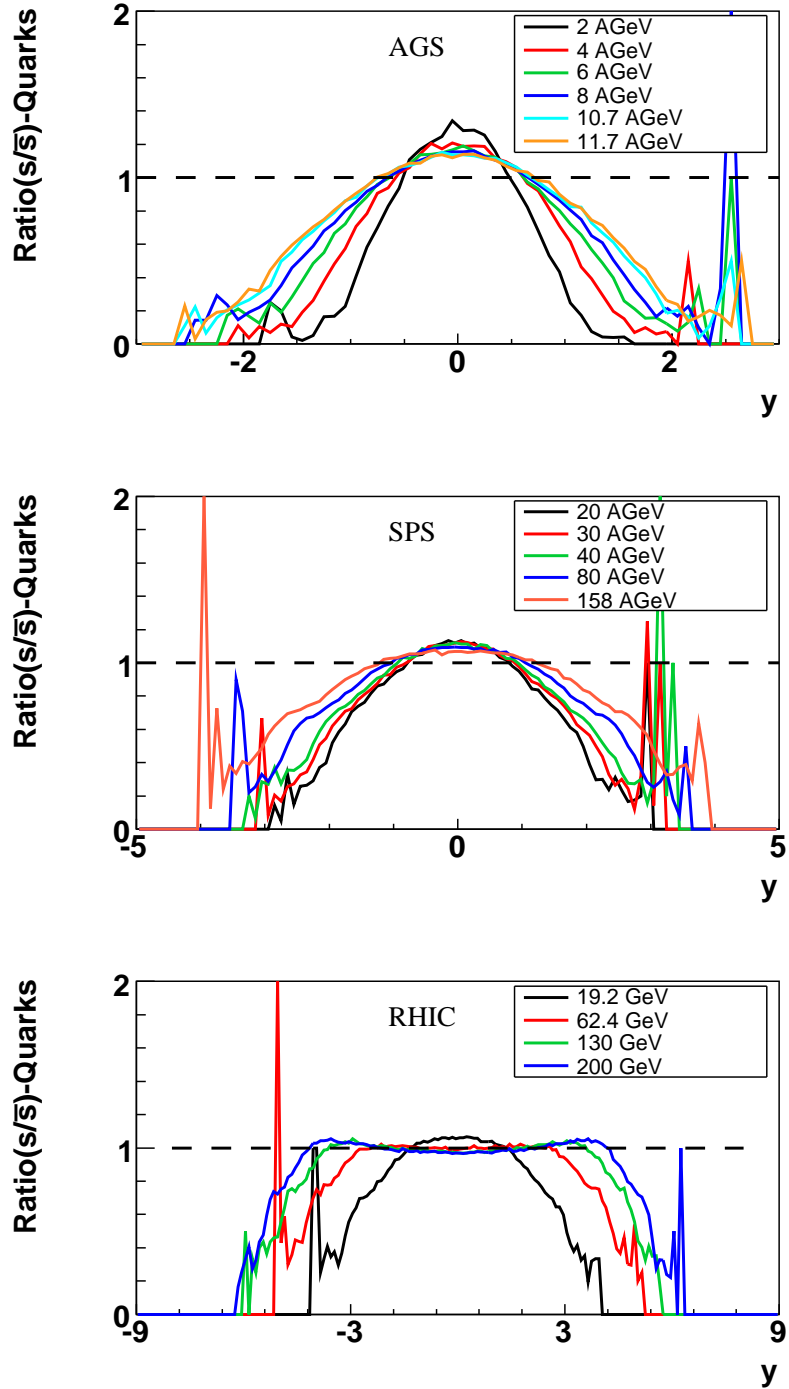


Figure 5.22: Rapidity dependence of the strange quark over anti-strange quark ( $s/\bar{s}$ ) ratio for central Pb+Pb/Au+Au reactions at AGS ( $E_{lab} = 2 - 11A$  GeV), SPS ( $E_{lab} = 20 - 158A$  GeV) and RHIC ( $\sqrt{s_{NN}} = 19 - 200$  GeV) energies.

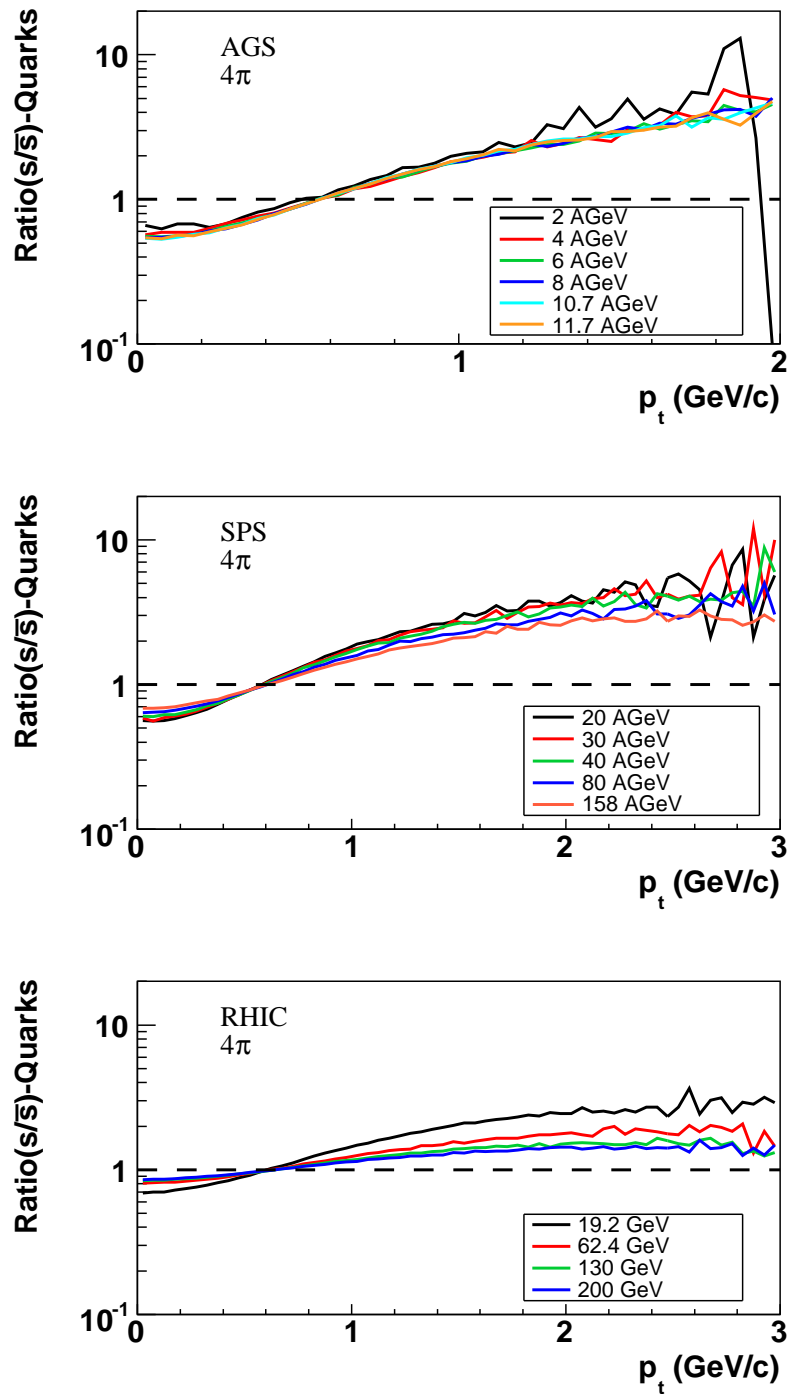


Figure 5.23: Transverse momentum dependence of the strange quark over anti-strange quark ( $s/\bar{s}$ ) ratio for central Pb+Pb/Au+Au reactions at AGS ( $E_{lab} = 2 - 11A$  GeV), SPS ( $E_{lab} = 20 - 158A$  GeV) and RHIC ( $\sqrt{s_{NN}} = 19 - 200$  GeV) energies.

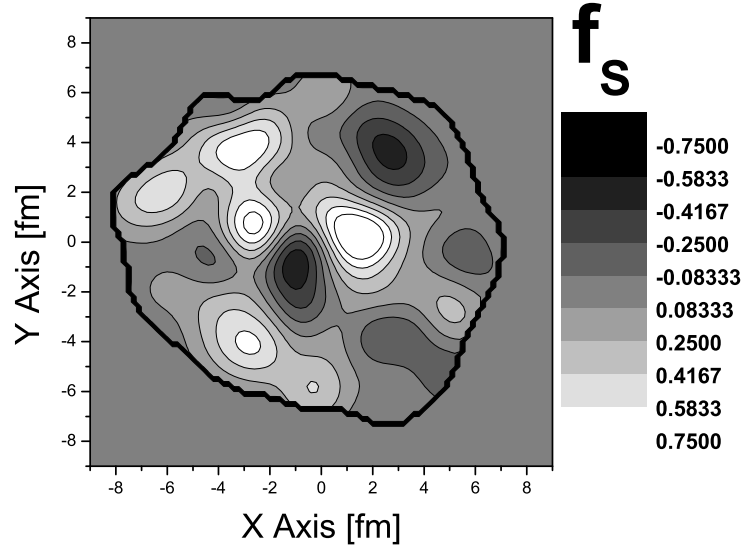


Figure 5.24: Fluctuations of the strangeness fraction  $f_s = \rho_s/\rho_B$  in the central plane (x is in the impact parameter direction, y is transversal to the impact parameter and longitudinal direction) for a single central Pb+Pb reaction at  $E_{lab} = 30A$  GeV. The color coding indicates the local strangeness fraction, dark regions have more anti-strange than strange quarks.

Next, we turn to the distribution and fluctuations of strangeness in coordinate space. Figure (5.24) elucidates the fluctuations of the strangeness fraction  $f_s = \rho_s/\rho_B$ , with  $\rho_B$  being the local baryon density and  $\rho_s$  being the local net-strangeness density, in the central plane for a single central Pb+Pb reaction at  $E_{lab} = 30A$  GeV. Here x is in the impact parameter direction and y is transversal to the impact parameter and longitudinal direction. The distribution of the net-strangeness and baryon densities were obtained from the UrQMD model by means similar to creating the hydro initial state in the hybrid model. All hadrons and their baryon number and strangeness content are represented by a Gaussian with a finite width of 1 fm [67, 264]. The plot is shown for the time when both nuclei have passed each other. The color coding indicates the local strangeness fraction, white regions have more strange than anti-strange quarks, while dark and black regions show more anti-strange quarks. Locally strangeness lumps of  $4 \text{ fm}^2 \times \Delta z$  appear both in positive and negative strangeness directions. As for the distribution in momentum space discussed above, also the coordinate space distribution is largely non-uniform, although these spacial fluctuations occur only on an event-by-event basis.

### 5.2.2 From the spectator region

In the previous section we have discussed the production of hypernuclei in the very hot and dense region of the fireball, created in a heavy ion collision. It was shown how many hypernuclei can be created from the manifold reaction products of the collision.

In this section we will discuss a different method of hypernuclei production in collisions of heavy ions. In particular we will discuss the absorption of  $\Lambda$  particles in the projectile spectator fragment. The projectile fragment is the remnant, composed of all nuclei which have not undergone a reaction and continue flying in the beam direction. This excited remnant is usually highly unstable and decays into several fragments.

Before it decays though there is the possibility that a (multi-)strange baryon, produced in the fireball, is absorbed in the projectile fragment. As the rapidity distributions from produced particles usually shows Gaussian tails, there is a finite possibility that such a particle appears in the rapidity bin of the projectile.

For a particle to be absorbed having the same rapidity as the projectile fragment is not sufficient. The hadron has to be spatially located inside or very close to the fragment and furthermore has to have a relative kinetic energy which is smaller than the binding energy of the hadron.

In the following we will estimate the number of  $\Lambda$ 's and  $\Xi$ 's which are absorbed in the projectile fragment of a Au+Au collision at a beam energy of  $E_{lab} = 20A$  GeV and with an impact parameter of  $b = 8.0$ . For this we will apply the UrQMD model in its cascade version (see section (3.1)). The absorption of strange particles can reasonably assumed only at a time after the two nuclei have passed through each other. After this point we will check for all  $\Lambda$ 's and  $\Xi$ 's in time steps of  $\Delta t = 0.5$  fm/c, first selecting only particles which are in a rapidity interval of  $y_b \pm \Delta y$ , where  $y_b = 1.9$  is the beam rapidity and  $\Delta y = 0.267$  the rapidity shift contributed to possible Fermi momenta of the nucleons in the nucleus.

For such particles the net baryon density in the local rest frame of the strange particle is then calculated. This is done by calculating the zero component of the net baryon number current of all baryons within the same rapidity bin. For this purpose we assume that each baryon is represented by a Gaussian package of width  $\sigma = 1$  fm which is Lorentz contracted in the z-direction.

The binding energy of the  $\Lambda$  and, for simplicity, for the  $\Xi$  is then assumed to be [276]:

$$E_{bind} = 0.383\rho_b(1 - 1.85\rho_0^{2/3})\text{MeV} \quad (5.5)$$

where  $\rho_0 \approx 0.16\text{fm}^{-3}$  is the nuclear ground state density. Finally we calculate the kinetic energy of the strange particle with respect to the rest frame of the projectile nucleus. Whenever this energy is less than its corresponding binding energy, calculated with eq. (5.5), the particle is absorbed and we remove it from the cascade simulation. We have

checked that our results do not depend strongly on the value of the binding energy (when it is varied in a reasonable interval,  $E_{bind}(\rho_0) \pm 20\%$ )

Following the above procedure we have sampled 200,000 events resulting in the following predictions for the absorption of  $\Lambda$ 's and  $\Xi$ 's:

Particle	Rate per event
$\Lambda$	0.0228
$\Xi$	$\approx 0.0002$

Table 5.2: Rate of absorbed strange baryons

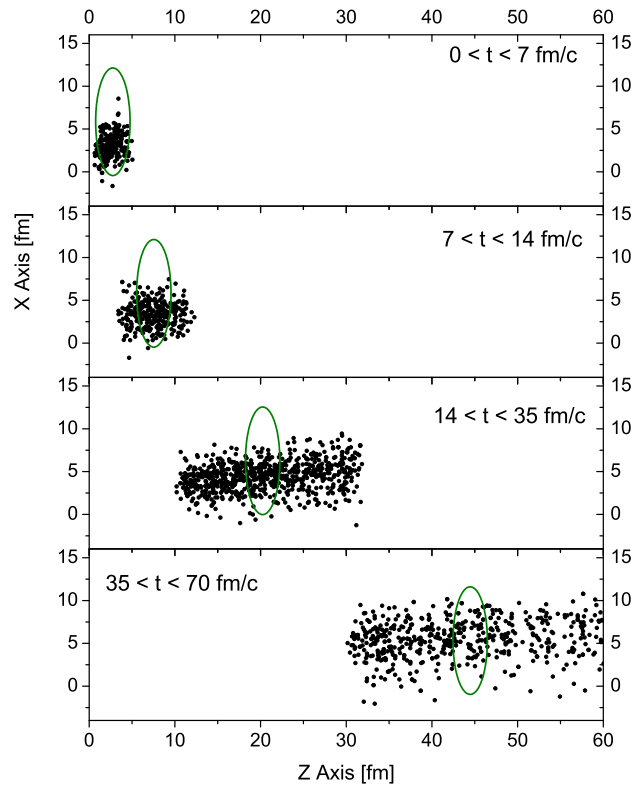


Figure 5.25: Distribution of the absorbed  $\Lambda$ 's in the X-Z-plane. Every point corresponds to one  $\Lambda$  absorbed in the projectile spectator fragment. For symmetric systems the absorption in the target spectator should also be symmetric with respect to the Y-axis.

Since we use the UrQMD model for our analysis we can also extract detailed information of the particles which are absorbed. Figure (5.25) depicts the time and x-positions of all  $\Lambda$ 's absorbed in the projectile spectators in 200,000 events. As one can see the absorption may take place over a rather long time interval. In the beginning mostly  $\Lambda$ 's close to the reaction zone (small x values) are absorbed, while later on particles can be absorbed at any point in the projectile fragment.

Figure (5.26) shows the transverse distribution of the absorbed  $\Lambda$ 's together with the contours of the two colliding nuclei. This figure shows that in fact most strange particles are absorbed in the spectator region.

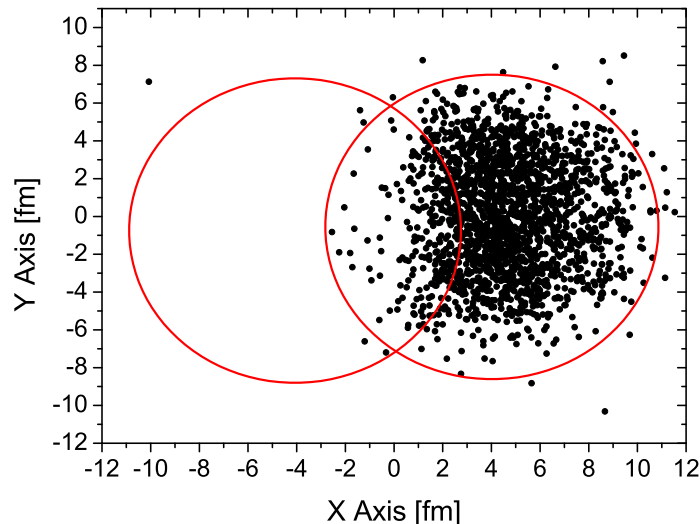


Figure 5.26: Distribution of the absorbed  $\Lambda$ 's in the transverse-plane. Every point corresponds to one  $\Lambda$  absorbed in the projectile spectator fragment.

Finally, Figure (5.27) shows the normalized momentum (left) and transverse momentum (right) distributions for the absorbed  $\Lambda$ 's. Here one can observe that even particles that have momenta larger than the binding energy can be absorbed as the relevant quantity is not the momentum but rather the kinetic energy and the strength of the binding in the projectile fragment.

These results indicate that in fact the production of hypernuclei via capture of  $\Lambda$ 's can be a promising perspective at the future FAIR facility. Even more intriguing is the possibility of absorbing the multi strange  $\Xi$  baryon which could result in the production of a double strange hypernucleus. This could prove valuable as the  $\Xi$ -hypernucleus is still not well understood due to very few events measured.



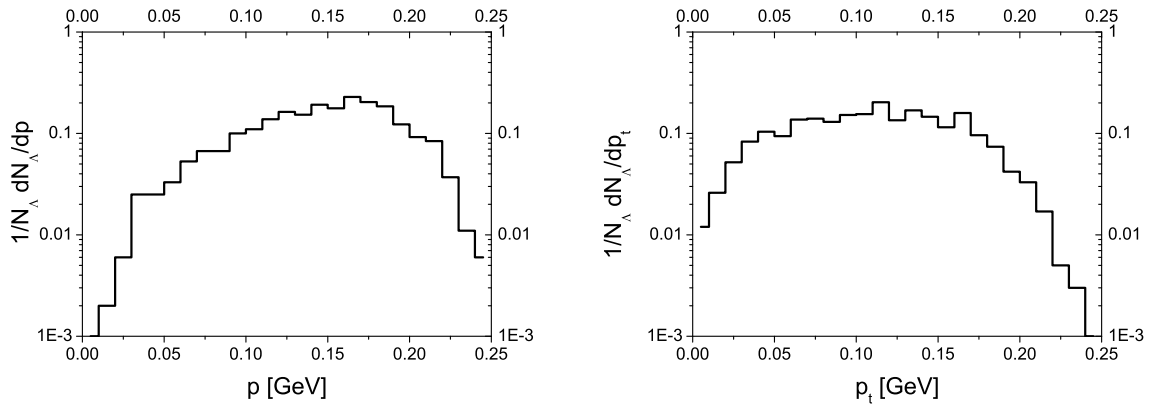


Figure 5.27: Left: Momentum distribution of the absorbed  $\Lambda$ 's.  
Right: Transverse momentum distribution of the absorbed  $\Lambda$ 's.



# Chapter 6

## Summary

The main aim of this work was to develop an effective equation of state for QCD, having the correct asymptotic degrees of freedom, to be used as input for dynamical studies of heavy ion collisions. The fundamental concepts and properties of elementary matter and the strong interaction were reviewed in short. For very hot or dense systems of nuclear matter, the appearance of chiral symmetry and deconfinement are the most interesting theoretical concepts to be dealt with. As low energy QCD cannot be solved analytically, effective models of the strong interaction focus on reproducing these most prominent features of the theory. Especially bulk matter properties of hot and dense nuclear matter can be characterized with thermodynamic variables and the phase diagram of QCD.

The first focus in this work is on the low energy limit of quantum chromodynamics, e.g. the hadronic sector. Here a multitude of identified particles and their resonances exist. Therefore we introduced the hadron resonance gas as the most basic effective low energy model of QCD. As free quarks are expected to exist in the high temperature limit they have to be introduced at some point in any hadronic model. In the HRG this can only be done via a Maxwell construction leading to a very strong first order phase transition between hadrons and quarks. As we now know from calculations, where a QCD (like) theory is solved on a space-time lattice, the chiral and deconfinement phase transitions, at least at zero baryon number density, are a smooth crossover. Therefore one has to introduce a model where both asymptotic degrees of freedom are included in a single partition function. We presented such an approach for modeling an EoS that respects the symmetries underlying QCD, and includes the correct asymptotic degrees of freedom, i.e. quarks and gluons at high temperature and hadrons in the low-temperature limit. We achieve this by including quarks degrees of freedom and the thermal contribution of the Polyakov loop in a hadronic chiral sigma-omega model.

The hadronic part of the model is a nonlinear realization of an sigma-omega model. As the fundamental symmetries of QCD should also be present in its hadronic states such an approach is widely used to describe hadron properties below and around  $T_c$ . Our hadronic model gives a good description of hadron vacuum properties like masses, as well as sat-

urated nuclear matter properties, like the binding energy of the nucleon or the  $\Lambda$ . The quarks are introduced as thermal quasi particles, coupling to the Polyakov loop, while the dynamics of the Polyakov loop are controlled by a potential term which is fitted to reproduce pure gauge lattice data. In this model the sigma field serves as the order parameter for chiral restoration and the Polyakov loop as order parameter for deconfinement. The hadrons are suppressed at high densities by excluded volume corrections. Nevertheless, we observe a substantial hadronic contribution to the EoS up to temperatures of 2 times  $T_c$ .

We showed that the properties of the EoS are in qualitative agreement with lattice data at  $\mu_B = 0$ . Various quantities, like the pressure and energy density, are in good agreement with lattice data. Deviations from lattice results can be explained by the hadronic contributions and volume corrections. In spite of a continuous phase transition, we obtain a considerably smaller value for the speed of sound around  $T_c$  ( $c_s^2 \approx 0.07$ ) when compared to lattice calculations [174]. At finite baryon density, the transition from deconfined to confined matter proceeds as a smooth crossover for all values of  $\mu_B$ . The same is true for the chiral phase transition (except the liquid gas phase transition, which is of first order at very low temperatures). At high chemical potentials and low temperatures we find a very interesting phase structure. In this region chiral symmetry is partially restored, while deconfinement is not yet realized, thus creating an exotic form of matter.

Furthermore we compared results for the quark number susceptibilities at  $\mu_B = 0$  obtained from our hadron-quark model and the purely quark PNJL model to recent results from lattice calculations. Both models strongly indicate that the EoS of QCD above  $T_c$  seems to be composed purely of a gas of non-interacting quasi particles. This finding is in agreement with recent work by [274] where the extracted quark vector coupling strength approaches zero very fast around  $T_c$ . On the other hand, lattice observables like the interaction measure and the normalized Polyakov loop indicate a large region above the critical temperature where the hot QCD medium is far from being an ideal gas. Around  $T_c$  repulsive hadronic interactions are supported by our results with the QH model. To describe the steep increase of  $c_2$  around  $T_c$  we need to introduce hadronic contributions up to right above  $T_c$ . At even larger temperature the hadrons seem to be replaced by a almost non interacting gas of quarks. This offers an intriguing implication concerning the CeP. The phase structure of QCD up to  $T_c$ , and likely even slightly above it, could be determined by hadronic interactions. A repulsive hadronic vector interaction, which is required in order to reproduce the properties of a saturated nuclear ground state, may move the CeP to larger chemical potentials or even remove it completely from the phase diagram which would be in accordance to recent lattice results and mean field investigations [275, 148, 274].

One hope of performing high energy heavy ion collisions is to find observables which are sensitive on the EoS of QCD or even only on some aspects as for example deconfinement, chiral symmetry restoration and a possible critical endpoint. For this purpose one has to make model studies to try to disentangle the dynamics of such a rather complicated many body system. In the recent years the development of fluid dynamic or hybrid models has

become very popular, as fluid dynamics allows for the inclusion of any phenomenological EoS in a very simple way. Therefore, as a next step, we introduced our new HQ model equation of state in a microscopic+macroscopic hybrid approach to heavy ion collisions.

This hybrid approach is based on the Ultra-relativistic Quantum Molecular Dynamics (UrQMD) transport approach with an intermediate hydrodynamical evolution for the hot and dense stage of the collision. The specific coupling procedure including the initial conditions and the freeze-out prescription have been explained. The present implementation allows to compare pure microscopic transport calculations with hydrodynamic calculations using exactly the same initial conditions and freeze-out procedure.

The effects of the change in the underlying dynamics - ideal fluid dynamics vs. non-equilibrium transport theory - have been explored. The final pion and proton multiplicities are lower in the hybrid model calculation due to the isentropic hydrodynamic expansion while the yields for strange particles are enhanced due to the local equilibrium in the hydrodynamic evolution. This leads to a reasonable description of most strange particle data including the famous 'horn' like structure in the  $K^+/\pi^+$  ratio.

We also investigated the dependence of the results on a change of the freeze-out prescription. It was observed that the different freeze-out procedures have almost as much influence on the mean transverse mass excitation function as the EoS. A comparison to the available data suggests that a gradual transition from hydrodynamics to the transport simulation at an energy density of  $4-5\epsilon_0$  provides the best description of the data. The experimentally observed step-like behavior of the mean transverse mass excitation function is only reproduced, if a first order phase transition with a large latent heat is applied or the EoS is effectively softened due to non-equilibrium effects in the hadronic transport calculation. The elliptic and directed flow have been shown to be not sensitive to changes in the EoS while the smaller mean free path in the hydrodynamic evolution reflects directly in higher flow results which are consistent with the experimental data. This finding indicates qualitatively that physical mechanisms like viscosity and other non equilibrium effects play an essentially more important role than the EoS when bulk observables like flow are investigated.

Although these results seem disappointing, as no real bulk matter signal for a phase transition could be identified, there are new results where the hybrid model is used, in connection with the QH EoS, to model the production of direct photons [277, 278, 279] and di-leptons [280] from heavy ion collisions. These results indicate that at least the presence of quasi-free quarks is necessary to explain the measured photon and di-lepton yields.

In the last chapter, results for the thermal production of MEMOs in nucleus-nucleus collisions from a combined micro+macro approach were presented. Multiplicities, rapidity and transverse momentum spectra are predicted for Pb+Pb interaction at  $E_{lab} = 5A$  GeV and  $E_{lab} = 30A$  GeV. The presented excitation functions for various MEMO multiplicities

show a clear maximum at the upper FAIR energy regime making this facility the ideal place to study the production of these exotic forms of multistrange objects. Detector simulations have shown that the CBM experiment is well suited for the search of exotic multihypernuclear objects either by invariant mass reconstruction of strange di-baryons or observing decay systematics (The very stable double negative  $\{2\Xi^0, 2\Xi^-\}$  for example should have a characteristic decay in two negatively charged particles)[250].

For the interesting region of anti-hypernuclei the upcoming experiments at the LHC will provide an abundant source of thermally produced anti-clusters with and without strangeness, exploring even deeper into the yet unknown nuclear chart of anti-(hyper)matter.

Compared to many previous studies on MEMO and strangelet production, based on statistical models with global strangeness and baryon number conservation, the present approach indicates that the local strangeness density clumps strongly in coordinate space and that strangeness is unevenly distributed in momentum space. This mechanism does not require the production of a deconfined state, and profits from the non-equilibrium features present in the reaction. These fluctuations might lead to an enhancement of MEMO (and strangelet) production compared to previous calculations. The net strangeness at midrapidity deviates from zero - not only on an event-by-event basis - indicating that the assumption of local strangeness neutralization is only justified at the RHIC energy regime, but not at lower energies. Here it is therefore questionable if midrapidity particle ratios can be used as input for thermal particle multiplicity calculations.

Instead of producing hypernuclei in the fireball of a heavy ion collision we highlight a different mechanism in the last section of this work. Here the hypernuclei are created due to absorption of  $\Lambda$ 's and  $\Xi$ 's in the projectile fragment region. Using the UrQMD transport model we make assumptions on how many hyperons one could expect to be absorbed in heavy ion collisions at  $E_{\text{Lab}} = 20\text{A GeV}$ . In addition we also provide space time and momentum space information on the absorbed hyperons.

## 6.1 Outlook

Based on the presented work one can easily continue to improve one the different aspects of this work. As lattice calculations become more and more sophisticated they yield more and new results which have yet to be explained with effective models. Quite recently it has become clear that there seems to be a distinct separation between the chiral and deconfinement phase transition. This puts again the hadronic part of the QCD equation of state, and their effect on the order parameters and thermodynamics, into the focus of attention. A straight forward approach would therefore be to include also a full hadronic resonance spectrum in the chiral hadronic model. On the other hand also the basic ingredients of the model can be revisited to obtain an even better description of lattice data.

For the hybrid model there seem to exist also various points at where to improve on. Interesting effects, like a core-corona separation, for the initial state may be taken into account. But also the hydrodynamic evolution itself can be improved on by the introduction of a viscous fluid dynamical code. Even more the treatment of the freeze out is yet still not yet settled and may be improved upon by a more consistent definition of the transition hypersurface. The introduction of a fluid dynamical description in rapidity coordinates could also enable us to make predictions for the highest energies reached in heavy ion (and proton proton) collision at the LHC.

Note that the observation of particle multiplicity fluctuations and their kurtosis have become the focus of attention concerning the search of the critical endpoint [49, 47, 226, 227]. But as has been pointed out in [228] fluctuations can be very sensitive on the correct treatment of conserved quantum numbers like baryon number charge and strangeness on an event-by-event basis. It is certainly possible, and planned, to analyze these kind of event-by-event fluctuations in the current hybrid-model. The computational effort for such studies however, is much greater than for bulk observables and we therefore restricted our present study on non event-by-event observables.





# Appendix A

## Effective chiral models

### A.1 The linear sigma model

In the following we will introduce a very instructive example of an effective (phenomenological) model for QCD. The linear  $SU(2) \times SU(2)$   $\sigma$  model [281, 282]. Though being a rather simple model it already contains many properties of QCD. The linear sigma model is an hadronic model. In this sense it is a low energy model for QCD and in the following  $\Psi$  will denote the nucleon wave function .

The model Lagrangean reads:

$$\mathcal{L}_{LSM} = \bar{\Psi}i\partial_\mu\gamma_\mu\Psi + \frac{1}{2}\partial_\mu\vec{\pi}\partial^\mu\vec{\pi} + \frac{1}{2}\partial_\mu\sigma\partial^\mu\sigma - g\bar{\Psi}(\sigma + i\vec{\tau}\vec{\pi}\gamma_5)\Psi + V_{SSB} \quad (\text{A.1})$$

where  $V_{SSB}$  is a potential term which spontaneously breaks the chiral symmetry of the Lagrangean:

$$V_{SSB} = V(\sigma^2 + \pi^2) = \frac{\mu^2}{2}(\sigma^2 + \pi^2) + -\frac{\lambda}{4}(\sigma^2 + \pi^2)^2 \quad (\text{A.2})$$

This potential is also called the Mexican-Hat potential (see figure A.1). It is radially symmetric in the coordinates  $\sigma$  and  $\pi = \vec{\pi}$  and the energetically favorable states are on the outside of the hat. The term of the form  $(\sigma^2 + \pi^2)$  is called chiral invariant because a chiral transformation would not change the length of a vector in  $\sigma$  and  $\pi$  but rather rotate it which does not change the value of the potential. The parameter  $\mu^2$  has to be larger than 0 for spontaneous breaking of chiral symmetry to occur. The degenerate ground states then are defined by:

$$\sigma^2 + \pi^2 = v^2 \quad \text{with} \quad v = \sqrt{\frac{\mu^2}{\lambda}} \quad (\text{A.3})$$

One can now chose the vacuum expectation values to take the following values:

$$\langle 0|\pi|0\rangle = 0, \quad \langle 0|\sigma|0\rangle = \sqrt{\frac{\mu^2}{\lambda}} = v \quad (\text{A.4})$$

In this case, fluctuations of the pionic fields do not require any energy, therefore the pions are the Goldstone modes of the model. On the other hand the sigma and nucleons are rather massive even though the Lagrangian is still fully symmetric under a chiral transformation.

The nucleon mass in this model is then generated through coupling to the scalar field and its finite ground state expectation value. It is in agreement with QCD properties, as the explicit chiral symmetry breaking term in the QCD Lagrangean should be small. A corresponding term could also be included in the linear sigma model:

$$L_{esb} = m_\pi^2 f_\pi \sigma \quad (\text{A.5})$$

It gives the correct pion mass, as the potential now has a distinct minimum and breaks the symmetry with respect to the axial current.

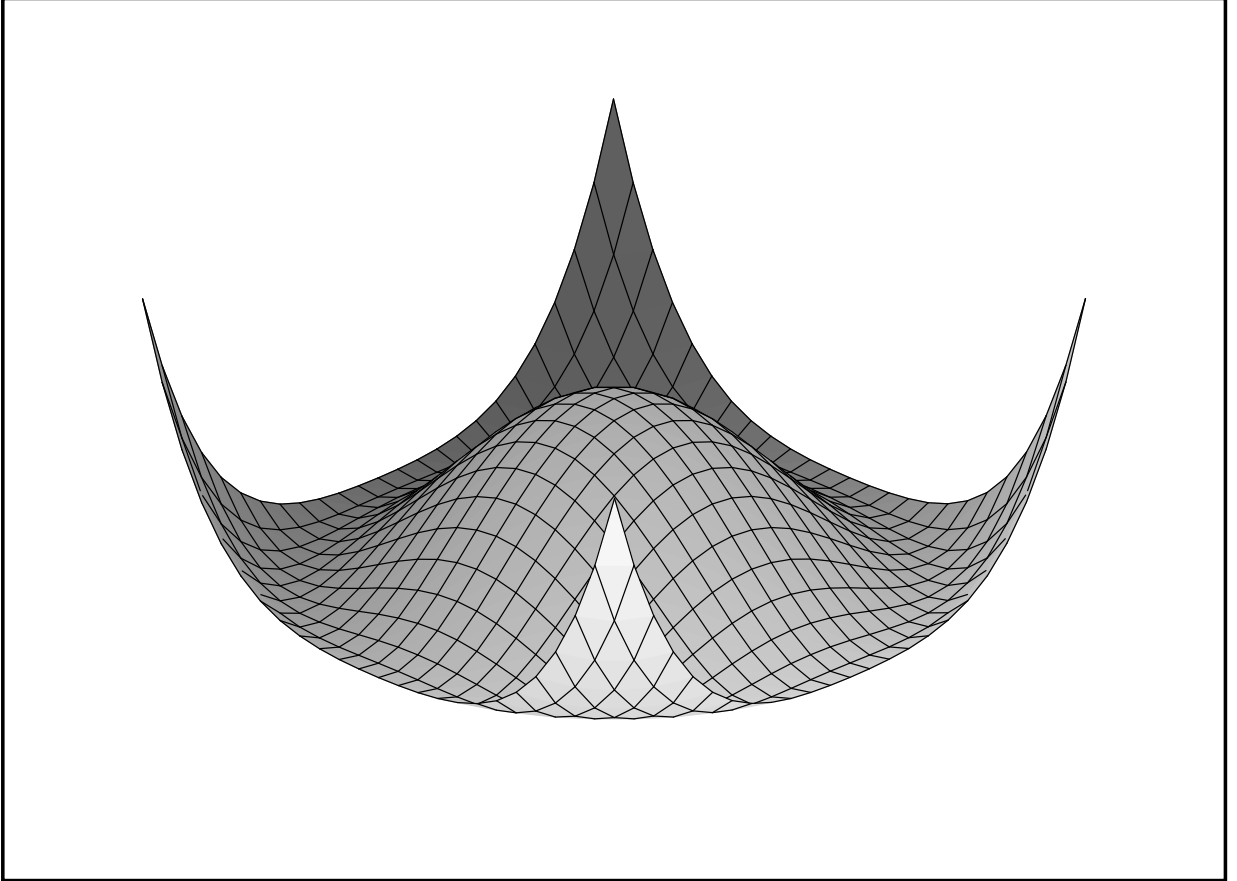


Figure A.1: Depiction of a Mexican-Hat Potentials in  $X(\sigma)$  and  $Y(\pi)$  coordinates.

## A.2 The nonlinear sigma model

Despite being very successful in describing several aspects of QCD, the linear sigma model has some shortcomings. One main problem of the model is the direct coupling of the pion field to the nucleons which leads to problems with the description of direct pion nucleon scattering data. In addition heavy particles do not exist in chiral multiplets.

To cure these main problems a "nonlinear representation" of the sigma model is used. One usually rewrites the chiral fields. As the chiral invariant corresponds to a radius in the chiral circle it is appropriate to use polar coordinates [283, 284] (for other advantages and a detailed introduction see [131]):

$$\begin{aligned} \mathcal{L}_{NLSM} &= \bar{N}(iD_\mu\gamma^\mu - \bar{A}_\mu\gamma^\mu\gamma_5 - g(v+S))N \\ &+ \frac{1}{2}\partial_\mu\vec{p}\partial^\mu\vec{p} + \frac{1}{2}\partial_\mu S\partial^\mu S - \frac{\mu^2}{2}(v+S)^2 - \frac{\lambda}{4}(v+S)^4 \end{aligned} \quad (\text{A.6})$$

where  $N = N_R + N_L = \xi^\dagger\Psi_R + \xi\Psi_L$  ( $\xi = \exp(i\vec{\tau}\vec{p}/2v)$ ) is the transformed nucleon wavefunction and  $D_\mu = \partial_\mu - \frac{1}{2}(\xi^\dagger\partial_\mu\xi + \xi\partial_\mu\xi^\dagger)$  is the modified derivative operator. The term  $(v+S)$  is defined by the transformation: wavefunction and  $D_\mu = \partial_\mu - \frac{1}{2}(\xi^\dagger\partial_\mu\xi + \xi\partial_\mu\xi^\dagger)$  is the modified derivative operator. The term  $(v+S)$  is defined by the transformation:

$$\sigma + i\vec{\tau}\vec{\pi} \equiv (v+S) \exp(i\vec{\tau}\vec{p}/v) \approx v + i\vec{\tau}\vec{p} \quad (\text{A.7})$$

$$(\sigma^2 + \vec{\pi}^2) = (v+S)^2 \quad (\text{A.8})$$

$v = \sigma_0$  is the expectation value of the scalar field,  $S$  and  $\vec{p}$  are the fluctuations of the  $\sigma$ - and  $\vec{\pi}$ -field.

In the NLSM the pions now do not couple directly to the nucleon anymore and these will therefore transform vectorial. This means that in the NLSM heavy particles can be included without spoiling invariance under chiral transformation.



# Appendix B

## Trace anomaly and scale invariance

In the limit of vanishing quark masses, the QCD-Lagrangean has no dimensional parameters and therefore is invariant under a scale transformation:

$$\psi(s) \rightarrow \lambda^{3/2}\psi(\lambda x), \quad A_\mu^a(x) \rightarrow \lambda A_\mu^a(\lambda x) \quad (\text{B.1})$$

with  $\lambda$  an arbitrary scale. This leads to a traceless energy momentum tensor  $\Theta^{\mu\nu}$ , with conserved dilaton current  $J_{\text{scale}}^\mu$

$$J_{\text{scale}}^\mu = x_\nu \Theta^{\mu\nu}, \quad \partial J_{\text{scale}}^\mu = \Theta^\mu_\nu = 0 \quad (\text{B.2})$$

this means one needs to specify a scale parameter [285, 286, 287, 288]. Taking into account quantum effects, the trace has a contribution from the gluons. furthermore a finite quark mass adds another term to the trace:

$$\Theta^\mu_\mu = \frac{\beta_{QCD}}{2g} G_{\mu\nu}^a G_a^{\mu\nu} + \sum_k \bar{\psi}_k \psi_k \quad (\text{B.3})$$

with  $\beta_{QCD}$  characterizing the rate at which the charge runs respect to the change in the scale:

$$\beta_{QCD}(g) = -\frac{g^3}{16\pi^2} \left(11 - \frac{2N_f}{3}\right) + \mathcal{O}(g^5) \quad (\text{B.4})$$

It has been shown that the Gluonic contribution can be identified with the gluon condensate [289, 290, 291, 292].

If an effective model contains terms where the parameters have a certain scale, this can be "fixed" by multiplying these terms with powers of  $\chi$  to assure scale invariance in the model.



# Appendix C

## Viscous fluid dynamics

The quantities evolved by fluid dynamics usually are the symmetric energy momentum tensor  $T^{\mu\nu}$  and a net charge current  $N^\mu = nu^\mu + \nu^\mu$  (e.g. the net baryon number current). The energy momentum tensor can be written as

$$T^{\mu\nu} = \epsilon u^\mu u^\nu - (p + \Pi)\Delta^{\mu\nu} + 2q^\mu u^\nu + \pi^{\mu\nu}. \quad (\text{C.1})$$

Here  $\epsilon$  is the energy density in the fluid rest frame,  $u^\mu$  is the normalized 4-velocity of the fluid,  $\Delta^{\mu\nu} = g^{\mu\nu} - u^\mu u^\nu$  denotes the projector onto the 3-space orthogonal to  $u^\mu$  and  $(p + \Pi)$  is the sum of the thermodynamic and the bulk viscous pressure.  $q^\mu$  denotes the heat flux current and  $\pi^{\mu\nu}$  is the shear stress tensor which has only five independent entries, as  $\pi^{\mu\nu}u_\mu = 0$ . The conservation equations for the currents and the energy momentum tensor are:

$$\partial_\mu N^\mu = 0 \text{ and } \partial_\mu T^{\mu\nu} = 0 \quad (\text{C.2})$$

These equations now contain 15 unknown variables:  $\epsilon$ ,  $p$ ,  $n$ ,  $\Pi$ ,  $\pi^{\mu\nu}$ ,  $\nu_\mu$  and  $q^\mu$ . One of these equations can be eliminated by assuming a specific equation of state ( $p = p(\epsilon, n)$ ). In the limit of ideal fluid dynamics all dissipative quantities vanish and one is left with 5 unknown which can be solved for using the set of equations (C.2).

Alternatively one can introduce equations to determine the dissipative quantities leading to first and second order theories of dissipative fluid dynamics. In the Navier-Stokes approximation, which is a first order theory, the dissipative variables are all expressed in terms of the non-dissipative variables. In the Israel-Stuart approach [293] the dissipative quantities are independent and their evolution is governed by differential equations. Usually the easier to solve first order theories yield unstable solutions [294], while solving second order theories numerically in more than 2 dimensions is a rather challenging task which still has to be fully resolved [295, 296, 297, 298, 299, 300, 106, 301, 302, 303, 304].





# Bibliography

- [1] Noether, E.: Invarianten beliebiger Differentialausdrücke. Gött. Nachr. 1918, 37-44 (1918)
- [2] <http://www.gsi.de/fair/experiments/CBM/Phasendiagram.jpg>
- [3] B. R. Schlei, Image and Vision Computing **27**, Issue 6 (2009), Pages 637-647
- [4] F.J. Dyson and N.H. Xuong, Phys. Rev. Lett. **13** (1964) 815.
- [5] International Symposium on Strangeness in Quark Matter 1998, J. Phys. G **25**, 1 (1999).
- [6] The STAR collaboration, Science Vol. **328**. no. 5974, pp. 58 - 62, April 2010,
- [7] J. Steinheimer, V. Dexheimer, H. Petersen *et al.*, Phys. Rev. **C81**, 044913 (2010). [arXiv:0905.3099 [hep-ph]].
- [8] H. Petersen, J. Steinheimer, G. Burau *et al.*, Eur. Phys. J. **C62**, 31-36 (2009).
- [9] J. Steinheimer, H. Stoecker, I. Augustin *et al.*, Prog. Part. Nucl. Phys. **62**, 313-317 (2009).
- [10] H. Petersen, J. Steinheimer, G. Burau *et al.*, Nucl. Phys. **A830**, 283C-286C (2009). [arXiv:0907.2169 [nucl-th]].
- [11] J. Steinheimer, H. Petersen, G. Burau *et al.*, Acta Phys. Polon. **B40**, 999-1004 (2009).
- [12] J. Steinheimer, S. Schramm, H. Stoecker, accepted for publication in J. Phys. G
- [13] J. Steinheimer, S. Schramm, to be published in Phys. Lett. B
- [14] T. Nakamura *et al.*, *In the Proceedings of 1st International Particle Accelerator Conference: IPAC'10, Kyoto, Japan, 23-28 May 2010, pp THOBRA02.*
- [15] D. J. Gross and F. Wilczek, Phys. Rev. D **8**, 3633 (1973).
- [16] D. J. Gross and F. Wilczek, Phys. Rev. Lett. **30**, 1343 (1973).

- [17] H. D. Politzer, Phys. Rev. Lett. **30**, 1346 (1973).
- [18] D. Weingarten, Phys. Rev. Lett. **51**, 1830 (1983).
- [19] C. Vafa, E. Witten, Nucl. Phys. **B234** (1984) 173.
- [20] J. Goldstone, Nuovo Cim. **19**, 154-164 (1961).
- [21] O. Kaczmarek and F. Zantow, Phys. Rev. D **71**, 114510 (2005) [arXiv:hep-lat/0503017].
- [22] A. M. Polyakov, Phys. Lett. B **72**, 477 (1978).
- [23] A. Roberge and N. Weiss, Nucl. Phys. B **275**, 734 (1986).
- [24] J. W. Harris and B. Muller, Ann. Rev. Nucl. Part. Sci. **46**, 71 (1996) [arXiv:hep-ph/9602235].
- [25] S. A. Bass, M. Gyulassy, H. Stoecker and W. Greiner, J. Phys. G **25**, R1 (1999) [arXiv:hep-ph/9810281].
- [26] P. Senger *et al.* [KaoS Collaboration], Nucl. Instrum. Meth. A **327**, 393 (1993).
- [27] A. Andronic *et al.* [FOPI Collaboration], Phys. Lett. B **612**, 173 (2005) [arXiv:nucl-ex/0411024].
- [28] G. Agakichiev *et al.* [HADES Collaboration], Phys. Rev. Lett. **98**, 052302 (2007) [arXiv:nucl-ex/0608031].
- [29] C. Pinkenburg *et al.* [E895 Collaboration], Phys. Rev. Lett. **83**, 1295 (1999) [arXiv:nucl-ex/9903010].
- [30] L. Ahle *et al.* [E866 Collaboration and E917 Collaborations], Phys. Lett. B **490**, 53 (2000) [arXiv:nucl-ex/0008010].
- [31] J. B. Elliott *et al.* [EOS Collaboration], Phys. Rev. C **67**, 024609 (2003) [arXiv:nucl-ex/0205004].
- [32] D. Adamova *et al.* [CERES Collaboration], Phys. Rev. Lett. **90**, 022301 (2003) [arXiv:nucl-ex/0207008].
- [33] C. Alt *et al.* [NA49 Collaboration], Phys. Rev. Lett. **94**, 052301 (2005) [arXiv:nucl-ex/0406031].
- [34] C. Alt *et al.* [NA49 Collaboration], Phys. Rev. Lett. **94**, 192301 (2005) [arXiv:nucl-ex/0409004].
- [35] C. Alt *et al.* [NA49 Collaboration], Phys. Rev. Lett. **92**, 042003 (2004) [arXiv:hep-ex/0310014].

- [36] C. Alt *et al.* [NA49 Collaboration], Phys. Rev. C **68**, 034903 (2003) [arXiv:nucl-ex/0303001].
- [37] C. Alt *et al.* [NA49 Collaboration], Phys. Rev. C **77**, 024903 (2008) [arXiv:0710.0118 [nucl-ex]].
- [38] R. Arnaldi *et al.* [NA60 Collaboration], Phys. Rev. Lett. **96**, 162302 (2006) [arXiv:nucl-ex/0605007].
- [39] J. Adams *et al.* [STAR Collaboration], Nucl. Phys. A **757**, 102 (2005) [arXiv:nucl-ex/0501009].
- [40] B. B. Back *et al.*, Nucl. Phys. A **757**, 28 (2005) [arXiv:nucl-ex/0410022].
- [41] I. Arsene *et al.* [BRAHMS Collaboration], Nucl. Phys. A **757**, 1 (2005) [arXiv:nucl-ex/0410020].
- [42] K. Adcox *et al.* [PHENIX Collaboration], Nucl. Phys. A **757**, 184 (2005) [arXiv:nucl-ex/0410003].
- [43] M. Gyulassy and L. McLerran, Nucl. Phys. A **750**, 30 (2005) [arXiv:nucl-th/0405013].
- [44] Z. Fodor and S. D. Katz, JHEP **0203**, 014 (2002) [arXiv:hep-lat/0106002].
- [45] Z. Fodor, S. D. Katz and C. Schmidt, JHEP **0703**, 121 (2007) [arXiv:hep-lat/0701022].
- [46] F. Karsch, J. Phys. G **31**, S633 (2005) [arXiv:hep-lat/0412038].
- [47] M. A. Stephanov, K. Rajagopal and E. V. Shuryak, Phys. Rev. Lett. **81**, 4816 (1998) [arXiv:hep-ph/9806219].
- [48] M. Gazdzicki and M. I. Gorenstein, Acta Phys. Polon. B **30**, 2705 (1999) [arXiv:hep-ph/9803462].
- [49] M. A. Stephanov, K. Rajagopal and E. V. Shuryak, Phys. Rev. D **60**, 114028 (1999) [arXiv:hep-ph/9903292].
- [50] L. V. Bravina *et al.*, Phys. Rev. C **60**, 024904 (1999) [arXiv:hep-ph/9906548].
- [51] L. V. Bravina *et al.*, Phys. Rev. C **63**, 064902 (2001) [arXiv:hep-ph/0010172].
- [52] M. Gazdzicki *et al.* [NA49 Collaboration], J. Phys. G **30**, S701 (2004) [arXiv:nucl-ex/0403023].
- [53] I. C. Arsene *et al.*, Phys. Rev. C **75**, 034902 (2007) [arXiv:nucl-th/0609042].

- [54] J. Theis, G. Graebner, G. Buchwald, J. A. Maruhn, W. Greiner, H. Stoecker and J. Polonyi, Phys. Rev. D **28**, 2286 (1983).
- [55] D. Molnar and P. Huovinen, Phys. Rev. Lett. **94**, 012302 (2005) [arXiv:nucl-th/0404065].
- [56] Z. Xu and C. Greiner, Phys. Rev. C **71**, 064901 (2005) [arXiv:hep-ph/0406278].
- [57] G. Bureau, J. Bleibel, C. Fuchs, A. Faessler, L. V. Bravina and E. E. Zabrodin, Phys. Rev. C **71**, 054905 (2005) [arXiv:nucl-th/0411117].
- [58] S. Paiva, Y. Hama and T. Kodama, Phys. Rev. C **55**, 1455 (1997).
- [59] C. E. Aguiar, Y. Hama, T. Kodama and T. Osada, Nucl. Phys. A **698**, 639 (2002) [arXiv:hep-ph/0106266].
- [60] O. . J. Socolowski, F. Grassi, Y. Hama and T. Kodama, Phys. Rev. Lett. **93**, 182301 (2004) [arXiv:hep-ph/0405181].
- [61] F. Grassi, Y. Hama, O. Socolowski and T. Kodama, J. Phys. G **31**, S1041 (2005).
- [62] R. Andrade, F. Grassi, Y. Hama, T. Kodama, O. . J. Socolowski and B. Tavares, Eur. Phys. J. A **29**, 23 (2006) [arXiv:nucl-th/0511021].
- [63] R. Andrade, F. Grassi, Y. Hama, T. Kodama and O. . J. Socolowski, Phys. Rev. Lett. **97**, 202302 (2006) [arXiv:nucl-th/0608067].
- [64] C. E. Aguiar, T. Kodama, T. Koide and Y. Hama, Braz. J. Phys. **37**, 95 (2007).
- [65] S. A. Bass *et al.*, Prog. Part. Nucl. Phys. **41**, 255 (1998) [Prog. Part. Nucl. Phys. **41**, 225 (1998)] [arXiv:nucl-th/9803035].
- [66] M. Bleicher *et al.*, J. Phys. G **25**, 1859 (1999) [arXiv:hep-ph/9909407].
- [67] J. Steinheimer, M. Bleicher, H. Petersen, S. Schramm, H. Stoecker and D. Zschesche, Phys. Rev. C **77**, 034901 (2008) [arXiv:0710.0332 [nucl-th]].
- [68] B. Andersson, G. Gustafson and B. Nilsson-Almqvist, Nucl. Phys. B **281**, 289 (1987).
- [69] B. Nilsson-Almqvist and E. Stenlund, Comput. Phys. Commun. **43**, 387 (1987).
- [70] T. Sjostrand, Comput. Phys. Commun. **82**, 74 (1994).
- [71] M. Belkacem *et al.*, Phys. Rev. C **58**, 1727 (1998) [arXiv:nucl-th/9804058].
- [72] L. V. Bravina *et al.*, Phys. Rev. C **78**, 014907 (2008) [arXiv:0804.1484 [hep-ph]].

- [73] H. J. Drescher, M. Bleicher, S. Soff and H. Stoecker, *Astropart. Phys.* **21**, 87 (2004) [arXiv:astro-ph/0307453].
- [74] H. J. Drescher, G. R. Farrar, M. Bleicher, M. Reiter, S. Soff and H. Stoecker, arXiv:astro-ph/0305429.
- [75] S. A. Bass, M. Hofmann, M. Bleicher, L. Bravina, E. Zabrodin, H. Stoecker and W. Greiner, *Phys. Rev. C* **60**, 021901 (1999) [arXiv:nucl-th/9902055].
- [76] S. A. Bass and A. Dumitru, *Phys. Rev. C* **61**, 064909 (2000) [arXiv:nucl-th/0001033].
- [77] S. Soff, S. A. Bass and A. Dumitru, *Phys. Rev. Lett.* **86**, 3981 (2001) [arXiv:nucl-th/0012085].
- [78] M. Bleicher *et al.*, *Phys. Rev. Lett.* **88**, 202501 (2002) [arXiv:hep-ph/0111187].
- [79] A. Dumitru, S. A. Bass, M. Bleicher, H. Stoecker and W. Greiner, *Phys. Lett. B* **460**, 411 (1999) [arXiv:nucl-th/9901046].
- [80] G. Zeeb, M. Reiter and M. Bleicher, *Phys. Lett. B* **586**, 297 (2004) [arXiv:nucl-th/0312015].
- [81] C. Nonaka and S. A. Bass, *Nucl. Phys. A* **774**, 873 (2006) [arXiv:nucl-th/0510038].
- [82] C. Nonaka and S. A. Bass, *Phys. Rev. C* **75**, 014902 (2007) [arXiv:nucl-th/0607018].
- [83] S. A. Bass *et al.*, *Nucl. Phys. A* **661**, 205 (1999) [arXiv:nucl-th/9907090].
- [84] M. Bleicher, W. Greiner, H. Stoecker and N. Xu, *Phys. Rev. C* **62**, 061901 (2000) [arXiv:hep-ph/0007215].
- [85] E. L. Bratkovskaya *et al.*, *Phys. Rev. C* **69**, 054907 (2004) [arXiv:nucl-th/0402026].
- [86] M. Bleicher, M. Belkacem, S. A. Bass, S. Soff and H. Stoecker, *Phys. Lett. B* **485**, 133 (2000) [arXiv:hep-ph/0004045].
- [87] M. Bleicher, J. Randrup, R. Snellings and X. N. Wang, *Phys. Rev. C* **62**, 041901 (2000) [arXiv:nucl-th/0006047].
- [88] M. Bleicher and J. Aichelin, *Phys. Lett. B* **530**, 81 (2002) [arXiv:hep-ph/0201123].
- [89] M. Bleicher, *Nucl. Phys. A* **715**, 85 (2003) [arXiv:hep-ph/0212378].
- [90] M. Bleicher and H. Stoecker, *J. Phys. G* **30**, S111 (2004) [arXiv:hep-ph/0312278].
- [91] H. Petersen, M. Bleicher, S. A. Bass and H. Stocker, arXiv:0805.0567 [hep-ph].
- [92] E. Fermi, *Phys. Rev.* **81**, 683-687 (1951).

- [93] E. Fermi, *Prog. Theor. Phys.* **5**, 570-583 (1950).
- [94] S. Z. Belenkij, L. D. Landau, *Nuovo Cim. Suppl.* **3S10**, 15 (1956).
- [95] L. D. Landau, *Izv. Akad. Nauk Ser. Fiz.* **17**, 51-64 (1953).
- [96] J. Hofmann, H. Stoecker, U. W. Heinz, W. Scheid and W. Greiner, *Phys. Rev. Lett.* **36**, 88 (1976).
- [97] H. Stoecker, J. A. Maruhn and W. Greiner, *Phys. Rev. Lett.* **44**, 725 (1980).
- [98] H. Stoecker *et al.*, *Phys. Rev. C* **25**, 1873 (1982).
- [99] L. P. Csernai and D. Rohrlich, *Phys. Lett. B* **458**, 454 (1999) [arXiv:nucl-th/9908034].
- [100] L. P. Csernai *et al.*, arXiv:hep-ph/0401005.
- [101] W. Schmidt, U. Katscher, B. Waldhauser, J. A. Maruhn, H. Stocker and W. Greiner, *Phys. Rev. C* **47**, 2782 (1993).
- [102] P. F. Kolb and U. W. Heinz, arXiv:nucl-th/0305084.
- [103] R. Baier and P. Romatschke, *Eur. Phys. J. C* **51**, 677 (2007) [arXiv:nucl-th/0610108].
- [104] H. Song and U. W. Heinz, *Phys. Lett. B* **658**, 279 (2008) [arXiv:0709.0742 [nucl-th]].
- [105] D. H. Rischke, S. Bernard and J. A. Maruhn, *Nucl. Phys. A* **595**, 346 (1995) [arXiv:nucl-th/9504018].
- [106] P. Romatschke and U. Romatschke, *Phys. Rev. Lett.* **99**, 172301 (2007) [arXiv:0706.1522 [nucl-th]].
- [107] F. Cooper and G. Frye, *Phys. Rev. D* **10**, 186 (1974).
- [108] M. Fukugita and A. Ukawa, *Phys. Rev. Lett.* **57**, 503 (1986).
- [109] F. Karsch and E. Laermann, *Phys. Rev. D* **50**, 6954 (1994) [arXiv:hep-lat/9406008].
- [110] S. Aoki *et al.* [JLQCD Collaboration], *Phys. Rev. D* **57**, 3910 (1998) [arXiv:hep-lat/9710048].
- [111] F. Karsch, E. Laermann and A. Peikert, *Nucl. Phys. B* **605**, 579 (2001) [arXiv:hep-lat/0012023].
- [112] C. R. Allton *et al.*, *Phys. Rev. D* **66**, 074507 (2002) [arXiv:hep-lat/0204010].
- [113] G. Boyd, J. Engels, F. Karsch, E. Laermann, C. Legeland, M. Lutgemeier and B. Petersson, *Nucl. Phys. B* **469**, 419 (1996) [arXiv:hep-lat/9602007].

- [114] F. Karsch, E. Laermann and A. Peikert, Phys. Lett. B **478**, 447 (2000) [arXiv:hep-lat/0002003].
- [115] Y. Aoki, Z. Fodor, S. D. Katz and K. K. Szabo, Phys. Lett. B **643**, 46 (2006) [arXiv:hep-lat/0609068].
- [116] Z. Fodor, S. D. Katz and K. K. Szabo, Phys. Lett. B **568**, 73 (2003) [arXiv:hep-lat/0208078].
- [117] C. R. Allton, S. Ejiri, S. J. Hands, O. Kaczmarek, F. Karsch, E. Laermann and C. Schmidt, Phys. Rev. D **68**, 014507 (2003) [arXiv:hep-lat/0305007].
- [118] C. R. Allton *et al.*, Phys. Rev. D **71**, 054508 (2005) [arXiv:hep-lat/0501030].
- [119] P. de Forcrand, O. Philipsen, Nucl. Phys. **B673**, 170-186 (2003). [hep-lat/0307020].
- [120] E. Laermann and O. Philipsen, Ann. Rev. Nucl. Part. Sci. **53**, 163 (2003) [arXiv:hep-ph/0303042].
- [121] M. D’Elia, M. P. Lombardo, Phys. Rev. **D70**, 074509 (2004). [hep-lat/0406012].
- [122] M. D’Elia, M. -P. Lombardo, Phys. Rev. **D67**, 014505 (2003). [hep-lat/0209146].
- [123] Y. Hidaka, L. D. McLerran and R. D. Pisarski, Nucl. Phys. A **808**, 117 (2008) [arXiv:0803.0279 [hep-ph]].
- [124] P. Huovinen and P. Petreczky, Nucl. Phys. A **837**, 26 (2010) [arXiv:0912.2541 [hep-ph]].
- [125] A. Chodos, R. L. Jaffe, K. Johnson, C. B. Thorn and V. F. Weisskopf, Phys. Rev. D **9**, 3471 (1974).
- [126] L. M. Satarov, M. N. Dmitriev and I. N. Mishustin, Phys. Atom. Nucl. **72**, 1390 (2009) [arXiv:0901.1430 [hep-ph]].
- [127] P. Papazoglou, ”‘Einheitliche Beschreibung von Hadronen und Kernen in einem chiralen  $SU(3)_L$ -Modell”’, *Doktorarbeit*, J.W.Goethe-Universität Frankfurt, Frankfurt am Main 1998.
- [128] D. Zschesche, ”‘Excited Hadronic Matter in a Chiral  $SU(3)_L \times SU(3)_R$ -Modell”’, *Doktorarbeit*, J.W.Goethe-Universität Frankfurt, Frankfurt am Main 2003.
- [129] P. Papazoglou, ”‘Chirale Beschreibung Seltsamer Hadronischer Materie in einem verallgemeinerten  $SU(3)_L \times SU(3)_R$   $\sigma$ -Modell”’, *Diplomarbeit*, J.W.Goethe-Universität Frankfurt, Frankfurt am Main 1997.
- [130] D. Zschesche, ”‘Beschreibung von Heißer, Dichter und Seltsamer Materie in einem chiralen  $SU(3)_L \times SU(3)_R$   $\sigma$ -Modell”’, *Diplomarbeit*, J.-W.Goethe-Universität Frankfurt, Frankfurt am Main 1997.

- [131] P. Papazoglou, D. Zschesche, S. Schramm, J. Schaffner-Bielich, H. Stoecker and W. Greiner, *Phys. Rev. C* **59**, 411 (1999) [arXiv:nucl-th/9806087].
- [132] P. Papazoglou, S. Schramm, J. Schaffner-Bielich, H. Stoecker and W. Greiner, *Phys. Rev. C* **57**, 2576 (1998) [arXiv:nucl-th/9706024].
- [133] V. Dexheimer and S. Schramm, *Astrophys. J.* **683**, 943 (2008) [arXiv:0802.1999 [astro-ph]].
- [134] V. A. Dexheimer and S. Schramm, *Phys. Rev. C* **81**, 045201 (2010) [arXiv:0901.1748 [astro-ph.SR]].
- [135] K. Fukushima, *Phys. Lett. B* **591**, 277 (2004) [arXiv:hep-ph/0310121].
- [136] C. Ratti, M. A. Thaler and W. Weise, *Phys. Rev. D* **73**, 014019 (2006) [arXiv:hep-ph/0506234].
- [137] C. Ratti and W. Weise, *Phys. Rev. D* **70**, 054013 (2004) [arXiv:hep-ph/0406159].
- [138] S. Roessner, C. Ratti and W. Weise, *Phys. Rev. D* **75**, 034007 (2007) [arXiv:hep-ph/0609281].
- [139] C. Sasaki, B. Friman and K. Redlich, *Phys. Rev. D* **75**, 074013 (2007) [arXiv:hep-ph/0611147].
- [140] C. Ratti, S. Roessner and W. Weise, *Phys. Lett. B* **649**, 57 (2007) [arXiv:hep-ph/0701091].
- [141] S. Roessner, T. Hell, C. Ratti and W. Weise, *Nucl. Phys. A* **814**, 118 (2008) [arXiv:0712.3152 [hep-ph]].
- [142] M. Ciminale, R. Gatto, N. D. Ippolito, G. Nardulli and M. Ruggieri, *Phys. Rev. D* **77**, 054023 (2008) [arXiv:0711.3397 [hep-ph]].
- [143] B. J. Schaefer, J. M. Pawłowski and J. Wambach, *Phys. Rev. D* **76**, 074023 (2007) [arXiv:0704.3234 [hep-ph]].
- [144] W. j. Fu, Z. Zhang and Y. x. Liu, *Phys. Rev. D* **77**, 014006 (2008) [arXiv:0711.0154 [hep-ph]].
- [145] T. Hell, S. Roessner, M. Cristoforetti and W. Weise, *Phys. Rev. D* **79**, 014022 (2009) [arXiv:0810.1099 [hep-ph]].
- [146] H. Abuki, R. Anglani, R. Gatto, G. Nardulli and M. Ruggieri, *Phys. Rev. D* **78**, 034034 (2008) [arXiv:0805.1509 [hep-ph]].
- [147] K. Fukushima, *Phys. Rev. D* **77**, 114028 (2008) [Erratum-ibid. *D* **78**, 039902 (2008)] [arXiv:0803.3318 [hep-ph]].



- [148] K. Fukushima, Phys. Rev. D **78**, 114019 (2008) [arXiv:0809.3080 [hep-ph]].
- [149] P. Costa, C. A. de Sousa, M. C. Ruivo and H. Hansen, Europhys. Lett. **86**, 31001 (2009) [arXiv:0801.3616 [hep-ph]].
- [150] P. Costa, M. C. Ruivo, C. A. de Sousa, H. Hansen and W. M. Alberico, Phys. Rev. D **79**, 116003 (2009) [arXiv:0807.2134 [hep-ph]].
- [151] H. Hansen, W. M. Alberico, A. Beraudo, A. Molinari, M. Nardi and C. Ratti, Phys. Rev. D **75**, 065004 (2007) [arXiv:hep-ph/0609116].
- [152] S. Mukherjee, M. G. Mustafa and R. Ray, Phys. Rev. D **75**, 094015 (2007) [arXiv:hep-ph/0609249].
- [153] H. Abuki, M. Ciminale, R. Gatto, N. D. Ippolito, G. Nardulli and M. Ruggieri, Phys. Rev. D **78**, 014002 (2008) [arXiv:0801.4254 [hep-ph]].
- [154] H. Abuki, M. Ciminale, R. Gatto, G. Nardulli and M. Ruggieri, Phys. Rev. D **77**, 074018 (2008) [arXiv:0802.2396 [hep-ph]].
- [155] K. Fukushima, Phys. Rev. D **79**, 074015 (2009) [arXiv:0901.0783 [hep-ph]].
- [156] H. Mao, J. Jin and M. Huang, J. Phys. G **37**, 035001 (2010) [arXiv:0906.1324 [hep-ph]].
- [157] B. J. Schaefer, M. Wagner and J. Wambach, Phys. Rev. D **81**, 074013 (2010) [arXiv:0910.5628 [hep-ph]].
- [158] S. K. Ghosh, T. K. Mukherjee, M. G. Mustafa and R. Ray, Phys. Rev. D **73**, 114007 (2006) [arXiv:hep-ph/0603050].
- [159] C. Ratti, S. Roessner, M. A. Thaler and W. Weise, Eur. Phys. J. C **49**, 213 (2007) [arXiv:hep-ph/0609218].
- [160] K. Fukushima and Y. Hidaka, Phys. Rev. D **75**, 036002 (2007) [arXiv:hep-ph/0610323].
- [161] A. Dumitru, R. D. Pisarski and D. Zschiesche, Phys. Rev. D **72**, 065008 (2005) [arXiv:hep-ph/0505256].
- [162] R. Hagedorn and J. Rafelski, Phys. Lett. B **97**, 136 (1980).
- [163] J. Baacke, Acta Phys. Polon. B **8**, 625 (1977).
- [164] M. I. Gorenstein, V. K. Petrov and G. M. Zinovev, Phys. Lett. B **106**, 327 (1981).
- [165] R. Hagedorn, Z. Phys. C **17**, 265 (1983).

- [166] D. H. Rischke, M. I. Gorenstein, H. Stoecker and W. Greiner, *Z. Phys. C* **51**, 485 (1991).
- [167] J. Cleymans, M. I. Gorenstein, J. Stalnacke and E. Suhonen, *Phys. Scripta* **48**, 277 (1993).
- [168] K. A. Bugaev, M. I. Gorenstein, H. Stoecker and W. Greiner, *Phys. Lett. B* **485**, 121 (2000) [arXiv:nucl-th/0004061].
- [169] K. A. Bugaev, *Nucl. Phys. A* **807**, 251 (2008).
- [170] J. I. Kapusta and K. A. Olive, *Nucl. Phys. A* **408**, 478 (1983).
- [171] Z. Fodor and S. D. Katz, *JHEP* **0404**, 050 (2004) [arXiv:hep-lat/0402006].
- [172] Y. Aoki, S. Borsanyi, S. Durr, Z. Fodor, S. D. Katz, S. Krieg and K. K. Szabo, *JHEP* **0906**, 088 (2009) [arXiv:0903.4155 [hep-lat]].
- [173] C. E. Detar and R. Gupta [HotQCD Collaboration], *PoS LAT2007*, 179 (2007) [arXiv:0710.1655 [hep-lat]].
- [174] A. Bazavov *et al.*, *Phys. Rev. D* **80**, 014504 (2009) [arXiv:0903.4379 [hep-lat]].
- [175] A. Bazavov and P. Petreczky [HotQCD collaboration], *J. Phys. Conf. Ser.* **230**, 012014 (2010) [arXiv:1005.1131 [hep-lat]].
- [176] J. R. Ellis, J. I. Kapusta and K. A. Olive, *Phys. Lett. B* **273**, 123 (1991).
- [177] H. Stoecker, G. Graebner, J. A. Maruhn and W. Greiner, *Phys. Lett. B* **95**, 192 (1980).
- [178] J. P. Blaizot, *Phys. Rept.* **64**, 171 (1980).
- [179] M. Cheng *et al.*, *Phys. Rev. D* **79**, 074505 (2009) [arXiv:0811.1006 [hep-lat]].
- [180] J. Steinheimer, M. Mitrovski, T. Schuster, H. Petersen, M. Bleicher and H. Stoecker, *Phys. Lett. B* **676**, 126 (2009) [arXiv:0811.4077 [hep-ph]].
- [181] C. Greiner, P. Koch and H. Stoecker, *Phys. Rev. Lett.* **58**, 1825 (1987).
- [182] C. Greiner, D. H. Rischke, H. Stoecker and P. Koch, *Phys. Rev. D* **38**, 2797 (1988).
- [183] S. V. Afanasiev *et al.* [The NA49 Collaboration], *Phys. Rev. C* **66**, 054902 (2002) [arXiv:nucl-ex/0205002].
- [184] P. Koch, B. Muller and J. Rafelski, *Phys. Rept.* **142**, 167 (1986).
- [185] S. Soff *et al.*, *Phys. Lett. B* **471**, 89 (1999) [arXiv:nucl-th/9907026].

- [186] C. Greiner, P. Koch-Steinheimer, F. M. Liu, I. A. Shovkovy and H. Stoecker, *J. Phys. G* **31**, S725 (2005) [arXiv:hep-ph/0412095].
- [187] P. Braun-Munzinger, J. Stachel and C. Wetterich, *Phys. Lett. B* **596**, 61 (2004) [arXiv:nucl-th/0311005].
- [188] J. Noronha-Hostler, H. Ahmad, J. Noronha and C. Greiner, *Phys. Rev. C* **82**, 024913 (2010) [arXiv:0906.3960 [nucl-th]].
- [189] F. Becattini and U. W. Heinz, *Z. Phys. C* **76**, 269 (1997) [Erratum-ibid. *C* **76**, 578 (1997)] [arXiv:hep-ph/9702274].
- [190] J. Cleymans, K. Redlich and E. Suhonen, *Z. Phys. C* **51**, 137 (1991).
- [191] P. Braun-Munzinger, D. Magestro, K. Redlich *et al.*, *Phys. Lett.* **B518**, 41-46 (2001). [hep-ph/0105229].
- [192] F. Becattini, *Z. Phys.* **C69**, 485-492 (1996).
- [193] A. Andronic, P. Braun-Munzinger and J. Stachel, *Nucl. Phys. A* **772**, 167 (2006) [arXiv:nucl-th/0511071].
- [194] C. Alt *et al.* [NA49 Collaboration], *Phys. Rev. C* **78**, 034918 (2008) [arXiv:0804.3770 [nucl-ex]].
- [195] L. Ahle *et al.* [E866 Collaboration and E917 Collaboration], *Phys. Lett. B* **476**, 1 (2000) [arXiv:nucl-ex/9910008].
- [196] J. Adams *et al.* [STAR Collaboration], *Phys. Rev. Lett.* **92**, 112301 (2004) [arXiv:nucl-ex/0310004].
- [197] K. Adcox *et al.* [PHENIX Collaboration], *Phys. Rev. C* **69**, 024904 (2004) [arXiv:nucl-ex/0307010].
- [198] J. L. Klay *et al.* [E-0895 Collaboration], *Phys. Rev. C* **68**, 054905 (2003) [arXiv:nucl-ex/0306033].
- [199] M. K. Mitrovski *et al.* [NA49 Collaboration], *J. Phys. G* **32**, S43 (2006) [arXiv:nucl-ex/0606004].
- [200] H. Weber, E. L. Bratkovskaya, W. Cassing and H. Stoecker, *Phys. Rev. C* **67**, 014904 (2003) [arXiv:nucl-th/0209079].
- [201] T. Anticic *et al.* [NA49 Collaboration], *Phys. Rev. C* **69**, 024902 (2004).
- [202] I. Adachi *et al.* [Belle Collaboration], arXiv:0810.1657 [hep-ex].
- [203] T. S. Biro, H. B. Nielsen and J. Knoll, *Nucl. Phys. B* **245**, 449 (1984).

- [204] J. Knoll, *Z. Phys. C* **38**, 187 (1988).
- [205] H. Sorge, *Phys. Rev. C* **52**, 3291 (1995) [arXiv:nucl-th/9509007].
- [206] H. Sorge, *Phys. Lett. B* **344**, 35 (1995).
- [207] C. Pinkenburg *et al.* [E895 Collaboration], *Nucl. Phys. A* **698**, 495 (2002) [arXiv:nucl-ex/0104025].
- [208] P. Chung *et al.* [E895 collaboration], *Phys. Rev. Lett.* **91**, 202301 (2003) [arXiv:nucl-ex/0302021].
- [209] T. Anticic *et al.* [NA49 Collaboration], *Phys. Rev. Lett.* **93**, 022302 (2004) [arXiv:nucl-ex/0311024].
- [210] A. Richard [NA49 Collaboration], *J. Phys. G* **31**, S155 (2005).
- [211] C. Alt *et al.* [NA49 Collaboration], *Phys. Rev. C* **78**, 034918 (2008) [arXiv:0804.3770 [nucl-ex]].
- [212] C. Blume [NA49 Collaboration], *J. Phys. G* **31**, S685 (2005) [arXiv:nucl-ex/0411039].
- [213] S. V. Afanasiev *et al.* [NA49 Collaboration], *Phys. Lett. B* **538**, 275 (2002) [arXiv:hep-ex/0202037].
- [214] Y. Akiba *et al.* [E802 Collaboration], *Nucl. Phys. A* **610**, 139C (1996).
- [215] C. Alt *et al.* [NA49 Collaboration], *Phys. Rev. C* **73**, 044910 (2006).
- [216] H. Petersen, J. Steinheimer, M. Bleicher and H. Stoecker, *J. Phys. G* **36**, 055104 (2009) [arXiv:0902.4866 [nucl-th]].
- [217] L. Van Hove, *Phys. Lett. B* **118**, 138 (1982).
- [218] F. Grassi, Y. Hama and T. Kodama, *Phys. Lett. B* **355**, 9 (1995).
- [219] J. Knoll, *Nucl. Phys. A* **821**, 235 (2009) [arXiv:0803.2343 [nucl-th]].
- [220] J. Brachmann *et al.*, *Phys. Rev. C* **61**, 024909 (2000) [arXiv:nucl-th/9908010].
- [221] H. Stoecker, *Nucl. Phys. A* **750**, 121 (2005) [arXiv:nucl-th/0406018].
- [222] H. Petersen, Q. Li, X. Zhu and M. Bleicher, *Phys. Rev. C* **74**, 064908 (2006) [arXiv:hep-ph/0608189].
- [223] M. Isse, A. Ohnishi, N. Otuka, P. K. Sahu and Y. Nara, *Phys. Rev. C* **72**, 064908 (2005) [arXiv:nucl-th/0502058].

- [224] Q. f. Li, Z. x. Li, S. Soff, M. Bleicher and H. Stoecker, *J. Phys. G* **32**, 407 (2006) [arXiv:nucl-th/0601047].
- [225] Q. f. Li, J. Steinheimer, H. Petersen, M. Bleicher and H. Stoecker, *Phys. Lett. B* **674**, 111 (2009) [arXiv:0812.0375 [nucl-th]].
- [226] V. Koch, A. Majumder and J. Randrup, *Phys. Rev. Lett.* **95**, 182301 (2005) [arXiv:nucl-th/0505052].
- [227] K. Paech, H. Stoecker and A. Dumitru, *Phys. Rev. C* **68**, 044907 (2003) [arXiv:nucl-th/0302013].
- [228] T. Schuster, M. Nahrgang, M. Mitrovski, R. Stock and M. Bleicher, arXiv:0903.2911 [hep-ph].
- [229] A. R. Bodmer, *Phys. Rev. D* **4**, 1601 (1971).
- [230] R. L. Jaffe, *Phys. Rev. Lett.* **38**, 195 (1977) [Erratum-ibid. **38**, 617 (1977)].
- [231] J. T. Goldman, K. Maltman, G. J. . Stephenson, K. E. Schmidt and F. Wang, *Phys. Rev. Lett.* **59**, 627 (1987).
- [232] J. T. Goldman, K. Maltman, G. J. . Stephenson, J. L. . Ping and F. Wang, *Mod. Phys. Lett. A* **13**, 59 (1998) [arXiv:nucl-th/9803002].
- [233] B. Schwesinger, F. G. Scholtz and H. B. Geyer, *Phys. Rev. D* **51**, 1228 (1995) [arXiv:nucl-th/9408002].
- [234] R. J. Oakes and C. N. Yang, *Phys. Rev. Lett.* **11**, 174 (1963).
- [235] L. M. Libby, *Phys. Lett. B* **29**, 345 (1969).
- [236] S. Graffi, V. Grecchi and G. Turchetti, *Lett. Nuovo Cim.* **2S1**, 311 (1969) [*Lett. Nuovo Cim.* **2**, 311 (1969)].
- [237] A. T. M. Aerts, P. J. G. Mulders and J. J. de Swart, *Phys. Rev. D* **17**, 260 (1978).
- [238] C. W. Wong and K. F. Liu, *Phys. Rev. Lett.* **41**, 82 (1978).
- [239] A. T. M. Aerts and C. B. Dover, *Phys. Lett. B* **146**, 95 (1984).
- [240] Yu. S. Kalashnikova, I. M. Narodetsky and Yu. A. Simonov, *Sov. J. Nucl. Phys.* **46**, 689 (1987) [*Yad. Fiz.* **46**, 1181 (1987)].
- [241] J. T. Goldman, K. Maltman, G. J. . Stephenson, K. E. Schmidt and F. Wang, *Phys. Rev. C* **39**, 1889 (1989).
- [242] J. Schaffner-Bielich, R. Mattiello and H. Sorge, *Phys. Rev. Lett.* **84**, 4305 (2000) [arXiv:nucl-th/9908043].

- [243] J. Schaffner-Bielich, Nucl. Phys. A **691**, 416 (2001) [arXiv:nucl-th/0011078].
- [244] J. K. Ahn *et al.*, Phys. Rev. Lett. **87**, 132504 (2001).
- [245] H. Takahashi *et al.*, Phys. Rev. Lett. **87**, 212502 (2001).
- [246] R. H. Dalitz, D. H. Davis, P. H. Fowler, A. Montwill, J. Pniewski and J. A. Zakrzewski, Proc. Roy. Soc. Lond. A **426**, 1 (1989)
- [247] J. Schaffner, H. Stoecker and C. Greiner, Phys. Rev. C **46**, 322 (1992).
- [248] J. Schaffner, C. B. Dover, A. Gal, C. Greiner and H. Stoecker, Phys. Rev. Lett. **71**, 1328 (1993).
- [249] E. P. Gilson and R. L. Jaffe, Phys. Rev. Lett. **71**, 332 (1993) [arXiv:hep-ph/9302270].
- [250] J. Schaffner-Bielich, C. Greiner, A. Diener and H. Stoecker, Phys. Rev. C **55**, 3038 (1997) [arXiv:nucl-th/9611052].
- [251] V. G. J. Stoks and T. A. Rijken, Phys. Rev. C **59**, 3009 (1999) [arXiv:nucl-th/9901028].
- [252] S. Scherer, M. Bleicher, S. Haussler and H. Stoecker, Int. J. Mod. Phys. E **17**, 965 (2008).
- [253] J. Aichelin and K. Werner, Phys. Rev. C **79**, 064907 (2009) [Erratum-ibid. C **81**, 029902 (2010)] [arXiv:0810.4465 [nucl-th]].
- [254] J. F. Donoghue, E. Golowich and B. R. Holstein, Phys. Rev. D **34**, 3434 (1986).
- [255] M. I. Krivoruchenko and M. G. Shchepkin, Sov. J. Nucl. Phys. **36**, 769 (1982) [Yad. Fiz. **36**, 1328 (1982)].
- [256] J. Belz *et al.* [BNL-E888 Collaboration], Phys. Rev. Lett. **76**, 3277 (1996) [Phys. Rev. C **56**, 1164 (1997)] [arXiv:hep-ex/9603002].
- [257] H. J. Crawford, Nucl. Phys. A **639**, 417 (1998).
- [258] H. Caines *et al.* [E896 Collaboration], Nucl. Phys. A **661**, 170 (1999).
- [259] G. Appelquist *et al.* [NA52 (NEWMASS) Collaboration], Phys. Rev. Lett. **76**, 3907 (1996).
- [260] T. A. Armstrong *et al.* [E864 Collaboration], Phys. Rev. Lett. **79**, 3612 (1997) [arXiv:nucl-ex/9706004].
- [261] A. Alavi-Harati *et al.* [KTeV Collaboration], Phys. Rev. Lett. **84**, 2593 (2000) [arXiv:hep-ex/9910030].

- [262] L. E. Finch [E864 Collaboration], Nucl. Phys. A **661**, 395 (1999) [arXiv:nucl-ex/9908019].
- [263] D. Zschesche, S. Schramm, J. Schaffner-Bielich, H. Stoecker and W. Greiner, Phys. Lett. B **547**, 7 (2002) [arXiv:nucl-th/0209022].
- [264] H. Petersen, J. Steinheimer, G. Burau, M. Bleicher and H. Stoecker, Phys. Rev. C **78**, 044901 (2008) [arXiv:0806.1695 [nucl-th]].
- [265] P. Braun-Munzinger and J. Stachel, J. Phys. G **21**, L17 (1995) [arXiv:nucl-th/9412035].
- [266] J. Steinheimer, S. Schramm and H. Stoecker, arXiv:0909.4421 [hep-ph].
- [267] A. Andronic, P. Braun-Munzinger and J. Stachel, Phys. Lett. B **673**, 142 (2009) [Erratum-ibid. B **678**, 516 (2009)] [arXiv:0812.1186 [nucl-th]].
- [268] T. A. Armstrong *et al.* [E864 Collaboration], Phys. Rev. C **70**, 024902 (2004) [arXiv:nucl-ex/0211010].
- [269] J. H. Chen and f. t. S. Collaboration, Nucl. Phys. A **830**, 761C (2009) [arXiv:0907.4147 [nucl-ex]].
- [270] C. Greiner and H. Stoecker, Phys. Rev. D **44**, 3517 (1991).
- [271] F. Becattini, J. Cleymans, A. Keranen, E. Suhonen and K. Redlich, Phys. Rev. C **64**, 024901 (2001) [arXiv:hep-ph/0002267].
- [272] J. Cleymans and K. Redlich, Phys. Rev. C **60**, 054908 (1999) [arXiv:nucl-th/9903063].
- [273] F. Becattini and J. Manninen, Phys. Lett. B **673**, 19 (2009) [arXiv:0811.3766 [nucl-th]].
- [274] L. Ferroni and V. Koch, arXiv:1003.4428 [nucl-th].
- [275] P. de Forcrand, S. Kim and O. Philipsen, PoS **LAT2007**, 178 (2007) [arXiv:0711.0262 [hep-lat]].
- [276] I. Ahmad, M. Mian, M. Z. Rahman Khan, Phys. Rev. **C31**, 1590-1592 (1985).
- [277] B. Baeuchle and M. Bleicher, Phys. Rev. C **81**, 044904 (2010) [arXiv:0905.4678 [hep-ph]].
- [278] B. Baeuchle and M. Bleicher, arXiv:1008.2338 [nucl-th].
- [279] B. Baeuchle and M. Bleicher, arXiv:1008.2332 [nucl-th].
- [280] E. Santini and M. Bleicher, arXiv:1009.5266 [nucl-th].

- [281] J. S. Schwinger, *Annals Phys.* **2**, 407 (1957).
- [282] M. Gell-Mann and M. Levy, *Nuovo Cim.* **16**, 705 (1960).
- [283] S. Weinberg, *Phys. Rev. Lett.* **18**, 188-191 (1967).
- [284] S. Weinberg, *Phys. Rev.* **166**, 1568-1577 (1968).
- [285] S. Coleman: "‘Aspects of Symmetry’", Cambridge University Press, Cambridge 1985.
- [286] C. G. Callan Jr., S. R. Coleman und R. Jackiw, *Annals Phys.* **59** (1970) 42.
- [287] C. G. Callan Jr., *Phys. Rev. D* **2** (1970) 1541.
- [288] J. C. Collins, A. Duncan und S. D. Joglekar, *Phys. Rev. D* **16** (1977) 438.
- [289] J. Schechter und Y. Ueda, *Phys. Rev. D* **3** (1971) 2874.
- [290] J. Schechter, *Phys. Rev. D* **21** (1980) 3393.
- [291] E. K. Heide, S. Rudaz und P. J. Ellis, *Phys. Lett. B* **293** (1992) 259.
- [292] E. K. Heide, S. Rudaz und P. J. Ellis, *Nucl. Phys. A* **571** (1994) 713 [arXiv:nucl-th/9308002].
- [293] W. Israel and J. M. Stewart, *Annals Phys.* **118**, 341 (1979).
- [294] W. A. Hiscock and L. Lindblom, *Phys. Rev. D* **31**, 725 (1985).
- [295] A. Muronga, *Phys. Rev. C* **69**, 034903 (2004) [arXiv:nucl-th/0309055].
- [296] A. Muronga, *Phys. Rev. Lett.* **88**, 062302 (2002) [Erratum-ibid. **89**, 159901 (2002)] [arXiv:nucl-th/0104064].
- [297] A. Muronga and D. H. Rischke, arXiv:nucl-th/0407114.
- [298] A. Muronga, *Phys. Rev. C* **76**, 014909 (2007) [arXiv:nucl-th/0611090].
- [299] H. Song and U. W. Heinz, *Phys. Rev. C* **77**, 064901 (2008) [arXiv:0712.3715 [nucl-th]].
- [300] U. W. Heinz, H. Song and A. K. Chaudhuri, *Phys. Rev. C* **73**, 034904 (2006) [arXiv:nucl-th/0510014].
- [301] M. Luzum and P. Romatschke, *Phys. Rev. C* **78**, 034915 (2008) [Erratum-ibid. **C 79**, 039903 (2009)] [arXiv:0804.4015 [nucl-th]].
- [302] R. Baier, P. Romatschke, D. T. Son, A. O. Starinets and M. A. Stephanov, *JHEP* **0804**, 100 (2008) [arXiv:0712.2451 [hep-th]].



- [303] K. Dusling and D. Teaney, Phys. Rev. C **77**, 034905 (2008) [arXiv:0710.5932 [nucl-th]].
- [304] P. Huovinen and D. Molnar, Phys. Rev. C **79**, 014906 (2009) [arXiv:0808.0953 [nucl-th]].

## C.1 Danksagung

Zuerst möchte ich bei Prof. Dr. Dr. h.c. Stöcker für die Möglichkeit bedanken meine Arbeit in diesem für mich so spannenden Gebiet schreiben zu können. Obwohl er vielbeschäftigt war hat er es doch immer geschafft meine Forschung durch seine kreativen und verrückten Kommentare zu inspirieren. Besonderer Dank gebührt auch den Professoren S. Schramm und M. Bleicher die mich in Prof. Stöckers Abwesenheit bereitwillig und tatkräftig unterstützten, mir bei vielen Fragestellungen hilfreich zur Seite standen und hatten immer ein offenes Ohr.

Auch den anderen Professoren am Institut möchte ich meine Dankbarkeit für viele interessante Diskussionen und Anregungen ausdrücken. Besonders hier die Professoren Greiner, Rischke und Schaffner-Bieleich hervorgehoben.

Ich danke der ganzen UrQMD Gruppe und besonders Gunnar Gräf und Thomas Lang mit denen ich lange mein Büro teilen und in Diskussionen verwickeln durfte. Ich danke Dr. Hannah Petersen mit deren Zusammenarbeit Teile dieser Arbeit entstanden sind. Danke an Dr. Elvira Santini, Dr. Qiungfeng Li, Dr. Michael Mitrovski, Björn Bäuchle, Marlene Nahrgang und Christoph Herold für die Zusammenarbeit.

Danke an Phillip Rau für die vielen Mittagspausen im Café Physik und an Manuel Lorenz für die interessanten Mittagsgespräche über die Physik und Literaturanregungen.

Ich danke der HGS-HiRe Graduiertenschule, sowie Henner Büsching dem Mann hinter dieser, für die Unterstützung während meiner Doktorandenzeit, die Seminare und Weiterbildungen.

Die meisten Berechnungen dieser Arbeit wurden auf dem CSC Computercluster der Uni Frankfurt durchgeführt. Danke an die Administration und das Team des CSC.

Ganz besonderer Dank geht an meine Eltern die mich auf meinem Weg immer unterstützten und insbesondere an meinen Vater der nie müde wurde meine physikalische Arbeit durch seine Kommentare zu bereichern.

Ohne die liebevolle Unterstützung durch meine Familie diese Arbeit auf die Beine zu stellen. Vielen dank an meine Frau Sonja meinen Sohn Anton und meine Tochter Ida dafür, dass sie soviel Verständnis für meine Arbeit, die Spinnereien und Konferenzen hatten. Ohne diese Verständnis und den Zuspruch hätte ich niemals meine Arbeit, in einem Gebiet das mir soviel Freude bereitet, fertigstellen können.

## C.2 Lebenslauf

Name: Jan Mattes Steinheimer-Froschauer

Geburtsdatum: 02.08.1982

Geburtsort: Frankfurt am Main

Familienstand: Verheiratet / 2 Kinder

Schulische Ausbildung:

1987-1988 Rocky-Point Elementary School in Rocky Point NY USA

1988-1992 Dietrich Bonhoeffer Grundschule in Dietzenbach

1992-1998 Ernst Reuter Schule in Dietzenbach, gymnasiale Mittelstufe

1998-1999 Southampton High-School in Southampton NY USA

1999-2002 Claus von Stauffenberg Schule in Rodgau-Dudenhofen, Gymnasiale Oberstufe, Abitur (2,4)

Zivildienst:

2002-2003 Individuelle Schwerstbehindertenbetreuung bei der Behindertenhilfe e.V. in Offenbach am Main

Studium:

- 10/03-03/08 Studium der Physik an der Johann-Wolfgang-Goethe Universität in Frankfurt am Main mit Schwerpunkt Theoretische Physik. Abschluss: Diplom (Sehr gut)
- seit 04/08 Promotionsstudium an der Goethe Universität Frankfurt am Main
- seit 09/09 Mitglied der Graduiertenschule HGS-HIRe (Helmholtz Graduate School for Hadron and Ion Research)
- 10/10 Verleihung des 'Exelence Awards' für herausragende Leistungen während der Promotion durch die HGS-HIRe Graduiertenschule.

### **C.3 Akademische Lehrer**

Prof. Dr. Dr. h.c. Stöcker  
Prof. Dr. Roskos  
Prof. Dr. Bleicher  
Prof. Dr. Schramm  
Prof. Dr. C. Greiner  
Prof. Dr. Rischke  
Prof. Dr. Schaffner-Bielich  
Prof. Dr. Dörner  
Prof. Dr. Jacoby  
Prof. Dr. Bruls  
Prof. Dr. Schempp  
Prof. Dr. Siemsen  
Prof. Dr. Baumeister  
Prof. Dr. Schmeling  
Prof. Dr. Stroth  
Prof. Dr. Appelshäuser  
Prof. Dr. Ströbele  
Prof. Dr. Meyer  
Prof. Dr. Lang  
Prof. Dr. Peters